Alma Mater Studiorum – Università di Bologna
in cotutela con Università di Costanza

DOTTORATO DI RICERCA IN

FISICA

Ciclo XXXI

Settore Concorsuale: FIS/03

Settore Scientifico Disciplinare: 02/B1

Development and analyses of innovative thin films for photovoltaic applications

Presentata da: Maria Antonietta Fazio

Coordinatore Dottorato

Prof.ssa Silvia Arcelli

Supervisore

Prof.ssa Daniela Cavalcoli

Supervisore

Prof. Giso Hahn

Esame finale anno 2019

Development and analyses of innovative thin films for photovoltaic applications

Maria Antonietta Fazio*

University of Bologna

March 2019

* Bologna, Italy. E-mail: maria.fazio2@unibo.it

Abstract (English)

In solar cell current research, innovative solutions and materials are continuously requested for efficiency improvements. Examples of these strategies could be focused on the decrease of the electron-hole recombination at surfaces and interfaces, through the improvement of passivation quality of the layers and the introduction of different materials in the solar cell structure. Si-based technology rules more than 95% of the whole photovoltaic market, due to silicon abundancy, non-toxicity, low costs and well-known properties. One of the latest Si-based technologies is called silicon heterojunction (SHJ) solar cell and it has reached a new record efficiency of 26.7% in 2017. Nonetheless, hydrogenated amorphous silicon (a-Si:H) layers employed in the so-called "heteroemitter stack" still have some challenges, such as high parasitic light absorption and high contact resistance with the layer on top. These problems could be overcome with the inclusion of oxygen and nitrogen elements within the layers to broaden the energy gap. In parallel, new technologies based on completely different materials are investigated; nonetheless, they still lack in the market due to stability issues (for example, in the case of perovskites) or low efficiencies (in the case of III-group nitride ternary alloys). However, in these preliminary phase a thorough study of the structure, composition, optical and electrical properties, as well as surface and interface quality creates a deeper knowledge on these new materials that could then be exploited in photovoltaic application. Indeed, the solar cell performance is strictly correlated to all these properties. In this overall perspective, we investigated both innovative Si-based materials (nanocrystalline and amorphous sub-stoichiometric silicon oxy-nitride and oxide thin films, nc-SiO_xN_y, a-SiO_xN_y and a-SiO_x, respectively) and innovative materials for solar cell concepts (as perovskite lanthanum-vanadium oxide $LaVO_3$ thin films, and indium gallium nitride $In_xGa_{1-x}N$ and aluminium indium gallium nitride $Al_xIn_yGa_{1-x-y}N$ layers). Different deposition conditions have been employed to extract their influence on compositional, optical, and electrical properties.

The study performed on nc-SiO_xN_y layers by means of conductive atomic force microscopy (c-AFM) and surface photovoltage (SPV) techniques has allowed us to clarify the role of O, N, and B content, and annealing treatment on the microscopic transport properties, and electronic transitions of Si-based thin films for SHJ applications.

From the study on a-SiO_x and a-SiO_xN_y layers by spectral ellipsometry, Fourier transform infrared spectroscopy, photoconductance decay and SPV

measurements, we can conclude that moderate insertions of O and N in a-Si:H lead to a decrease of optical parasitic absorption related to a higher band gap, while maintaining the passivation quality of the layers.
As these Si-based materials generally show also quite good electrical properties, they might be successfully applied in SHJ solar cell devices.
The measurements by AFM and Kelvin probe force microscopy (KPFM) on $LaVO_3$ have clearly shown that this material is a poor charge-transport medium, thus not suitable for photovoltaic applications. A solution could be the incorporation of an additional electron-transport material and hole-transport material into a structure similar to the design of dye-sensitized solar cells, with a huge number of internal interfaces between the individual solar absorber and nanostructured charge transport media to enable the separation and collection of photogenerated electron-hole pairs.
The analysis on InGaN and AlGaInN by SPV measurements has shown how different parameters, such as element composition, Si doping, strain relaxation, dislocations or pinholes can affect the interface quality of the layer with the substrate. Generally, low In content, Si doping and no misfit dislocations in InGaN/GaN structure cause less recombination processes at the interface. Whereas, the strain relaxation (both tensile and compressive) with the formation of pinholes produces better interfaces in the AlGaInN/GaN samples.

Zusammenfassung (Deutsch)

In der aktuellen Forschung der Solarzellen werden kontinuierlich innovative Lösungen und Materialien für weitere Effizienzverbesserungen gefordert. Beispiele für diese Strategien könnten die Verbesserung der Passivierungsqualität der Schichten und die Einführung verschiedener Materialien in der Solarzellenstruktur sein. Si-basierte Technologie beherrscht mehr als 95% des gesamten Photovoltaik-Marktes, aufgrund von Silizium-Abundanz, Ungültigkeit, niedrigen Kosten und bekannten Eigenschaften. Eine der neuesten Si-basierten Technologien heißt Silizium-HeteroJunction (SHJ) Solarzelle und hat 2017 einen neuen Rekord-Wirkungsgrad von 26.7% erreicht. Gleichwohl werden hydrierte amorphe Silizium- (a-Si:H) Schichten in der so verwendet "Heteroemitter Stack" genannt, haben noch einige Probleme, wie hohe parasitäre Lichtabsorption und hohen Kontaktwiderstand mit der darüber liegenden Schicht. Diese Probleme könnten durch den Einschluss von Sauerstoff- und Stickstoffelementen in den Schichten überwunden werden, um die Energielücke zu verbreitern. Parallel dazu werden neue Technologien auf Basis völlig unterschiedlicher Materialien untersucht; Trotzdem mangelt es ihnen aufgrund von Stabilitätsproblemen (z. B. bei Perowskiten) oder niedrigen Wirkungsgraden (bei III-Gruppen-Nitrid-ternären Legierungen) immer noch am Markt. In dieser ersten Phase wird jedoch eine gründliche Untersuchung der Struktur, der optischen und elektrischen Eigenschaften sowie der Oberflächen- und Grenzflächenqualität durchgeführt, um ein tieferes Wissen über diese neuen Materialien zu erhalten, die dann in der Photovoltaik Anwendung finden können. In der Tat korreliert die Leistung der Solarzellen genau mit all diesen Eigenschaften. In dieser Gesamtperspektive untersuchten wir sowohl innovative Si-basierte Materialien (nanokristalline und amorphe substöchiometrische Siliziumoxi-Nitrid- und Oxid-Dünnschichten, nc-SiO_xN_y, a-SiO_xN_y und a-SiO_x) als auch neuere Materialien für Solarzellenkonzepte (als Perovskit-Lanthan-Vanadium-Oxid, $LaVO_3$, dünne Filme und Indiumgalliumnitrid $In_xGa_{1-x}N$ und Aluminium-Indium-Gallium-Ni-Tride, $Al_xIn_yGa_{1-x-y}N$-Schichten). Unterschiedliche Abscheidungsbedingungen wurden verwendet, um ihren Einfluss auf die Zusammensetzung, die optischen Eigenschaften und die elektrischen Eigenschaften zu extrahieren.

Die Studie mit nc-SiO_xN_y-Schichten mittels leitfähiger Rasterkraftmikroskopie (c-AFM) und Surface Photovoltage (SPV) ermöglichte es, die Rolle des O-, N- und B-Gehaltes und die Glühbehandlung auf dem mikroskopischen

Transport zu klären Eigenschaften und elektronische Übergänge von Si-basierten Dünnschichten für SHJ-Anwendungen.
Aus der Untersuchung von a-SiO_x- und a-SiO_xN_y-Schichten durch spektrale Ellipsometrie, Fourier-Transformations-Infrarotspektroskopie, Photoconductive Decay und SPV-Messungen können wir schließen, dass moderate Insertionen von O und N in a-Si:H zu einer Abnahme von optischen Parasiten führen Absorption bezogen auf eine höhere Bandlücke, unter Beibehaltung der Passivierungsqualität der Schichten.
Da diese Si-basierten Materialien in der Regel auch recht gute elektrische Eigenschaften aufweisen, könnten sie erfolgreich in SHJ-Solarzellen eingesetzt werden.
Die Messungen mit AFM und Kelvin Probe Force Mikroskopie (KPFM) an $LaVO_3$ haben deutlich gezeigt, dass dieses Material ein schlechtes Ladungstransportmedium ist und daher nicht für photovoltaische Anwendungen geeignet ist. Eine Lösung könnte sein, ein zusätzliches Elektronen- und Lochtransportmaterial in eine Struktur einzufügen, die farbstoffsensibilisierten Solarzellen ähnelt. Solch eine Struktur besitzt eine große Anzahl interner Schnittstellen zwischen den einzelnen Solarabsorbern und den nanostrukturierten Ladungstransportmedien, wodurch die Trennung und Sammlung von photogenerierten Elektronenlochpaaren ermöglicht wird.
Die Analyse von InGaN und AlGaInN durch SPV-Messungen hat gezeigt, wie verschiedene Parameter wie Elementzusammensetzung, Si-Dotierung und Spannungsrelaxation mit auftretenden Versetzungen oder Pinholes die Grenzflächenqualität der Schicht mit dem Substrat beeinflussen können. Im Allgemeinen verursachen ein geringer In-Gehalt, eine Si-Dotierung und keine Fehlstellenversetzungen in der InGaN / GaN-Struktur weniger Rekombinationsprozesse an der Grenzfläche. Während die Spannungsrelaxation (sowohl Zug- als auch Druckspannung) unter Bildung von Pinholes zu besseren Grenzflächen in den AlGaInN / GaN-Proben führt.

Table of contents

List of acronyms

2DEG - 2-Dimensional Electron Gas
III-N - III-group Nitrides
III-V - III-group and V-group alloys
ac-SPV - Surface PhotoVoltage at different chopper frequencies (method)
AFM - Atomic Force Microscopy
$Al_xIn_yGa_{1-x-y}N$, AlInGaN - Aluminium Indium Gallium Nitride
a-Si:H - hydrogenated amorphous silicon
a-SiO_x - amorphous silicon oxide
a-SiO_xN_y - amorphous silicon oxynitride
BP - BandPass
c-AFM - conductive Atomic Force Microscopy
CAGR - Compound Annual Growth Rate
CdTe - cadmium telluride
CIGS - copper indium gallium selenide
CO_2 - carbon dioxide
CPD - Contact Potential Difference
c-Si - crystalline silicon
CVD - Chemical Vapour Deposition
ECV - Electrochemical Capacitance-Voltage (technique)
EDD - Equivalent Disk Diameter
EDR - Equivalent Disk Radius
EFM - Electrical Force Microscopy
EPT - Energy Payback Time
DSSCs - Dye-Sensitized Solar Cells
FF - Fill Factor
FFT - Fast Fourier Transform
FTIR - Fourier Transform InfraRed (spectroscopy)
FZ-Si - Float Zone Silicon
GHG - GreenHouse Gas
HJ - HeteroJunction
HJ-IBC - HeteroJunction with Inter-digitated Back Contact
IBC - Inter-Digitated Back Contact
$In_xGa_{1-x}N$, InGaN - indium gallium nitride
IPCC - Intergovernmental Panel for Climate Change
I_{sc} - short circuit current

ITO - indium tin oxide
I-V - current voltage (characteristic)
J_{dark} - dark current density
J_{sc} - short circuit current density
KPFM - Kelvin Probe Force Microscopy
$LaVO_3$ - lanthanum-vanadium oxide
MD - Misfit Dislocation
MI - Mott Insulators
MIS - Metal-Insulator-Semiconductor (configuration)
MOCVD - Metal Organic Chemical Vapour Deposition
N_2O - nitrous oxide
nc-Si:H - hydrogenated nanocrystalline silicon
nc-SiO_xN_y - nanocrystalline silicon oxynitride
PCD - PhotoConductance Decay
PECVD - Plasma Enhanced Chemical Vapour Deposition
PV - PhotoVoltaics
QTH - Quartz Tungsten Halogen (lamp)
RE - Renewable Energies
RMS - Root Mean Square (roughness)
ROAP/CA - Rest Of Asia-Pacific & Central Asia
R_x - flux ratio or dilution
SCR - Surface Charge Region
SEM - Scanning Electron Microscopy
SHJ - Silicon HeteroJunction (solar cells)
SiH_4 - silane
SIMS - Secondary-Ion Mass Spectrometry
SPMs - Scanning Probe Microscopes
SPS - Surface Photovoltage Spectroscopy
SPV - Surface PhotoVoltage
STM - Scanning Tunnelling Microscope
V_{oc} - open circuit voltage
XRD - X-Ray powder Diffraction
ZnO - zinc oxide

Introduction

During the last 300 years, greenhouse gases (GHG) emissions in the atmosphere have increased at an unprecedent rate and level, due to the birth of industrialization [1]. These emissions dramatically contribute to the climate change, causing warming of the atmosphere and the oceans, and change in the global water cycle; furthermore, human activity is the dominant cause of all these changes [1]. For this reason, at the end of 2015 took place the so-called "Paris agreement", a call for the global community to adopt responsible strategies for a sustained reduction in GHGs emissions to limit the temperature increase to 1.5 °C above pre-industrial levels [2].

A solution to meet basic human energetic needs and at the same time provide low environmental impacts and GHGs emissions is represented by renewable energies (RE) [3]. Among RE, photovoltaics (PV) exploits a widely accessible and infinite solar resource, with the possibility of being installed in those communities without a connection to a main grid. At last, PV is regarded as a truly "green" energy resource due to low-impact manufacturing processes and recycling of discarded modules [4]. For all these reasons, PV is a fast-growing market, with the Si-wafer based PV as the leader technology, accounted for almost 95% of the total production in 2017 [5]. Moreover, in 2017 single-crystalline silicon (c-Si) solar cells have achieved a new world record efficiency of 26.7% [6].

Nonetheless, several new concepts have been developed to boost the efficiency of Si-based solar cells to achieve and even overcome its theoretical efficiency; for example, by using new materials to substitute either the absorber layer or the emitter layer.

Si-based PV technology has not been replaced yet, since alternative technologies based on new materials still lack stability (for example, in the case of perovskites) or have low efficiencies (in the case of III-group nitride ternary alloys). The solar cell performance is strictly correlated to the structure, composition, optical and electrical properties of the materials. Furthermore, since newest solar cells are generally based on heterostructures, the analysis of surface morphology at the nanoscale and the quality of the interface with the substrate is mandatory, those areas where the recombination processes mainly take place. A thorough study of the structure and composition of the materials, as well as an investigation on their surface and interface properties is then needed.

In this work, both innovative materials for Si based solar cells (as nanocrystalline and amorphous sub-stoichiometric silicon oxy-nitride and oxide thin films, nc-SiO_xN_y, a-SiO_xN_y and a-SiO_x) and materials for advanced solar cell concepts (as perovskite lanthanum-vanadium oxide, $LaVO_3$, thin films, and indium gallium nitride, $In_xGa_{1-x}N$, and aluminium indium gallium nitride, $Al_xIn_yGa_{1-x-y}N$, thin films) will be investigated by several techniques to extract the correlation between different deposition conditions and their properties.

- The first part of this work is based on the study of Si-based thin films deposited by plasma enhanced chemical vapour deposition technique (PECVD). In detail, boron-doped nc-SiO_xN_y, intrinsic a-SiO_x and a-SiO_xN_y thin films with different deposition parameters have been investigated by conductive atomic force microscopy (c-AFM) and surface photovoltage (SPV) spectroscopy techniques on transport and optical properties, and by a multi-characterization approach on structural and passivation properties, respectively.
  These materials are interesting since they can substitute hydrogenated amorphous silicon (a-Si:H) as the doped heteroemitter layer in silicon heterojunction (SHJ) solar cells, due to their lower parasitic absorption and contact resistance with the top layer.
  The aim of the study on the B doped nc-SiO_xN_y layers is the extraction of a model which explains the electrical conduction in these materials. The investigation has been extended also to doped hydrogenated nanocrystalline silicon (nc-Si:H) films to distinguish the role of O and N in the electrical conductivity. The influence of Si nanocrystal dimensions on impurity solubility and dopant efficiency has been underlined in several theoretical [7,8] and experimental studies [9,10]. However, this correlation is still unclear in more complex and multiphase structures, such as nc-SiO_xN_y layers. Within this framework, this first analysis provides a thorough investigation of nanoscale electrical properties of nc-SiO_xN_y thin films, where the samples differ in oxygen content and crystalline fraction. The research aims to collect information on the impact of oxygen and nitrogen, and subsequent B activation, on the sample electrical conductivity. Moreover, a consistent transport model for the highly conductive areas of the samples has been estimated through the extraction of current-voltage characteristics. SPV spectra have also been investigated to extract variations in the band gap and the overall absorption with the different composition and thermal treatment.

Furthermore, a-SiO_x and a-SiO_xN_y thin films have been investigated as fluxes of nitrous oxide (N_2O) or carbon dioxide (CO_2) gases vary in the reactor. The inclusion of O and/or N within the a-Si:H layer boosts its optical band gap, hindering the parasitic absorption process. Nevertheless, huge inclusion of these elements increases disorder and then promotes surface recombination.

Several techniques have been employed to clarify the changes in the interface structure of the amorphous network correlated with different N_2O and CO_2 fluxes during deposition. In detail, by Fourier-transform infrared spectroscopy (FTIR), spectral ellipsometry, SPV spectroscopy and photoconductance decay (PCD), several information on a-SiO_x and a-SiO_xN_y layers has been extracted: optical properties, light induced electronic transitions and minority carrier lifetimes. It is evident how relying on multiple characterization methods is essential to have an overall and complete evaluation of the surface/interface quality of thin films.

- The second part of the thesis consists of the analysis of an inorganic perovskite, $LaVO_3$, which is a transition metal oxide perovskite, intrinsically much more stable than hybrid organic-inorganic perovskites and thus more suitable as a candidate for photovoltaic devices based on perovskites. $LaVO_3$ thin films have been deposited both by sol-gel and sputtering techniques onto two different substrates (silicon and quartz) and, eventually, with zinc oxide on top, ZnO. In $LaVO_3$/ZnO junctions, AFM and Kelvin probe force microscopy (KPFM) analyses have been employed to extract $LaVO_3$ morphology, and ZnO and $LaVO_3$ work functions to predict the behaviour of the solar cell.
- The third part of the work deals with different III-group nitride alloys, which are quite interesting materials for solar cell and optoelectronic applications due to their wide tunability of both lattice parameters and optical band gap. InGaN and AlInGaN on GaN thin films have been deposited by metal organic chemical vapour deposition. SPV spectroscopy has allowed us to investigate the role of In content, misfit dislocations at the interface with the substrate, carrier density within the layers and the recombination processes at the interface.

The outline of the thesis is the following. Chapter 1 provides an introduction on renewable energy sources with photovoltaics as the front line. The role of different PV technologies has been explained. At last, the working principles of the photovoltaic cell have been presented.
In Chapter 2, the materials and their properties are listed and described.

In Chapter 3, the physical principles and the application of all the characterization methods used have been presented focusing on AFM, c-AFM, KPFM and SPV techniques.
In Chapter 4, the experimental details are listed for each technique.
Chapter 5 contains the results for each sample set.
At last, a conclusive section with final discussion and conclusions on the obtained results is presented.
nc-SiON, a-SiON and a-SiO thin films have been deposited at the Photovoltaics Division at University of Konstanz. LaVO samples have been deposited at MaCEPV (Materials for electronic and photovoltaic devices) laboratory, iCube, CNRS at University of Strasbourg, while InGaN and AlInGaN samples have been grown at AIXTRON laboratory at Herzogenrath. FTIR, spectral ellipsometry and PCD measurements have been performed at University of Konstanz, while AFM, c-AFM, KPFM and SPV measurements have been performed at University of Bologna.

1 Overview on photovoltaics

In this first Section, the importance of renewable energy technology is stressed out, with a peculiar attention on the solar cell technology. Furthermore, latest silicon-based technologies are described, as well as some new concept technologies based on inorganic perovskites and group-III nitride alloys. At last, some basic definitions concerning solar cell devices are illustrated.

1.1 Motivations for photovoltaics

During the past few thousand years, the production of greenhouse gases (GHGs) appeared to be compensated by the absorption through natural sinks within the atmosphere, maintaining their level fairly constant and a long-term equilibrium on Earth [1,11]. Nonetheless, since the beginning of the industrialization in the last 300 years, GHG emissions in the atmosphere have increased at an unprecedent rate and level [1]. The consequences are dramatic on the Earth's climate and on all the natural systems related to its cycles. The so-called “climate change” embraces warming of the atmosphere and the oceans, changes in the global water cycle, reductions in snow and ice and global mean sea level rise. All these modifications are able to affect natural and human systems all over the world [1]. According to the Intergovernmental Panel for Climate Change (IPCC) “human influence is extremely likely to have been the dominant cause of the observed global warming since the mid-20th century” [1]. Indeed, the diagram in Figure 1.1 shows that the main contribution (more than 70%) to the total anthropogenic GHGs emissions is CO_2 from fossil fuels combustion and industrial processes [1].
Many efforts have started to strengthen the global response to climate change, due to the present situation that will worsen with the exponential economic and population growth of the last century (global population forecasted to count more than 11 billion humans by the end of the century [12]). At the end of 2015, the so called “Paris agreement” took place as an historic global climate agreement at the 21st Conference of the Parties in Paris.

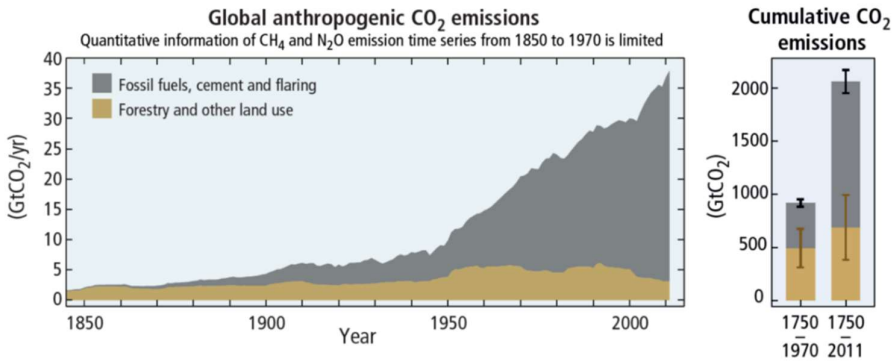

Figure 1.1 Global anthropogenic CO_2 emissions in gigatons of CO_2 equivalent per year from different sources. Cumulative emissions of CO_2 and their uncertainties shown as bars and whiskers, respectively, on the right [1].

It is a call for the global community to adopt responsible strategies for a substantial and sustained reduction in GHGs emissions, promoting actions to adapt to climate impacts, and setting mitigation targets [2]. The UN have also agreed on making efforts to limit the increase to 1.5 °C above pre-industrial levels [2]. A good compromise between meeting basic human energetic needs and providing low environmental impacts and GHGs emissions is represented by the use of renewable energies (RE) [3]. RE represent any form of energy from solar, geophysical or biological sources, replenished by natural processes at a rate equal or faster than its rate of use. They include resources such as biomass, solar energy, geothermal heat, hydropower, tide and waves, ocean thermal energy and wind energy. Essentially, the most promising large-scale carbon-free energy sources, capable of fulfilling the demand for electricity, are solar power-related technologies and nuclear power, whereas geothermal energy and tidal energy are significant only at a local scale [4]. Although nuclear plants emit no CO_2, they have quite serious unsolved issues, whereas the solar resource is widely accessible and essentially infinite: the amount of solar radiation arriving on Earth is 10 000 times the current energy consumption on the planet [4]. Photovoltaics (PV) represents the production of electricity via direct conversion of the solar energy through the use of photovoltaic cells. A great advantage of PV is its possibility of being installed in those communities where a connection to a main grid would be cost prohibited. Moreover, supported by a wide public acceptance, solar PV holds also the highest job-generating potential among the family of solar technologies [13]. At last, PV is regarded as a truly "green" energy resource also for the low

impact of manufacturing processes on the environment and the possibility to recycle the discarded modules [4].
For all these reasons, PV is a fast growing market: the Compound Annual Growth Rate (CAGR) of PV installations has been of 24% between year 2010 to 2017 [5]. Concerning PV module production in 2017, China&Taiwan hold the lead with a share of 70%, followed by Rest of Asia-Pacific & Central Asia (ROAP/CA) with 14.8%. Europe contributed with a share of 3.1% (compared to 4% in 2016); USA/CAN contributed 3.7%, as shown in Figure 1.2a [5]. In 2017, Europe's contribution to the total cumulative PV installations amounted to 28% (compared to 33% in 2016) (see Figure 1.2b). In contrast, installations in China accounted for 32% (compared to 26% in 2016) [5].
Si-wafer based PV technology accounted for about 95% of the total production in 2017. The share of multi-crystalline technology is now about 62% of total production (as reported in Figure 1.2c) [5]. The record lab cell efficiency is 26.7% for mono-crystalline and 22.3% for multi-crystalline silicon wafer-based technology. The highest lab efficiency in thin film technology is 22.9% for CIGS (copper indium gallium selenide) and 21.0% for CdTe (cadmium telluride) solar cells (see the chart in Figure 1.3a).
The Energy Payback Time (EPT) is used to measure how many years a system should operate to produce the energy required for its manufacture: after the payback time, all of the energy produced is truly new energy [4].
In 2017, the EPT PV systems were still dependent on the geographical location: PV systems in Northern Europe need around 2.5 years to balance the input energy, while PV systems in the South equal their energy input after 1.5 years and less, depending on the technology installed [5]. The Experience Curve – also called Learning Curve - shows that in the last 37 years the module price decreased by 24% with each doubling of the cumulated module production (see Figure 1.3b). Cost reductions result from economies of scale and technological improvements [5].
Though the Si-based solar cell technology still dominates in the PV market, different new ideas are catching on and developing to overcome the theoretical efficiency limit of Si. However, these new technologies are still not present in the market due to lack of stability (in the case of perovskites) or due to still low efficiencies (in the case of nitride ternary alloys). For all these reasons, a thorough study of the structure and composition of the materials is mandatory, as well as an investigation on their surface and interface properties. In this work, both innovative materials for Si based solar cells (nanocrystalline and amorphous sub-stoichiometric silicon oxy-nitride and oxide thin films) and

materials for advanced solar cell concepts (as indium gallium nitride and perovskite thin films) will be investigated by several techniques to extract how different deposition conditions can affect their properties.

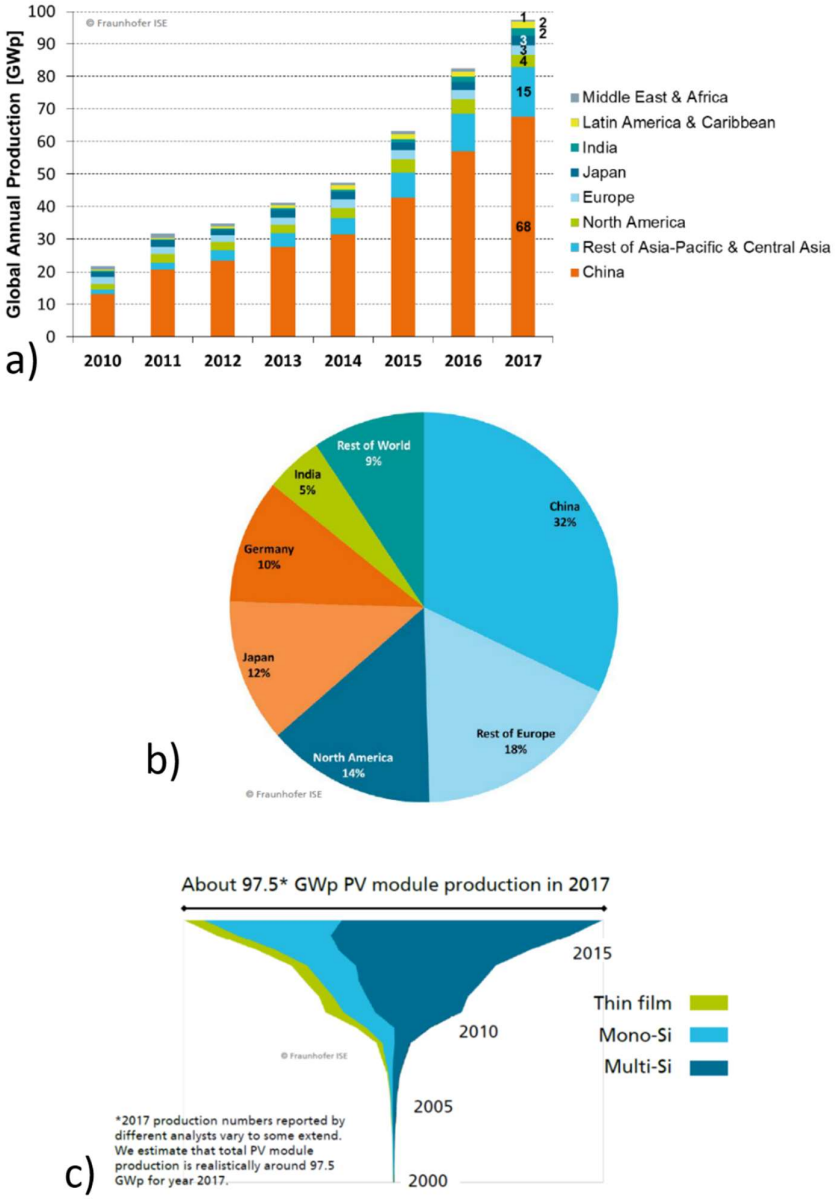

Figure 1.2 a) PV annual module production per year for each area of the world. b) Total cumulative PV installations in 2017. c) Module production, divided by technology [5].

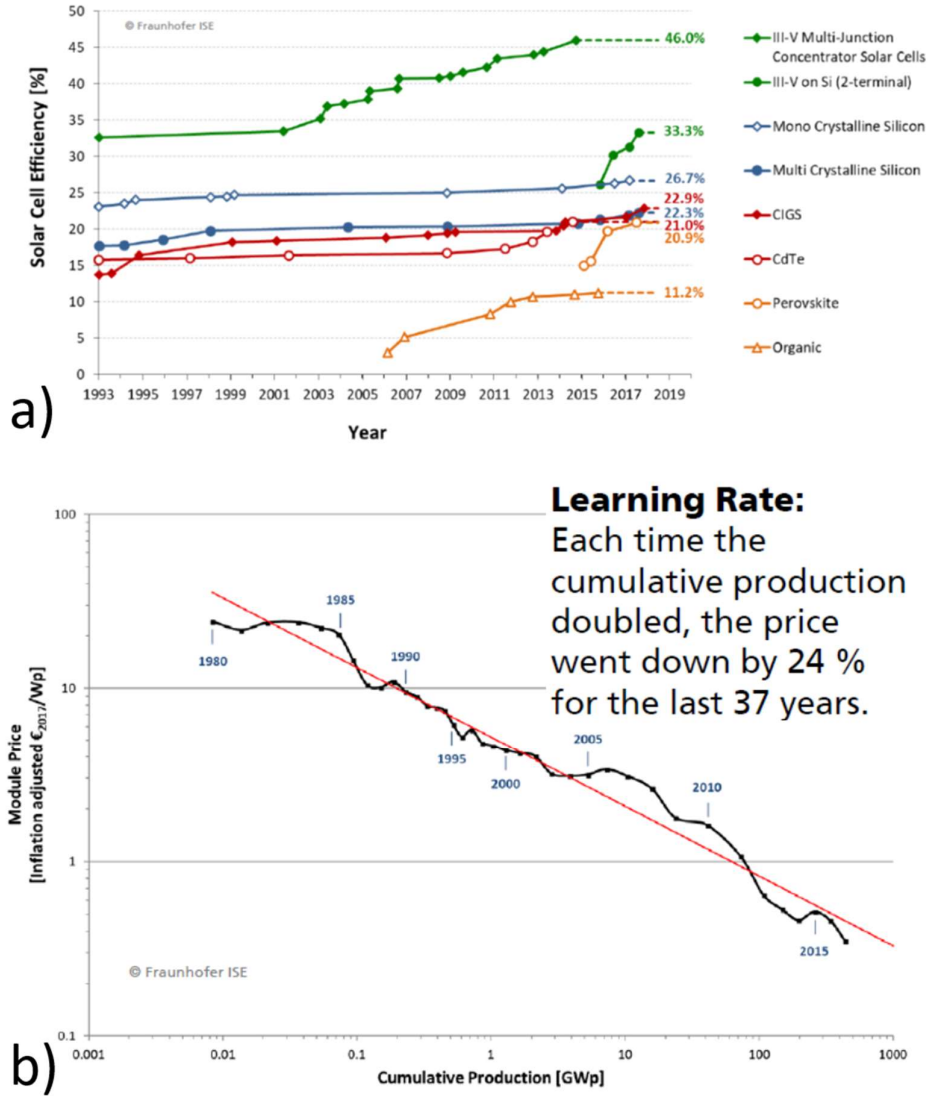

Figure 1.3 a) The record lab cell efficiency for different solar cell technologies. b) The Experience Curve with module prices as a function of cumulative production [5].

1.2 Silicon-based thin films in silicon heterojunction solar cells

After a steady improvement over the last decades, in 2017 single-crystalline silicon (c-Si) solar cells have achieved a new world record efficiency of 26.7% [6]. In addition, the photovoltaic module cost has dropped thanks to increased mass production associated with its technology maturity. Indeed, the drop in

costs has now gone so far that solar photovoltaic electricity has already reached grid parity in many countries and locations [14]. However, the advances in silicon ingot growth processes and in defect/contamination control during the whole cell fabrication are at the basis of this overall enhancement. Nowadays, the bulk electrical properties of the crystalline silicon wafers have reached such a high quality that obtaining further progresses in the device has become quite laborious. Innovative surface passivation schemes and an excellent interface control could be a way to overcome this new impasse.
Intrinsic hydrogenated amorphous silicon (a-Si:H) films have been used and studied for some decades as effective passivizing layers thanks to their passivation via chemical surface states [15]. The passivation is achieved by hydrogenation of Si dangling bonds, with a reduction of the surface defects [16]. An additional doping of the layers promotes also a field effect passivation, in combination with the detriment of the surface-states-related passivation. Both the films (intrinsic and doped) have been typically employed together in Si heterojunction (SHJ) solar cells, constituting the so-called "hetero-emitter stack". A sketch of the SHJ solar cell structure is reported in Figure 1.4 [15]. It has been shown that growing the doped layers directly on the c-Si absorber (in an n/c-Si/p configuration) causes a severe passivation loss due to doping-related defect generation in the amorphous host matrix [15]. Nevertheless, doped layers of a-Si:H (red and green layers in Figure 1.4) are essential to obtain the electric field that could separate the carriers of different sign and accelerate them in the external circuit [15]. For these reasons, a few nm thick buffer layer of intrinsic a-Si:H is inserted between the c-Si substrate (violet layer in the sketch) and the doped film (orange layers) to preserve both passivation and doping. In 2014 this strategy has led Sanyo, now Panasonic, to achieve a high efficiency SHJ cell of practical size of 25.6% [16].

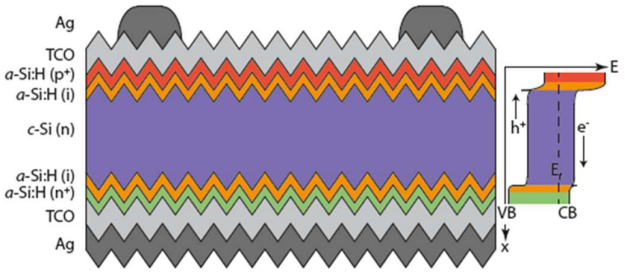

Figure 1.4 Sketch of a SHJ solar cell developed by Sanyo (Japan), named HIT®, with the corresponding band diagram on the right [15].

Recently, the role of surface passivation on the final efficiency of SHJ solar cells, together with reduced series resistance and optimised optical properties, has been shown by Yoshikawa et al. [17]. These authors combined the heterojunction (HJ) technology of SHJ with an inter-digitated back contact (IBC) one, obtaining solar cells with a certified efficiency larger than 26%. The IBC-structure advantage is the formation of all electrical collection regions and contacts for both carrier types at the rear side of the device [17]. In this way, the optimization of the front side can exclusively rely on optical and passivation properties, ignoring its carrier collection functionality. The scheme of the HJ-IBC solar cell is shown in Figure 1.5 [17].

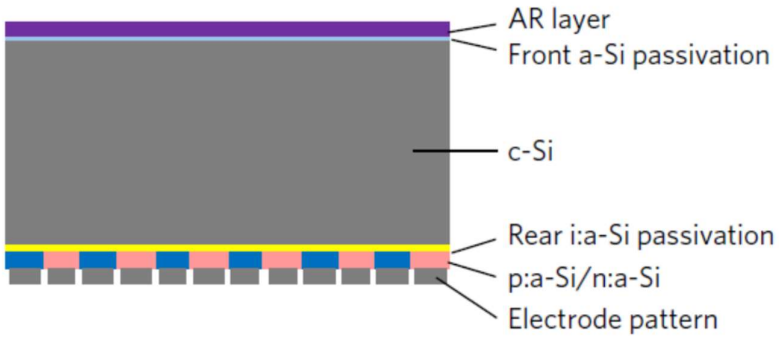

Figure 1.5 Cross-section scheme of the HJ-IBC solar cell [17]. AR layer stands for dielectric anti-reflection layer.

In this structure p-type amorphous Si (p:a-Si) and n-type amorphous Si (n:a-Si) layers are patterned at the rear side to collect holes and electrons, respectively. Both the front and the rear sides are covered by an a-Si passivation layer.
Notwithstanding the high efficiencies achieved by SHJ and HJ-IBC solar cells, a-Si:H films display high parasitic absorption of light; consequently, the short circuit current drops off and the series resistance increases, leading to a reduced fill factor (defined in Equation (1.7) in Section 1.5) [18]. A widening of the optical band gap could reduce the absorption process within the a-Si:H films. As an example, such a result can be achieved with the inclusion in the layers of elements like carbon, nitrogen and/or oxygen [18,19], while electrical conductivity can be improved by the introduction of crystalline phases in the amorphous matrix [19].

Although the passivation mechanisms at the a-Si:H/c-Si interface have been deeply investigated for at least one decade [20,21], a-Si:H layers with incorporation of small amounts of O and N, named here sub-stoichiometric hydrogenated amorphous silicon oxide (a-SiO_x) and silicon oxynitride (a-SiO_xN_y) thin films, are still not well-known materials.
These materials are innovative in different applications, *e.g.* as rear passivation layers in monocrystalline silicon solar cells [22,23], as buffer layers for organic based photodetectors [24] or as matrix layers for superlattices with Si nanocrystals [25–28]. Nonetheless, there is still not a clear overview on their fundamental properties, since these layers are complex sub-stoichiometric compounds containing different phases, whose properties drastically vary with the deposition method and subsequent annealing processes.
Moreover, the correlation between deposition conditions, *i.e.* different structures of the amorphous network, and passivation quality of surfaces and interfaces has not been clarified yet. However, as stated above, detailed knowledge and understanding of these mechanisms are mandatory for an additional optimization of the passivizing layer quality for SHJ solar cells.
Combining the intrinsic and doped a-SiO_xN_y films to hetero-emitter stacks, a very high implied open circuit voltage (defined in Equation (1.6)) of up to 733 mV on a 2 Ω·cm p-type float zone Si wafer has been already demonstrated [18]. Simulations have also revealed a short circuit current density gain (described in Section 1.5) of up to 1.85 mA/cm^2. As aforementioned, a further efficiency enhancement can be achieved by replacing the amorphous emitter layer with one containing a nanocrystalline (nc) phase, since the electrical conductivity increases and the contact resistance between the nc-emitter and the transparent conductive oxide (light-grey layer in Figure 1.4) lowers [29]. These SiO_xN_y layers revealed the presence of a Si crystallised fraction [19,30]; for this reason, we will call them nc-SiO_xN_y for sake of clarity.
In this perspective, sub-stoichiometric a-SiO_x and a-SiO_xN_y films have been studied varying the deposition parameters to link them to their optical and passivizing properties and nc-SiO_xN_y layers have been investigated in their electrical properties at the nanoscale and their surface photovoltage spectra and how they are both influenced by the O inclusion within the layers and an additional annealing step.

1.3 Perovskites in solar cell applications

Perovskite is a calcium titanium oxide mineral, composed of calcium titanate with the chemical formula $CaTiO_3$. The mineral was discovered in the Ural

Mountains of Russia by Gustav Rose in 1839 and named after Russian mineralogist Lev Perovski (1792–1856) [31]. The term "perovskite" and "perovskite structure" are often used interchangeably; nonetheless, the true perovskite (the mineral) is formed of calcium, titanium and oxygen, while a perovskite structure is anything with generic form ABX_3 and the same crystallographic structure as the perovskite mineral [32]. The perovskite lattice arrangement is shown in Figure 1.6 and can be represented as follows: a large atomic or molecular cation of type A in the centre of a cubic structure [32]. The corners of the cube are then occupied by atoms B (also cations) and the faces of the cube are occupied by smaller atoms X (anions) [32].

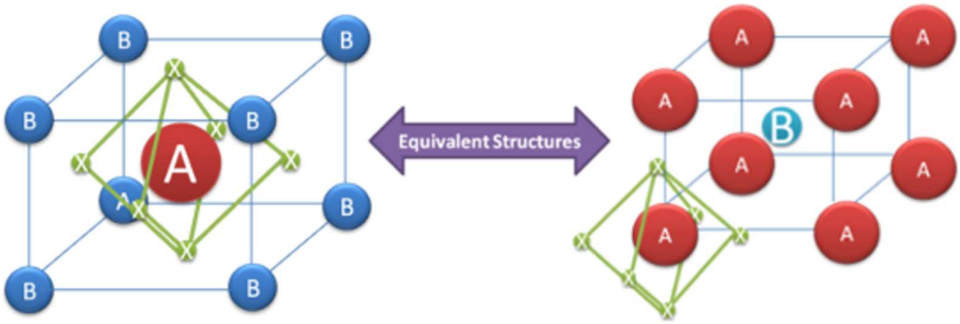

Figure 1.6 A generic perovskite crystal structure of the form ABX_3. Two equivalent structures are shown: left, the atom B is at the <0,0,0> position; right, the atom (or molecule) A is at the <0,0,0> position. Also note that the lines are a guide to represent crystal orientation rather than bonding patterns [32].

Depending on which atoms/molecules are used in the structure, perovskites can have an impressive array of interesting properties including superconductivity [33–35], giant magnetoresistance [36–38], spin-dependent transport (spintronics) [39,40] and catalytic properties [41,42]. Perovskites therefore represent an exciting playground for physicists, chemists and material scientists [32].
In the case of perovskite solar cells, the most efficient devices so far have been produced by employing hybrid organo-metal halide perovskites. This technology is quite new, since it was born in 2009 reporting an efficiency of 3.5% [43]. The sudden rise of perovskite PV begun in 2012, when an efficiency exceeding 9% was reached by two different groups of T. Miyasaka - H. J. Snaith [44] and G. Park - M. Grätzel [45]. In both works, a solid-state device structure was used, to avoid decomposition of the perovskite absorber in the electrolyte. Since 2012, several hundreds of papers have been published on this subject,

favoured by the simplicity and low cost of this technology, easily performable with very standard lab equipment.
In the last few years, the power conversion efficiency of mesoporous-type perovskite solar cells has increased to 23.3% by optimizing thin-film growth, interface, and absorber materials [46–48]. However, these materials are affected by instability, reliability and toxicity issues [49]. To overcome all these problems, research has moved towards alternative inorganic oxides with a perovskite structure. The big issue that affects this branch of materials is their quite large bandgap; indeed, the bandgap of the active layer in solar cells should be around 1.3 eV to perfectly match the solar spectrum of the Earth [50]. To date, cuprous oxide (Cu_2O) has been generally employed as the absorber layer with a bandgap of 2.1 eV, obtaining efficiencies around 4% [51]. One category of low bandgap oxides can be found among Mott insulators (MI). MI behave as insulators, although they are predicted to be conductors by band theories. Nonetheless, they can easily become conductive (by means of a Mott transition) due to strain, defects, oxygen stoichiometry, etc. [50]. Some examples are $LaVO_3$, $YTiO_3$, YVO_3, La_2CuO_4, Sm_2CuO_4, $LaMnO_3$ and $SrMnO_3$, and their band gaps and Shockley-Queisser limit[1] are reported in Figure 1.7. Not all of them are suitable for photovoltaic applications; indeed, among them, $YTiO_3$, YVO_3, $LaVO_3$ and $LaMnO_3$ have optical band gaps close to 1.1 eV, thus being interesting as absorber layers [50].
$LaVO_3$ is a p-type semiconductor and has an orthorhombic crystalline structure at room temperature. In two different research groups [52,53], it was shown that electronic reconstructions can take place at the interface of $LaVO_3/SrTiO_3$ junction creating conductive interfaces, due to the diffusion of oxygen vacancies in the $SrTiO_3$ substrate which promote metallicity of the interface. The heterostructures with such electronic reconstruction were theoretically proposed for solar cells, since the internal potential gradient could favour the separation of the photogenerated carriers [50]. Among the various $LaVO_3$-based solar cells, only a dye-sensitized solar cell[2] worked with very low

[1] For each incident spectrum, there is an optimum bandgap of the absorber at which the efficiency of the cell has a maximum, and, for a standard solar spectrum, this limit was reported by Shockley and Queisser in 1961 [74].

[2] Dye-sensitized solar cells (DSSCs) were invented by Michael Grätzel and Brian O'Regan in 1991. Where conventional systems take advantage of the semiconductor to both absorb light and transport charge carriers, DSSCs separate these two functions. A sensitizer, which is anchored to the surface of a wide band gap semiconductor, absorbs sunlight. When light is

efficiency (0.12%), probably due to trap-assisted recombination and consequent low minority carrier diffusion length [54,55]. An efficient strategy to overcome these issues involves tuning of carrier concentration in the material, varying the La/V ratio, oxygen stoichiometry, and/or introducing additional substituents for La or V [50]. In this perspective, this study has been performed on $LaVO_3$ thin films deposited with different techniques and on different substrates, to investigate their properties. In detail, we have focused on the surface characteristics at the nanoscale by means of atomic force microscopy (AFM). Afterwards, a ZnO/$LaVO_3$ p-n junction has been fabricated to obtain a solar cell architecture and it has been analysed by Kelvin probe force microscopy (KPFM) to extract the work function of ZnO and $LaVO_3$ and the barrier height of the junction. Indeed, for a high efficiency solar cell, an efficient charge separation is needed and thus a suitable corresponding heterojunction band structure. In this perspective, the evaluation of the $LaVO_3$ work function and the built-in barrier at the interface with ZnO is mandatory for a preliminary investigation on a successful operation of a solar cell.

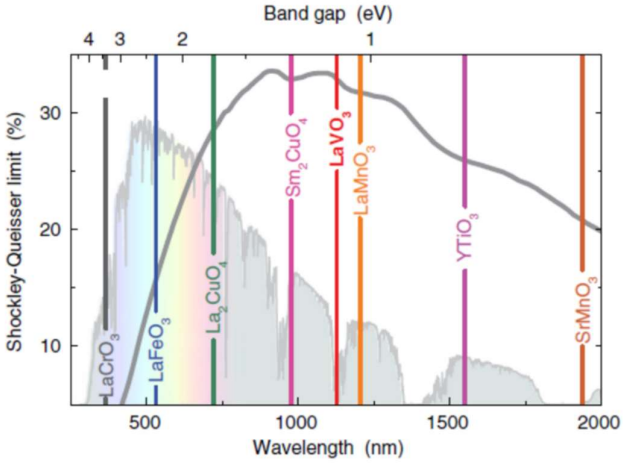

Figure 1.7 Shockley-Queisser limit as a function of band gap, along with the solar spectrum. The band gaps of various MI for solar cells application are marked [54].

1.4 Ternary and quaternary nitride alloys for photovoltaic applications

The nitride-based semiconductors, such as gallium nitride (GaN) and related alloys, have received enormous attention because of their broad range of

incident on the dye, electrons are injected from the dye into the conduction band of the semiconductor, accounting for the charge separation [55].

practical applications [56]. These semiconductors are always addressed as III-N alloys due to the bond between nitrogen (N) and elements belonging to the III-group of the periodic table [57]. III-N alloys form a continuous alloy system with direct band gaps, ranging from about 0.7 (indium nitride, InN) [58] to 6.2 eV (aluminium nitride AlN) [59] with 3.4 eV for GaN [60]. Band gaps adjustable from 0.7 to 6.2 eV can be achieved by suitable alloy combinations in the $In_xGa_{1-x}N$ and $Al_xGa_{1-x}N$ systems from which heterojunctions can be fabricated [56]. We can omit the element content in subscript for sake of brevity. The first studies on these materials have been heavily focused on Ga-rich InGaN and GaAlN alloys, due to their easier production; their bandgaps cover the blue and near-ultraviolet parts of the electromagnetic spectrum [57]. Afterwards, in the early 2000s, innovative deposition techniques such as metal-organic chemical vapour deposition (MOCVD) have drastically improved the material quality of InN and In-rich alloys. In this way, the studies have been spread also on In-based alloys, obtaining materials whose bandgap could cover also the low-energy visible spectrum towards the near infrared [57].
Indeed, the whole IR-vis-UV spectrum becomes accessible with mixed alloys of AlN, GaN and InN. The bandgap value of a ternary alloy lies between the bandgaps of its constituents. This property is described by the Vegard's law for ternary nitride alloys $A_xB_{1-x}N$, as follows:

$$E^g_{A_xB_{1-x}N} = E^g_{AN}x + E^g_{BN}(1-x) - b_{A,B}x(1-x) \tag{1.1}$$

where E^g_{AN} and E^g_{BN} are the energy gap values of the binary alloys. The bowing parameter $b_{A,B}$ strongly depends on the strain within the layer; for this reason, one can find several values for the same material [61]. A distinctive feature of III-Ns with respect to classical III-Vs (where V stands for an element of the V-group of the periodic table) is their crystal structure, since III-Ns adopt the wurtzite structure as stable phase, with hexagonal symmetry and lack of an inversion centre [62]. The basic wurtzite cell is illustrated in Figure 1.8, with a and c as lattice parameters. Classical III-Vs share instead the more symmetric, cubic zincblende structure [62].

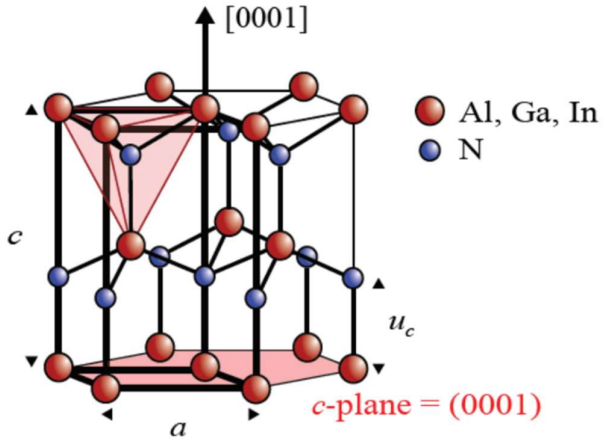

Figure 1.8 Wurtzite hexagonal unit cell. The a and c lattice constants with the c-axis direction and the basal c-plane are indicated [62].

The lattice constants are also tunable in the ternary alloys, following a linear Vegard's law [57]:

$$a_{AB} = x a_A + (1 - x) a_B \tag{1.2}$$

where a_A, a_B and a_{AB} are the lattice constants of A-N, B-N and AB-N alloys, respectively. Due to the properties of tunability of both lattice parameters and energy band gap, heterostructures of binary and ternary alloys can be built up. III-N devices and heterostructures are generally grown along the c-axis, then a lattice constant is the most meaningful one when considering heterostructures [62]. In Figure 1.9 the band gaps and lattice constants of nitride semiconductors alloys compared to other III-Vs are shown [62]. With a closer look to the plot, it can be noted that the only ternary III-nitride semiconductor lattice-matched to GaN is InAlN, with an In content of 17-18%, a strain-free condition that is one of its key advantages [63]. InGaN alloys and In-rich InAlN (In>17%) are subject to compressive stress when grown pseudomorphically on GaN [62]. One of the main consequences of the wurtzite structure and ionic character of the III-N bonding is the spontaneous polarization of III-N materials. In addition, compressive or tensile strain in pseudomorphic heterostructures introduces a piezoelectric polarization. The presence of polarization-induced interface charges has a strong impact on the band profile and charge distribution of III-nitride heterostructure, with induced electric fields reaching several MV/cm. The electric field effect is a huge band bending at the interface and a creation of a 2-dimensional electron gas (2DEG), exploited in high electron mobility heterostructures [62]. Practically, a barrier layer is

grown on top of GaN, with a wider bandgap than GaN's and a polarization capable of inducing a positive polarization charge at the interface. Suitable barrier materials are therefore AlGaN and InAlN with In<30% [62].
Since it constitutes a continuous alloy system, III-N group has been considered a promising system for semiconductor device applications since 1970, especially for the development of blue and UV light-emitting diodes. Other advantages include high mechanical and thermal stability, large piezoelectric constants and the possibility of passivation by forming thin layers of Ga_2O_3 or Al_2O_3 with bandgaps of approximately 4.2 eV and 9 eV [64]. The spontaneous and piezoelectric polarization of the wurtzite structure and the high electron drift velocities ($2 \cdot 10^5$ ms^{-1}) of GaN can be exploited for the fabrication of high-power transistors based on AlGaN/GaN heterostructures [64]. In ad-

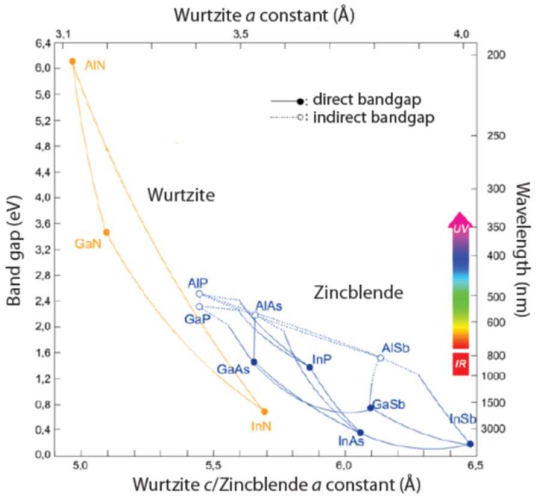

Figure 1.9 Band gap as a function of lattice constant for wurtzite III-N (orange symbols) and classical zincblende III-V semiconductors (blue symbols) [62].

dition, AlN can be employed in passive barrier layers, high-frequency acoustic wave devices, high-temperature windows, and dielectric optical enhancement layers in magneto-optic multilayer structures [64]. The re-evaluation of the InN bandgap [58] and subsequent findings have had a significant impact on device applications of III-N group. The bandgap of InGaN alloys ranging from 0.64 to 3.42 eV provides almost a perfect match to the solar spectrum, as shown in Figure 1.10. This property opens up an interesting opportunity for high-efficiency solar cells application of III-Ns [57].

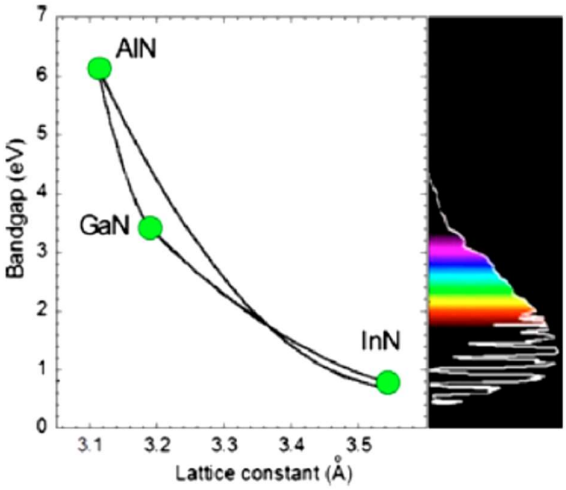

Figure 1.10 The bandgap of the group III-N alloys as a function of the a-axis lattice constant compared to the solar spectrum [57].

InN and InGaN have also other advantages for solar cell applications: superior resistance against high-energy particle radiation, which makes them suitable for space applications; possible strong phonon bottleneck effect to slow down hot-carrier cooling; advantageous band alignment with respect to silicon, naturally formation of a recombination junction with a Si base [57]. Since InGaN first proposal for solar cell applications [65], significant efforts and progress have been made, with coexisting great opportunities and issues [57].
Recently, a pure $In_{0.08}Ga_{0.92}N$ p-n junction has recently shown a fill factor of 62% and a conversion efficiency of 0.39%, which is quite low [66].
The III-N alloys also tend to exhibit very strong absorption at the band edge ($\sim 10^5$ cm^{-1}), allowing an absorption of a large fraction of incident light in a few hundred nanometres of material. This thickness is quite little as compared to the tens or hundreds of microns of material necessary in traditional Si solar cells [67]. One of the key issues for increasing the efficiency of the devices is the reduction in dislocations, as they act as non-radiative recombination centres. The generation of misfit dislocations (MDs) is a well-known phenomenon in heteroepitaxy, occurring as a thin epilayer is grown on a substrate with significantly different lattice parameters. Below a certain epilayer thickness, called the critical thickness, an epilayer may be grown pseudomorphically on a substrate, while a relaxation of misfit strain via plastic flow occurs for thicker epilayers (see Figure 1.11a in the case of compressive strain) [68]. In Figure 1.11b, the critical thickness as a function of the In content is reported

for an InGaN/GaN system, comparing two different approximation methods [69].

Recently, $Al_xIn_yGa_{1-x-y}N$ quaternary alloys have been recognized to have the potential to overcome some shortfalls of GaN epilayers, of InGaN and AlGaN alloys. By varying In and Al compositions in these alloys, one can change the energy band gap while keeping the lattice matched with GaN [70]. In detail, this quaternary material allows almost independent control of the lattice mismatch and, therefore, piezoelectric doping, and of the band offset in AlInGaN-based heterostructures [71]. In addition to these key features, AlInGaN quaternary alloys could also provide a better thermal match to GaN, which represents an important advantage in epitaxial growth. The potential applications of InAlGaN quaternary alloys are several, among which InGaN/InAlGaN quantum well light emitters, GaN/InAlGaN heterojunction field-effect transistors, and UV detectors [70].

Due to their versatility in several application fields, the III-N layers are still interesting and a subject of study. We have studied several layers of both $In_xGa_{1-x}N$ and $Al_xIn_yGa_{1-x-y}N$ grown on GaN with different deposition conditions. The layers then differ in their composition and a thorough analysis on how these variations affect the interface and electrical properties has been performed.

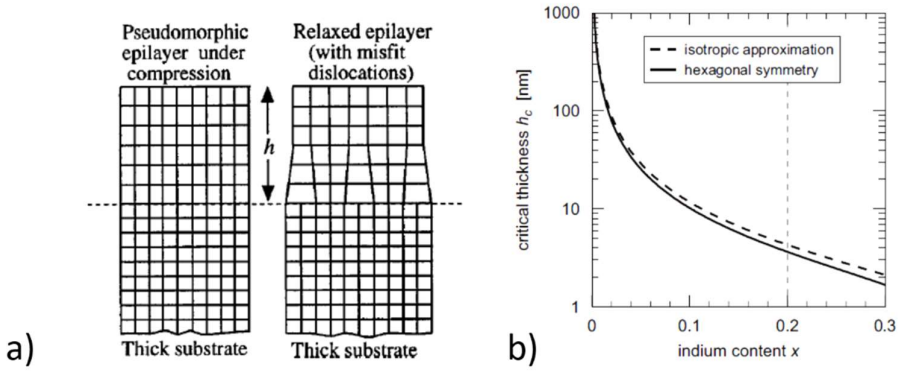

Figure 1.11 a) Structure of an epilayer under biaxial compression: pseudomorphic (left) and relaxed with misfit dislocations (right) [68]. b) The calculated critical thickness *vs.* In content curves for a single-layer InGaN/GaN system. The two curves correspond to the isotropic approximation (dashed line) and to the energy balance model (solid line) [69].

1.5 Basic definitions in solar cells

A solar cell or photovoltaic cell is a device that directly converts sunlight into electricity through the photovoltaic effect [72]. In a photovoltaic device, the absorption of incident photons of the radiant energy occurs, promoting the generation of electron-hole pairs through band-to-band transitions in the semiconductor. Photovoltaic energy conversion results from charge generation, separation and transport [73,74]. To avoid the instantaneous recombination of the carriers, *i.e.* the excited electrons relaxation to their ground state, a built-in electric field is needed. Then, these particles diffuse through the semiconductor and ultimately encounter an energy barrier that allows only charged particles of one sign to pass, reflecting the others: a p-n junction [73]. At this point, the charges can be collected at the contacts and driven through a load in an external circuit [74]. The effect is known as photovoltaic conversion.

As the basic structure in a PV system, the solar cell can be schematised as a two terminal device which acts like a diode in the dark and produces photovoltage under the Sun's illumination. Since a single cell can produce modest DC photovoltages (0.5 - 1 V), typically 28 to 36 cells are connected in series to form a module, to produce a DC output voltage of 12 V. A charge storage system is needed, due to changes in the illumination during the day [74].

The solar cell, illuminated by light, works as a battery in a simple electronic circuit. The open-circuit voltage V_{oc} is the maximum voltage available from a solar cell, occurring at zero current. It corresponds to the amount of forward bias on the solar cell due to the present bias of the junction with the light-generated current [75]. Whereas, the photocurrent created when the terminals are connected is called the short circuit current I_{sc}. For any intermediate load resistance R_L, a voltage V between 0 and V_{oc} is established and the cell delivers a current $I = V/R_L$, determined by the current-voltage characteristic of the cell under illumination [74].

A maximization of both the short circuit current density J_{sc} and V_{oc} is needed to achieve better performance of the solar cell. For high J_{sc}, the absorber material (the active region of the device, where most of the photogeneration occurs) should have high minority carrier lifetime, high carrier mobility, and absorption in a wide wavelength range; whereas, the bandgap and the transport mechanism of the material affect V_{oc} [76]. J_{sc} is related to the incident light through the quantum efficiency $QE(E)$ of the cell, defined as the probability of an incident photon of energy E to deliver one electron to the external circuit:

$$J_{sc} = q \int b_s\,(E)\; QE(E) dE \tag{1.3}$$

where b_s is the number of photons of energy between E and $E + dE$ incident to a unit area in a unit time and q is the electronic charge. QE is an incisive quantity to compare solar cell performances under different conditions, since it does not depend on the incident light spectrum [74]. A solar cell in dark acts as a p-n junction; therefore, free carriers flow in the opposite direction of the photocurrent, constituting the dark current density J_{dark} under an applied bias V. This quantity follows an exponential law:

$$J_{dark}(V) = J_0(e^{eV/Ak_BT} - 1) \tag{1.4}$$

where J_0 represents the reverse saturation current of the diode, A the ideality factor, k_B the Boltzmann's constant and T the temperature in the device. Following the superposition approximation, the net current $J(V)$ can be approximated as the sum of the short circuit photocurrent and the dark current. By Equations (1.3) and (1.4), the net current density is:

$$J(V) = J_{dark}(V) - J_{sc} \tag{1.5}$$

since the two currents have opposite signs. Then, the open circuit voltage V_{oc} can be expressed as:

$$V_{oc} = \frac{Ak_BT}{q} \ln\left(\frac{J_{sc}}{J_0} + 1\right) \tag{1.6}$$

and it increases logarithmically with light intensity [74]. Typical ideal $J(V)$ curves are depicted in Figure 1.12 [77].

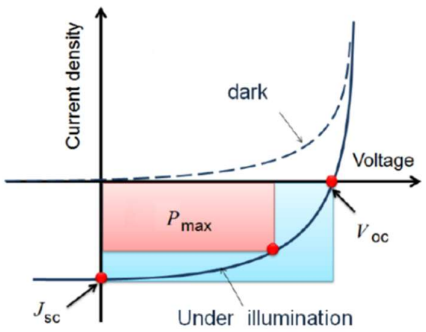

Figure 1.12 Curves of net current density *vs.* voltage, under illumination (solid line) and in the dark (dashed line) for a solar cell [77].

The operating range of the solar cell is from 0 to V_{oc}, where the cell delivers a power density $P = JV$; its maximum occurs at some voltage V_{max} and some current density J_{max}, as shown in Figure 1.13 [78].
The "squareness" of the J-V curve is described by the fill factor FF:

$$FF = \frac{J_{max}V_{max}}{J_{sc}V_{oc}} \tag{1.7}$$

At last, the efficiency is defined as the ratio between the power density generated at operating point and the incident light power density P_{rad}:

$$\eta = \frac{J_{max}V_{max}}{P_{rad}} \tag{1.8}$$

Through short circuit current density, open circuit voltage, fill factor and efficiency one can evaluate the performance of a solar cell under a particular illumination condition [74].

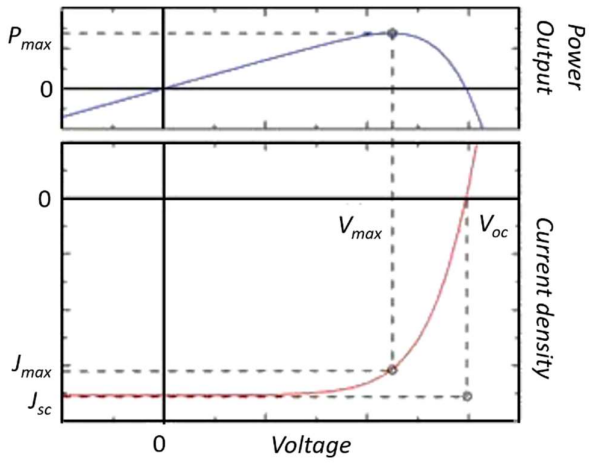

Figure 1.13 The power curve (top) and the J-V characteristic (bottom) curves. It should be noticed that when a certain balance of current and voltage occurs, power results maximized [78].

2 Materials

In this chapter all the sample characteristics and deposition conditions have been reported.

2.1 Nanocrystalline SiO_xN_y thin films

p-type nc-SiO_xN_y layers are deposited by plasma enhanced chemical vapour deposition (PECVD) on intrinsic float zone silicon (FZ-Si) substrate with a commercial system (PlasmaLab 100 from Oxford Instrument) in a parallel plate configuration with a radiofrequency of 13.56 MHz. The materials have been deposited at the Department of Physics of the University of Konstanz, in detail at Photovoltaics Division. The deposition temperature is always 300 °C. Silane (SiH_4), hydrogen (H_2) and nitrous oxide (N_2O) are used as precursor gases. Diborane (B_2H_6) diluted in hydrogen (0.5%) has been added, since boron inclusion donates a p-type doping.
All gas ratios are referred to their dilution in silane. Their ratios are then generally defined as:

$$R_X = \frac{[X]}{[X] + [SiH_4]} \tag{2.1}$$

where the square brackets represent the gas concentrations and X stands for N_2O, B_2H_6 or H_2. Diborane ratio is $R_{B_2H_6} = 2.34\%$ during deposition for all nc-SiO_xN_y layers; they have been eventually annealed at 800 °C in a nitrogen atmosphere to promote nanocrystals formation. This additional thermal step could be avoided and replaced by the introduction of higher H_2 fluxes during the deposition process. Indeed, the annealing step is not suitable for the whole solar cell production, since it is a high-priced process and implicates even the unwanted recrystallization of amorphous pre-deposited stacked layers. Unfortunately, our deposition system cannot reach such high H_2 fluxes in this setting, so we decided to introduce a thermal treatment instead.
To make a comparison, also nanocrystalline hydrogenated silicon (nc-Si:H) layers have been deposited and measured. Differently from nc-SiO_xN_y samples, B-doped nc-Si:H thin layers have been deposited by PECVD on FZ-Si at 225 °C, using only SiH_4, H_2 and B_2H_6 as precursor gases. The hydrogen dilution (defined in Equation (2.1)) of the nc-Si:H samples is $R_{H_2} = 91\%$.
Some deposition parameters, such as nitrous oxide and diborane dilutions, and annealing time, as well as few properties (thickness and crystalline

fraction) of all the samples are reported in Table 2.1. From cross-section scanning electron microscopy (SEM) analysis, it is evident that the nanocrystals in these layers are randomly distributed with no preferential orientation [30].

Sample (label)	R_{N2O} (%)	Annealing (h)	R_{B2H6} (%)	Thickness (nm)	Crystalline fraction
nc-SiO_xN_y (L3h)	9.09	3	2.34	209	88
nc-SiO_xN_y (L0h)	9.09	0	2.34	209	67
nc-SiO_xN_y (H3h)	47.4	3	2.34	283	70
nc-Si:H (Sit)	0	0	2	18	<5
nc-Si:H (SiT)	0	0	2	55	60

Table 2.1 Deposition parameters and properties of all the nanocrystalline silicon-based investigated samples.

The samples are labelled according to their annealing time; the as-deposited samples are referred to as 0 h. Moreover, the letters are also explanatory, since: "L" stands for low, while "H" for high (N_2O dilution); "t" as thin and "T" as thick (thickness), as the deposition time is the only parameter that changes in the nc-Si:H samples.
The thickness has been calculated by spectral ellipsometry measurements, while the Si crystallized fraction χ has been extracted by Raman spectroscopy [19]. To avoid recrystallization within the layers during the Raman spectroscopy, a power of 20 mW has been used for a 488 nm excitation laser.
The Si crystallized fraction has been obtained on layers deposited on a glass substrate using the following expression:

$$\chi = \frac{I_C}{I_C + I_A} \tag{2.2}$$

where I_A is the integrated area of the peak at 480 cm^{-1} related to the transversal optic mode of the amorphous component and I_C is the integrated area of the peak at 520 cm^{-1} related to the crystalline phase in the Raman spectra [19].
An example of the Raman spectrum is reported in Figure 2.1. While the amorphous peak is modelled as a Gaussian curve, the crystalline one is described by a Lorentzian curve [30,79]. In this way the crystalline fraction of the samples is comparable, since it is not possible to determine the absolute crystallinity of these multi-phase layers.

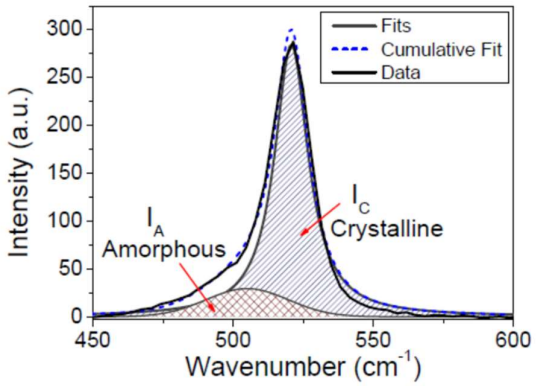

Figure 2.1 Raman spectrum of sample L3h. The fits of the single peaks (solid lines) and the cumulative one (dashed line) are present [30,79].

In previous studies, an impact of both nitrous oxide dilution and thermal treatment on the properties of the samples has been demonstrated. Firstly, introducing higher N_2O dilution during deposition leads to an increased inclusion of O within the layers, while N content remains almost the same [18]. So, high nitrous oxide dilution corresponds to a higher oxygen content, while a low N_2O dilution is related to a lower oxygen content.
Secondly, both the varied parameters in the nc-SiO_xN_y sample family, such as N_2O dilution and annealing, provoke a variation in the crystallinity fraction within the layers. This property is strictly correlated with the macroscopic electrical properties of the samples; indeed, the higher the crystalline fraction, the better the electrical conduction [19]. Therefore, the samples with higher oxygen content (related to a lower χ) show worse macroscopic electrical properties, while the annealing process promotes the recrystallization, and so the electrical conduction [19]. The electrical conductivity enhancement with annealing is probably correlated to an oxygen relocation after the treatment and the subsequent formation of O- and Si-rich areas within the samples [19].
Moreover, our previous studies have concluded that annealing also affects surface morphological properties of the samples, as surface roughness and dimensions of surface structures. This last nanoscale information on the surface structures has been extracted from AFM maps. Their size is 1×1 μm^2 with a resolution of 512×512 px. The maps have been acquired with a Park NX10 system in non-contact mode. Super-sharp apex tips have been used, with a curvature radius less than 5 nm (Nanosensors SSS-NCHR).

The investigation of surface morphology is also essential, since every surface becomes an interface in an HJ structure; therefore, as stated above, the overall interface quality affects the performances of the final device [80].
Interesting quantities have been extracted from the AFM maps using two different sources: the height–height correlation function (*HHCF*) of single maps and a superimposed segmentation mask obtained using Gwyddion software [81].
The *HHCF* is defined as follows [82]:

$$HHCF(r) = \frac{1}{N(M-m)} \sum_{l=1}^{n} \sum_{n=1}^{M-m} (z_{n+m,l} - z_{n,l})^2 \tag{2.3}$$

where N and M are the horizontal and vertical dimensions in pixels of the map, z is the recorded height for each point of the matrix and m is correlated with the sampling interval Δx of the measurement [82]:

$$m = \frac{r}{\Delta x} \tag{2.4}$$

in which r corresponds to the lateral distance between two points [83]. Assuming the surfaces of the samples approximately self-affine, the *HHCF* can be written in a simpler exponential form, from which several parameters can be estimated [83]. *HHCF* can be written as follows:

$$HHCF(r) = 2R_{HHCF}^2 \left\{ 1 - \exp\left[- \left(\frac{r}{\xi} \right)^{2\alpha} \right] \right\} \tag{2.5}$$

with R_{HHCF} the surface roughness, α the Hurst exponent and ξ the lateral correlation length. ξ represents the length scale beyond which the heights of two points of the surface are no more correlated and $\alpha \in [0,1]$ is a measure of the local roughness of the surface structures [83,84].
A better explanation of how the Hurst exponent change affects the surface morphology is visibly shown in Figure 2.2.

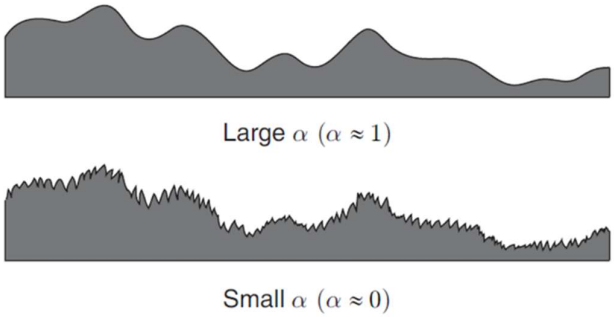

Figure 2.2 Local surface morphology for surfaces with different values of α. Smoother surfaces with larger values of α (top figure); rougher surfaces with $\alpha \approx 0$ (bottom figure) [83].

From the segmentation mask, an equivalent disk radius (EDR) of the surface structures can be derived [81]. The surface features are grain-like; then, they will be called grains from now on. To remove incorrectly identified grains, an additional filtering step was needed [85]. For this reason, grains with very small areas (< 4 px) and minimum height value less than the minimum height + 1 nm are removed from the analysis.
The AFM map of sample L3h with the superimposed mask is shown in Figure 2.3. The grain-like structure is clearly visible.
The analysis has been performed on samples with the same deposition parameters as sample L3h (see Table 2.1), *i.e.* low O inclusion, but with different annealing times: 0, 3 and 6 hours. Additional information on the crystalline fraction of these samples (extracted with the previously discussed method from Raman spectroscopy) is reported in Table 2.2.

Annealing time (h)	χ (%)	ξ (nm)	R_{HHCF} (nm)	EDR (nm)
0	67±2	18.5±0.2	1.204±0.001	8.21±0.03
3	88±2	23.8±0.2	1.369±0.001	8.56±0.03
6	86±2	26.6±0.4	1.476±0.002	9.66±0.04

Table 2.2 Crystalline fraction χ, lateral correlation length ξ, roughness R_{HHCF} and equivalent disk radius EDR for nc-SiO_xN_y samples with same deposition conditions but different annealing times. The reported errors are statistical.

It has been shown that annealing affects the layer morphology: surface roughness and dimensions of surface structures increase in the annealed samples. Indeed, both *HHCF* and grain size analyses indicate the presence of larger structures on the sample surfaces, as indicated in Table 2.2. In addition, the

equivalent disk diameter (EDD), twice the EDR, is of the same order of the lateral correlation length, but always smaller. This fact can be explained considering that ξ is sensitive to clustering of grains, while EDD resolves individual grains [85]. We can conclude that annealing promotes the formation of bigger structures on the surface that likely coalesce with each other.

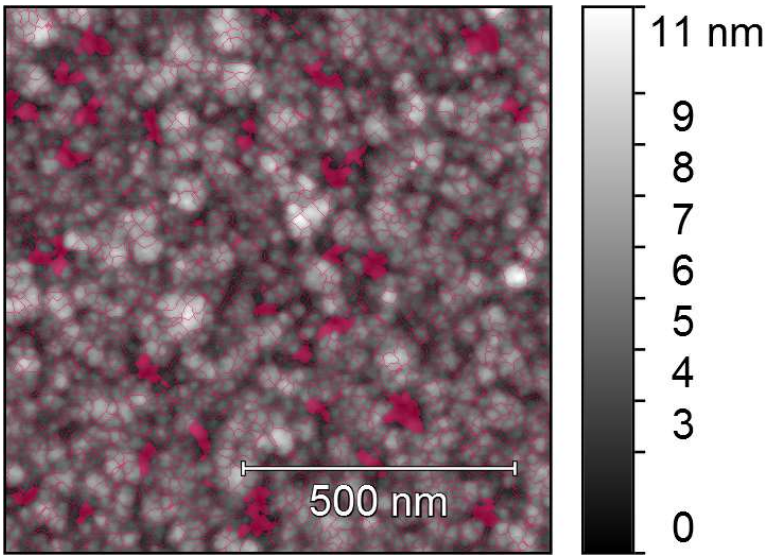

Figure 2.3 AFM map of sample L3h, with the superimposed mask (in pink). The mask has been inverted for sake of clarity. The filled areas in pink are the areas avoided by the filtering step [86].

In conclusion, a change in the macroscopic electrical properties of the samples, as well as a variation in the microscopic structure of the layers occur, as N_2O dilution differs or an annealing step is added. In this perspective, we expected also a modification of the electrical properties at the nanoscale.

2.2 Amorphous SiO_x and SiO_xN_y thin films

The a-SiO_xN_y (N sample set) and a-SiO_x (C sample set) layers have been deposited by PECVD on 250 μm thick boron-doped FZ silicon (5×5 cm^2, 2 Ω·cm, (100)-oriented) using the same PlasmaLab 100 commercial tool from Oxford Instruments available at the Photovoltaics Division of the University of Konstanz. All the parameters have been kept constant for all depositions (P=100 W, p=450 mTorr, T=175 °C, electrode distance d=20 mm, deposition time t=150 s). The exception occurs for the N_2O or CO_2 gas fluxes, added with pure SiH_4 gas to the plasma. The dilution ratios have been previously

defined in Equation (2.1) and it is also valid for $X = CO_2$. The N_2O and CO_2 ratios ranges are 4.8–16.6% and 4.8–9.1%, respectively. It is noticeable that the second range is smaller than the first. This has been a conscious decision, related to the double O-availability of a CO_2 molecule with respect to an N_2O molecule. A reference of a-Si:H layer was deposited using exclusively pure SiH_4 gas. The labels of the samples and the gas dilutions are listed in Table 2.3.

Sample (label)	R_{N2O} (%)	R_{CO2} (%)
N4.8	4.8	0
N9.1	9.1	0
N13	13	0
N16.6	16.6	0
C4.8	0	4.8
C7	0	7
C9.1	0	9.1
Ref	0	0

Table 2.3 Information of the a-SiO_x and a-SiO_xN_y investigated samples: labels, N_2O and CO_2 fluxes.

The samples were dipped in a 2% hydrofluoric acid solution before each deposition to remove natural silicon oxide layer from the surfaces. The deposition has been performed on both sides for each sample in separate depositions and in-between each deposition the deposition chamber has been cleaned. The layer thicknesses vary between 100 and 140 nm; these differences are correlated with the changes in the plasma composition in each deposition. An additional annealing step on a hotplate in ambient air at 300 °C for 15 min was performed to activate the passivation at the interface with the substrate [18]. In Figure 2.4, the interface between a-SiO_xN_y/a-SiO_x top layers (right) and the c-Si substrate (left) is shown, highlighting the band diagrams and their bending in proximity of the interface. In addition, the possible electronic transitions under illumination are sketched in different colours. This indication is useful to better identify the electronic transitions in the SPV spectra (see Section 3.4.1). In the sketch a lower limit of the band gap at 2 eV has been considered for the top layer, while values range from 2 to 3 eV in literature [18,87].

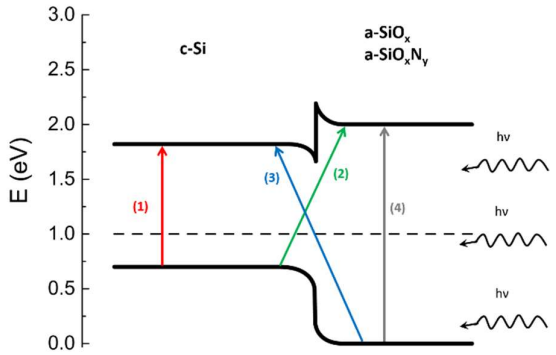

Figure 2.4 Sketch of the band diagram of a-SiO_x and a-SiO_xN_y layers (right) at the interface with the c-Si substrate (left). The possible electronic transitions under illumination are highlighted with numbers and arrows of different colours. A 2-eV bandgap for the top layer has been considered.

The possible transitions are listed as follows:
(1) in the c-Si substrate: band-to-band transition at around 1.1 eV;
(2) at the interface (c-Si→top-layer): crossing transition from the c-Si valence band to the top layer conduction band at around 1.3 eV;
(3) at the interface (top layer→c-Si): transition from the top-layer valence band to c-Si conduction band at around 1.8 eV;
(4) in the top layer: band-to-band transition at around 2 eV.
The scheme of Figure 2.4 is only a rough indication for the SPV effective transitions under illumination, since the effective band diagram is more complicated as the layers are amorphous and disordered.
In this overview, a thorough analysis of a-SiO_x and a-SiO_xN_y layers performed by means of different techniques could be interesting, with the aim of investigating changes in several properties of the layers, as gas dilutions vary during deposition.

2.3 $LaVO_3$ thin films

The $LaVO_3$-based samples investigated in this work were deposited by sol-gel and magnetron sputtering procedures on different substrates at the MaCEPV (Materials for electronic and photovoltaic devices) laboratory, iCube, CNRS at Université de Strasbourg. The experimental details on the fabrication procedures are reported elsewhere [50]. Additional ZnO/$LaVO_3$ junctions have been fabricated to simulate a solar cell architecture. The sample characteristics and labels are reported in Table 2.4 [88].

Label	ZnO thickness (nm)	$LaVO_3$ thickness (nm)	Technique	Substrate
LVO55Q	-	55	sputtering	quartz
LVO55S	-	55	sputtering	silicon
LVOsg36Q	-	36	sol-gel	quartz
ZLVO100Q	100	100	sputtering	quartz
ZLVO130Q	100	130	sputtering	quartz

Table 2.4 Labels and characteristics of the $LaVO_3$ samples [88].

The labels are indicative of the layer details: the numbers represent the thickness of the layers, the last letter stands for the substrate initial, "sg" means sol-gel (for the others, sputtering has been always omitted) and the initial "Z" indicates the structure ZnO//$LaVO_3$//quartz; ZnO does not completely cover the $LaVO_3$ layer, since it is deposited only on one side of the sample, as shown in Figure 2.5.

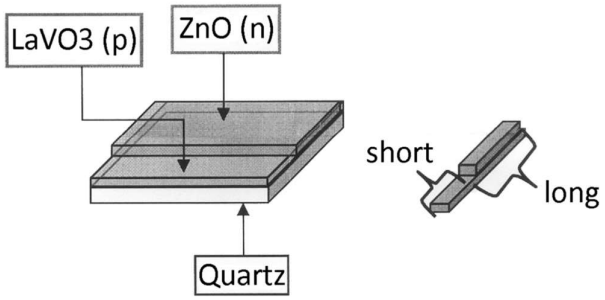

Figure 2.5 $LaVO_3$/ZnO samples structure [88].

In Table 2.5, some properties of the thin films deposited by sol-gel (LVOsg36Q) and sputtering (LVO55Q) on quartz are listed.

Sample	LVOsg36Q	LVO55Q
Composition	$LaVO_3$	$La_1V_{1.4}O_{3.6}$
Optical bandgap (eV)	1.2	4.1 direct /1.5 indirect
Carrier density (cm^{-3})	n $1.2 \cdot 10^{21}$	n$1.6 \cdot 10^{18}$ p $2.0 \cdot 10^{18}$
Mobility ($cm^2 \cdot V^{-1} \cdot s^{-1}$)	n 0.3	n 3.2 p 1.2
Resistivity ($\Omega \cdot cm$)	$2.5 \cdot 10^{-2}$	2.4

Table 2.5 Properties of the $LaVO_3$ samples deposited on quartz by sol-gel and sputtering. Adapted from [50].

From Table 2.5, it is evident for the sol-gel-deposited layer that the carrier density is quite high (in the range of 10^{21} cm^{-3}) to be used in a single gap absorber for solar cells, because of high Auger recombination [50]. A partial substitution of La with Ba was then performed to avoid the problem, but these new layers showed no reduction of the carrier density [50]. Still from Table 2.5, it is visible that the sputtered film is not fully stoichiometric; indeed, various sputtering powers were employed (sample LVO55Q was sputtered at 130 W) but the oxidation of the La target even in a sealed atmosphere did not allow a fully stoichiometric $LaVO_3$ deposition [50].
After preliminary simulations with AFORS-Het simulation software to estimate the minimum thickness of $LaVO_3$ necessary to build a solar cell with measurable photocurrent (details shown in [50]), two solar cell structures were fabricated: $LaVO_3$ on n-type c-Si and $LaVO_3$ on quartz. The I-V characteristics obtained under AM1.5[3] illumination are shown in Figure 2.6a,b [50,89].

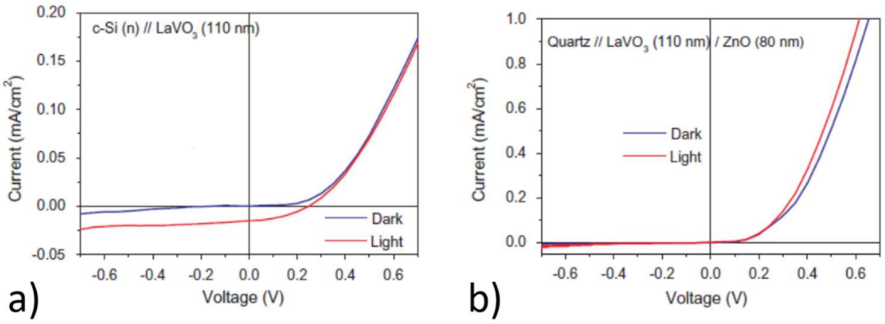

Figure 2.6 I-V characteristics of solar cell architectures under AM1.5 illumination using $LaVO_3$ thin films deposited by sputtering on a) c-Si and b) ZnO. From [50].

It is visible that in the structure with silicon very low I_{sc} occurs (see Section 1.5 for its definition), whereas in the second structure no photocurrent at all is observed. To understand why the $LaVO_3$/ZnO junction is not working properly, n-type ZnO layers where deposited at low temperature on two different $LaVO_3$ sputtered samples (ZLVO100Q and ZLVO130Q, respectively) in the configuration reported in Figure 2.5. These structures have been

[3] Both absorption and scattering depend strongly on the path length of sunlight through the atmosphere, *i.e.* on the Sun's elevation angle above the horizon. If the Sun is at an angle z from the zenith (or an angle h from the horizon) the air mass (AM) is defined as: $AM = \frac{1}{\cos z} = \frac{1}{\sin h}$. An AM1.5 corresponds to a 41.81° angle [89].

investigated by KPFM. Moreover, the whole range of samples reported in Table 2.4 has been analysed in the morphological properties by AFM.

2.4 $In_xGa_{1-x}N$ thin films

Two different sets of $In_xGa_{1-x}N$/GaN structures have been investigated, one Si-doped and the other undoped. All the layers have been grown at AIXTRON by Metal Organic Chemical Vapour Deposition (MOCVD) on sapphire and have a structure which is represented in Figure 2.7.

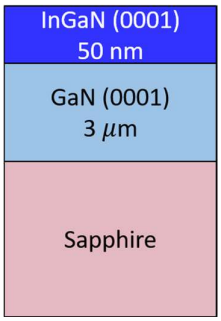

Figure 2.7 Sketch of the $In_xGa_{1-x}N$/GaN samples grown on sapphire substrate.

The Si doped samples names and characteristics are listed in Table 2.6, while the deposition details are reported elsewhere [90].

Sample	In by XRD[4] (%)	Carrier density by ECV[5] ($\times 10^{18}$ cm^{-3})	Si doping (Low, Medium, High)
L612	14.0	7	L Si
L613	19.0	10	L Si
L614	22.0	40	M Si
L615	19.3	90	H Si
L616	19.3	90	H Si

Table 2.6 Silicon doped $In_xGa_{1-x}N$/GaN samples labels, composition and carrier densities.

[4] XRD stands for X-ray powder diffraction. The analysis of the diffraction pattern allows for the identification of phases within a given sample. With that achieved, quantifying each phase present may be possible, followed by studying the crystallinity of a sample, the crystal structures and their lattice parameters, crystallite size and strain [221].

[5] ECV stands for electrochemical capacitance-voltage technique. It is a profiling technique, employed to measure the active carrier concentration profiles in semi-conductor layers through the creation of a Schottky junction [222].

One can notice that in the InGaN top layers In percentage varies from sample to sample, ranging from 14% to 22%. As already said in Section 1.4, In content influences the value of the band gap, ranging for these samples from 2.6 eV to 2.9 eV from higher to lower indium contents (blue light), whereas the GaN layer has a 3.4 eV band gap (UV light). Moreover, also the Si doping is different in all the layers and the numbering of the samples follows the increasing carrier density within the layers. Figure 2.8a,b,c shows some morphology AFM maps for different indium contents.

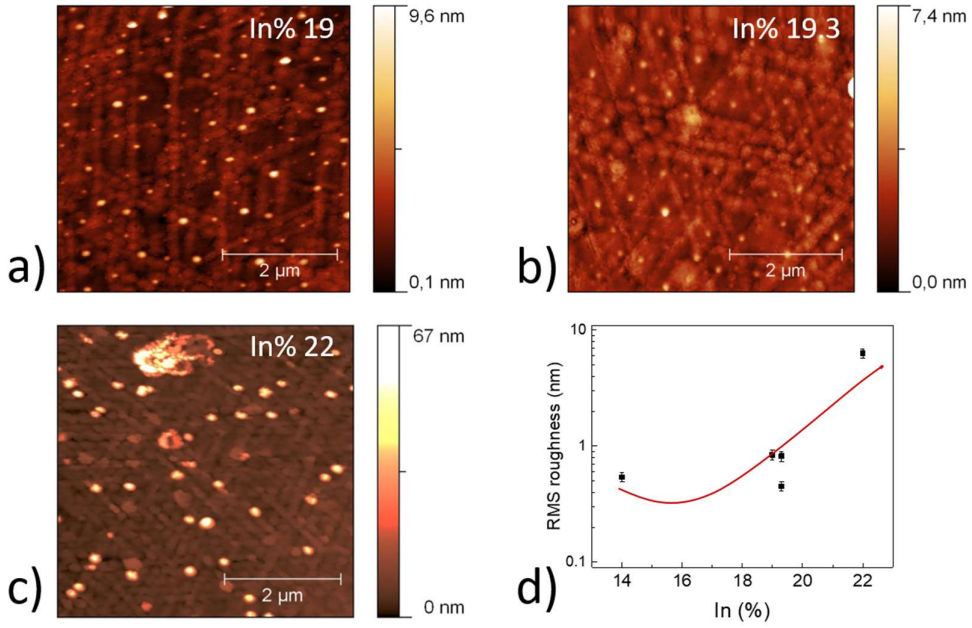

Figure 2.8 Morphology maps of Si doped InGaN/GaN samples with a) 19%, b) 19.3% and c) 22% indium content. d) The extracted roughness for samples is listed in Table 2.6. The red line is a guide for the eye. A. Minj, private communication.

In all the maps, crossing line structures are clearly visible and they are related to the presence of misfit dislocations creating a cross-hatch pattern parallel to the surface. The dislocation pattern has been confirmed also by transmission electron microscopy (TEM) images. The contrast for the cross-hatch pattern is mainly due to preferential growth along the dislocation line, which could indicate alteration in growth dynamics (A. Minj, private communication). The surface roughness of all samples listed in Table 2.6 has been extracted (similarly to the method described in Section 4.3) and plotted as a function of indium content in Figure 2.8d. As the red line clarifies, the roughness

increases with the indium content, meaning that the underlying cross-hatch pattern is denser with higher structures. All these layers have been investigated by surface photovoltage spectroscopy (SPS) and the experimental details have been listed in Section 4.1.2.

The undoped $In_xGa_{1-x}N$ layers characteristics are listed in Table 2.7 and the deposition conditions are similar to those reported in [91].

Sample	In (%)	Misfit Dislocations (MDs)
L605	15.6	No
L571	18.0	Yes

Table 2.7 Undoped $In_xGa_{1-x}N$/GaN samples labels, composition and misfit dislocations presence.

The two samples have the same thickness. However, as the critical thickness depends on the indium content and is below 50 nm for In>17% (see Figure 1.11b), the sample with the lowest indium content does not exhibit misfit dislocations, while they are present in the other sample. The sample with no dislocations exhibits a strained pseudomorphic structure, while the other presents a fully relaxed structure with defects (see Figure 1.11a). The band diagram in both cases is reported in Figure 2.9 .

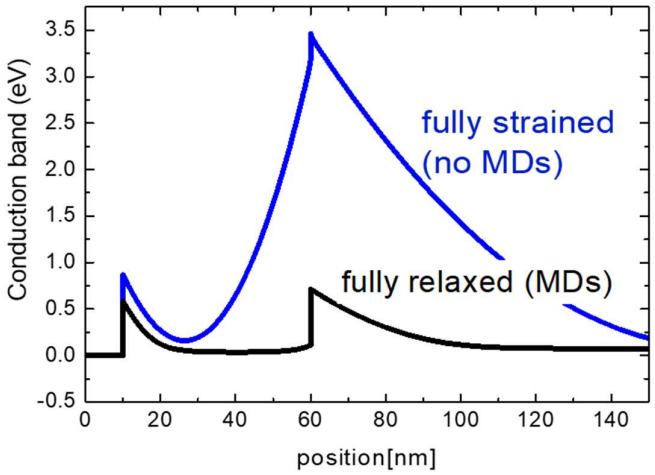

Figure 2.9 Band diagrams of fully relaxed with MDs (black solid line) and fully strained without MDs (blue solid line) undoped InGaN/GaN structures. InGaN and GaN offsets are given here [92]. The surface states are kept constant to 10^{13} cm^{-2}. A. Minj, private communication.

It is clearly visible that the band bending at the InGaN/GaN interface strongly diminishes as MDs appear. InGaN and GaN offsets are given here [92]. In sample L571, we have misfit dislocations at the interface. This sample has been investigated by KPFM technique (see Section 3.3 for more details). Figure 2.10a,b,c shows the topography, the KPFM in dark and the KPFM under illumination maps of sample L571, respectively. Like the Si doped samples, misfit dislocations are visible in the morphology map as a cross-hatch pattern. In this case, both the free surface and the dislocation areas are active under illumination and there is an evident contrast between the two areas both in dark and under illumination. The illumination induced changes in contact potential difference (CPD) values of both areas are more clearly explained in Figure 2.10d, where the number of counts for different CPD values is reported in both in dark (blue curve) and under illumination (red curve) cases. The concept of CPD will be deeply explained in Section 3.3. Each curve exhibits two peaks: the lower CPD peak is connected to the free surface CPD values' mode, while the higher CPD peak corresponds to the MDs CPD values' mode. From the comparison of the distribution of the CPD of measurements in dark condition and under illumination, both peaks undergo a shift towards higher values when they are under illumination. However, CPD increases by 430 mV at free surface and only by 314 mV at MDs. Here, the smaller change in CPD on MDs could be caused by two different factors: they act as strong recombination centres and/or the band bending on the surface above the MDs is smaller due to interface piezoelectric charge reduction at MDs, which is eventually seen in the surface band bending due to charge neutrality condition (see Equation (3.9)). Looking again at Figure 2.9 band diagrams, the surface barrier height and the band bending are quite different considering MDs free areas and MDs areas. However, it should be noticed that no contrast appears in KPFM maps in dark in the Si-doped samples, as shown in Figure 2.11a,b. A cross-hatch pattern in the morphology map is present, similar to the undoped L571 InGaN layer, due to the formation of misfit dislocations at the interface. Nonetheless, contrary to undoped InGaN layers, MDs do not create any contrast in the KPFM map. This effect is reasonable, since the high doping density of 10^{19} cm^{-3} screens the potential change near the misfit dislocations which is not visible anymore. The black spot in Figure 2.11b is related to another type of defect present in the Si doped layers, namely V-defect that is formed by a threading dislocation starting from the sapphire layer terminated by a pit in the shape of an inverted hexagonal pyramid [93]. The sample

set listed in Table 2.7 has been investigated as well by SPS and the experimental details have been listed in Section 4.1.2.

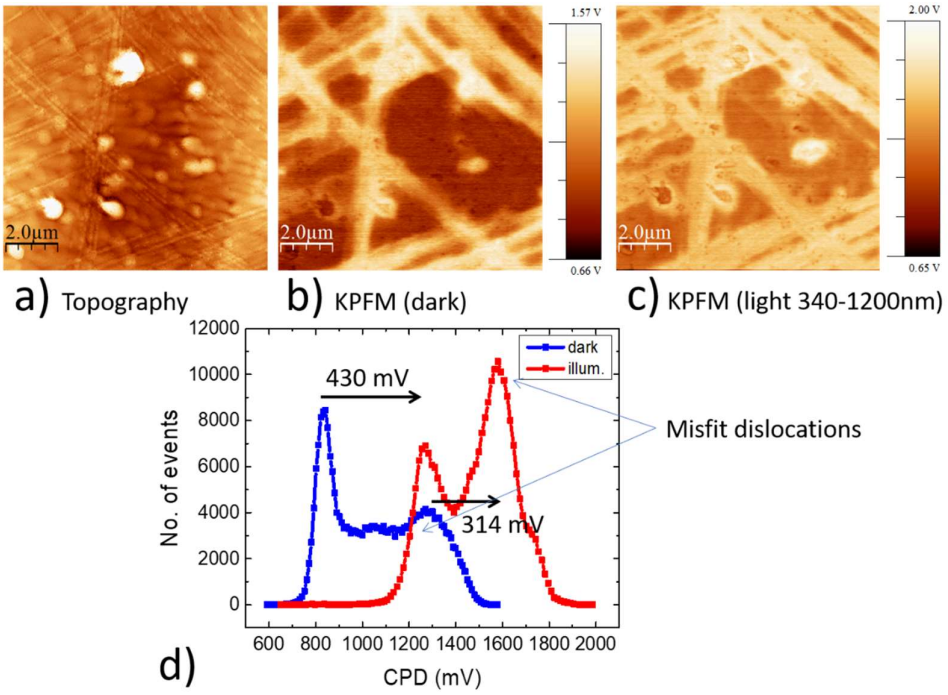

Figure 2.10 a) AFM topography, b) KPFM in dark and c) KPFM under illumination maps on sample L571. The darker areas are related to the free surfaces, while the lighter ones are related to dislocations. d) Number of counts of different CPD values in dark (blue squares) and under illumination (red squares) maps. Each curve shows two peaks: lower CPDs correspond to the free surface counts, higher CPDs to the misfit dislocation ones. The shifts of both peaks from dark to illumination are highlighted by two arrows. A. Minj, private communication.

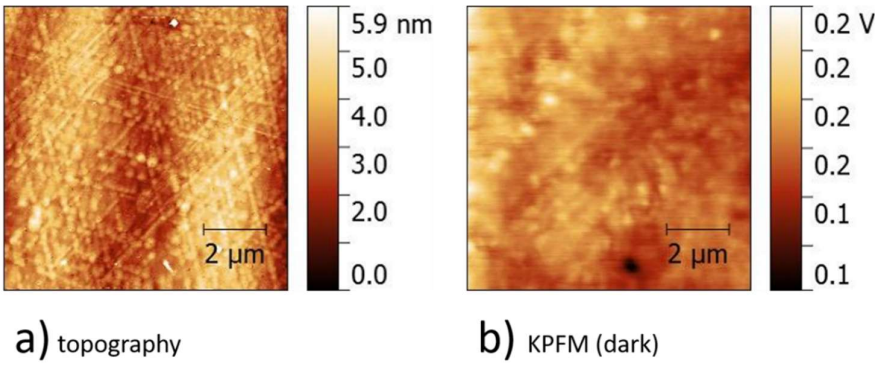

Figure 2.11 a) AFM topography and b) KPFM in dark maps on sample L613. A. Minj, private communication.

2.5 $Al_xIn_yGa_{1-x-y}N$ thin films

AlInGaN on GaN layers have been grown by MOCVD at AIXTRON and their structure is sketched in Figure 2.12. The growth conditions are reported elsewhere [94]. All the AlInGaN layers have such elements content that their energy band gap results higher than GaN's (3.4 eV). Both elements percentages and thickness have been varied in the sample set. These changes make the lattice parameter either bigger or lower than GaN's (see Figure 1.10), so the top layer is affected by compressive strain or tensile strain.

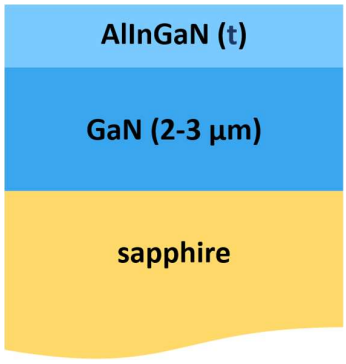

Figure 2.12 Sketch of the $Al_xIn_yGa_{1-x-y}N$/GaN samples grown on sapphire substrate.

The strain has been measured starting from the In, Al and Ga percentages acquired by XRD (see Note 4 at the bottom of page 37); the lattice parameter has been extracted using an Equation similar to (1.2) and then compared to the GaN lattice parameter. Following this difference, we could separate the samples into two sets: one affected by tensile strain and one by compressive strain and they are both listed in Table 2.8. However, apart from the strain, the presence of pinholes at the surface can be related to the thickness of AlInGaN layers. Indeed, in Figure 2.13 and in Figure 2.14, AFM maps of tensile strained samples set and the compressive strained samples set are shown, respectively. From left to right, the thickness in both sets increases. Firstly, it can be noticed that the roughness increases as well from left to right. Moreover, for thicker layers black dips occur on the surface, namely pinholes, meaning that there is a strain relaxation within the AlInGaN layer. These layers have been then investigated by SPS technique and all the experimental details are reported in Section 4.1.2.

Tensile strained samples				
At%	TS655 (5 nm//n.a.)	TS654 (20 nm//15.35%)	TS653 (50 nm//15.2%)	TS652 (96 nm//15%)
In	In progress	15	12	17
Ga		11	9	11
Al		73	79	72

Compressive strained samples			
At%	TS571 (7.8 nm//21%)	TS572 (23 nm//21.14%)	TS573 (54.1 nm//21.75%)
In	In progress	22	19
Ga		22	19
Al		56	62

Table 2.8 $Al_xIn_yGa_{1-x-y}N$/GaN samples labels, composition and strain.

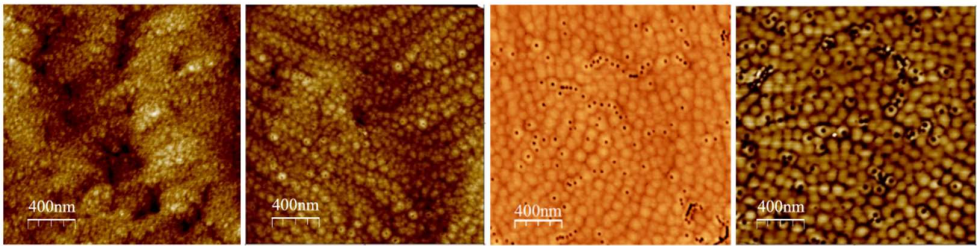

Figure 2.13 AFM maps of samples TS655, TS654, TS653, and TS652 from left to right (thickness increasing, tensile strained samples). The dark dots on the right represent pinholes at the surface. A. Minj, private communication.

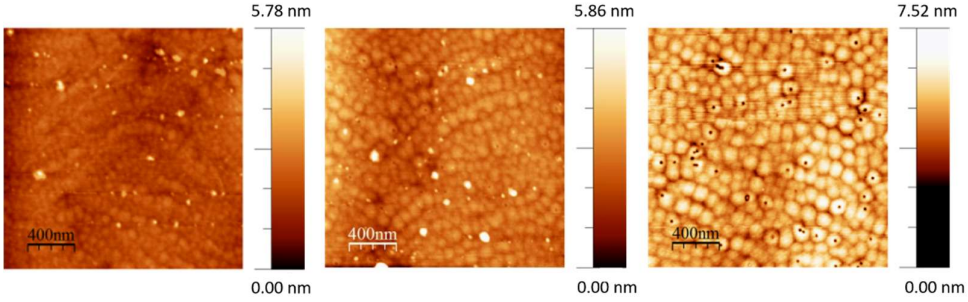

Figure 2.14 AFM maps of samples TS571, TS572, and TS573 from left to right (thickness increasing, compressive strained samples). The dark dots on the right represent pinholes at the surface. A. Minj, private communication.

3 Methods

In this chapter, all the techniques employed for the analyses of all samples are described in detail in their history, theory and applications. We will start with atomic force microscopy and its variants, *i.e.* conductive atomic force and Kelvin probe force microscopies. Then, a less standard technique called surface photovoltage will be introduced in all its potential. At last other more common additional techniques have been theoretically described.

3.1 Atomic force microscopy (AFM)

Scanning probe microscopes (SPMs) are instruments employed for the study of surfaces at the nanoscale level. SPMs collect images of surfaces using a physical nanometric probe that touches the surface of a sample both to scan the surface and to collect data [95]. Typically, a two-dimensional grid of data points is obtained and displayed as a computer image. The first SPM was the scanning tunnelling microscope (STM) developed at the IBM Research Lab in Zürich by Gerd Binnig and Heinrich Rohrer in 1982 [96]. This system allowed for the first time real space imaging of the atomic structure [97]. STM maintains a small gap of few angstroms between tip and sample, controlled by the tunnel current flowing between them [96]. As one electrode is shaped into a tip, current flows only from a specific orbital of the apex atom, thus achieving a lateral resolution of atomic dimensions [95,96].
Despite STM sub-angstrom resolution in all three dimensions, this setup employs an electrical current flow, restricting the investigation on conductive and semi-conductive materials only, with vacuum as an essential environment [95,98]. As a consequence, in 1985 G. Binnig and C. F. Quate introduced a new type of probe, based on atomic interactions between the tip and the sample, which they called atomic force microscope (AFM) [99]. AFM can equally work in air or in liquid ambient and provides three-dimensional surface topography at nanometre lateral and sub-angstrom vertical resolutions on both insulators and conductors [98].
In an AFM setup the probe is a tip at the end of a micro-fabricated cantilever with a low spring constant to measure in each point the tip-sample forces as the tip presses (either continuously or intermittently) against the sample surface.
The forces acting between the tip and the sample are van der Waals forces between two atoms at a distance r, described by the Lennard-Jones potential (whose qualitative shape and components are shown in Figure 3.1):

$$V(r) = 4\varepsilon \left[\left(\frac{\sigma}{r}\right)^{12} - \left(\frac{\sigma}{r}\right)^{6} \right] \tag{3.1}$$

where ε is the depth of the potential well, and σ is the diameter of the atom as described in a rigid sphere model. The first term relates to the attractive force at a large distance, while the second describes the short range repulsion [100].

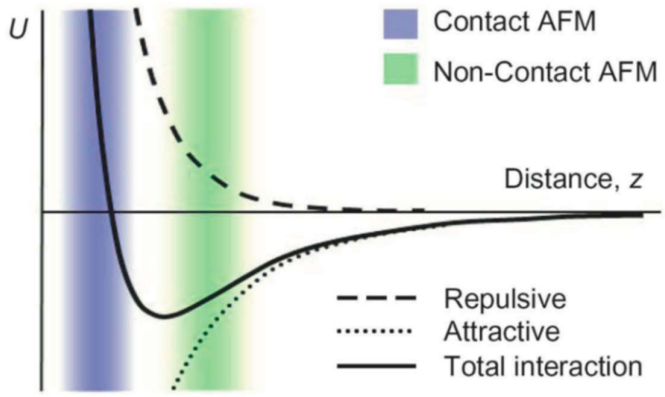

Figure 3.1 Interatomic force modelled as Lennard-Jones potential (solid black curve), with highlighted repulsive and attractive components. Different AFM operation modes regions are shown related to tip-sample distance [88].

These tip-sample forces cause the bending or deflection of the cantilever as the tip is scanned over the sample. The deflection is monitored through the deviation of a collimated beam from a diode-laser focused on the cantilever and then reflected towards the centre of a four-section split photodiode (Figure 3.2) [100]. In this way, the system can detect and distinguish two different forces: the cantilever bending due to attractive or repulsive forces and the cantilever torsion due to lateral components [100]. Then, the deflection is measured and recorded, to generate a map of surface topography [95].
In this work, AFM setup in non-contact mode has been employed. In this operating mode, the cantilever oscillates at a set frequency close or equal to its resonance one. The interactive forces between the tip and the sample are only attractive (see the green region in Figure 3.1) and modify the cantilever resonant frequency, so that the amplitude of vibration decreases for a fixed drive frequency [101].

By non-contact AFM technique, we have investigated the morphology at the nanoscale of $LaVO_3$ thin films fabricated with different deposition conditions. This method has allowed us to correlate the surface structure to the deposition technique, substrate and thickness.

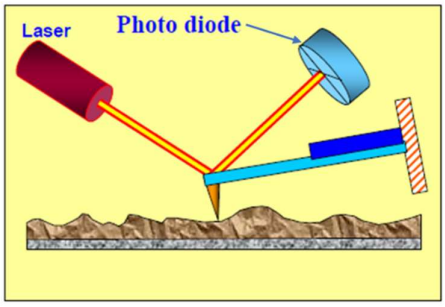

Figure 3.2 Schematic view of the optical system in an AFM. Adapted from [100].

3.2 Conductive atomic force microscopy (c-AFM)

By AFM it is also possible to investigate on characteristics of the sample beyond topography. Conductive atomic force microscopy (c-AFM) is a mode of atomic force microscopy in which a conductive tip is scanned in contact with the sample surface, while a voltage is applied between the tip and the sample, generating a current image [102]. At the same time, a topographic image is also generated. A typical c-AFM setup is illustrated in Figure 3.3a, in which a bias voltage is applied to the tip, while the sample is grounded (the bias could also be applied to the sample) [79].
The simultaneous acquisition of the current and the topographic images of the same area of the sample allows for the identification of features on the surface more or less conducting [102]. A scheme of the mode of operation of a c-AFM system is shown in Figure 3.3b. This double acquisition also allows to control and exclude possible topography-related artefacts [79]. Indeed, a local current increase can be associated to a wider contact area. As an example, this phenomenon generally occurs when the tip enters a dip while scanning. If no correlation results between height and current profiles, one can exclude this type of artefact [79].
From these c-AFM acquisitions, the local spreading resistance of the sample at the nanoscale can be evaluated [103,104]. Indeed, considering the tip-surface contact resistance constant during the scanning, the measured current for a given bias is proportional to the local resistivity of the sample [103,104].

Spreading resistance imaging can be also applied to samples with complex structures, where a study of the privileged current paths and changes in electrical resistance due to differences of composition is quite appealing [103,104]. After the current-map recording, current-voltage (I-V) characteristics can be acquired in specific points on the sample; the system linearly varies the bias applied to the tip (or to the sample) and the produced current is consequently extracted, amplified and recorded. In this way, the electrical behaviour in single different points of the maps can be investigated. During I-V measurements, it is advisable to employ minimum voltages sufficient to generate detectable currents [105]. With this choice, degeneration or, worse, breakage of the tip, as well as spikes of high current can be avoided.

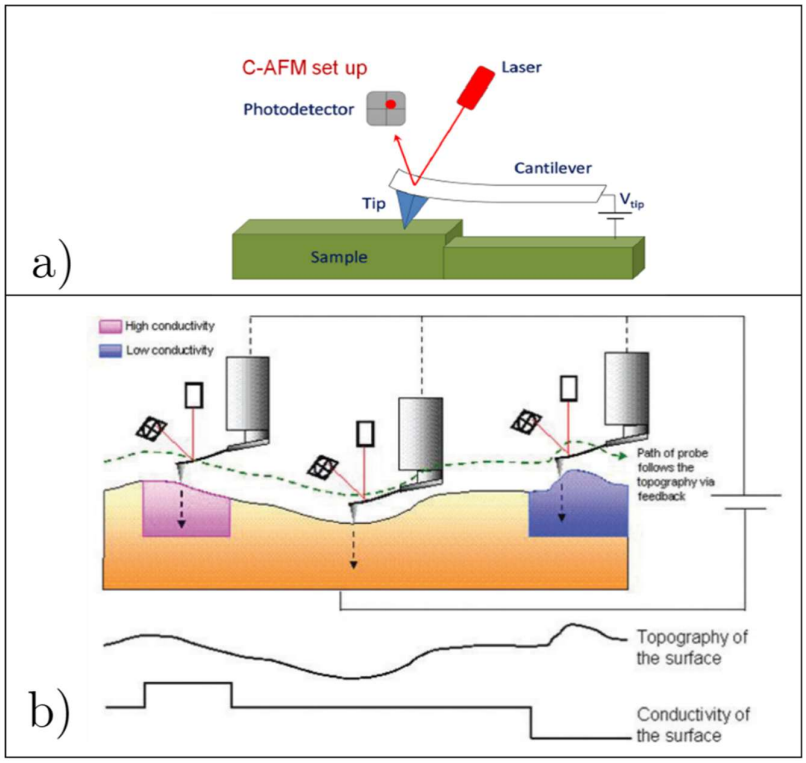

Figure 3.3 a) Schematic view (not in scale) of a c-AFM setup [79]. b) Schematic diagram of mode of operation of conductive AFM system [106].

In the last years, c-AFM technique has been used for different aims. To cite some examples, for the analyses of the resistive switching behaviour in memory systems [107–111], for the changes in the electrical properties for different deposition parameters [112,113], and for the investigation of local differences in the conductivity at the nanoscale [114,115]. In particular, this

technique is also useful for the investigation of local electrical properties or degradation/defect sites in different layers, as they affect the device performance [116–118]. Moreover, with c-AFM technique electrical properties of individual nanostructures can be investigated [119–122]; indeed, the tip works as a metalized probe, having intrinsically the function of an electrical contact. The possibility of additional extraction of local current-voltage characteristics allows for the evaluation of an electrical conduction transport model at the nanoscale [121,123,124].
c-AFM is efficient also for more exotic and newer purposes, where the tip plays an active role, rather than exclusively being a probe. For example, single gold filaments can grow at the tip apex and the local phase can be switched at nanometric scale in phase-change materials for nano-display application, by applying a tip-sample voltage bias in peculiar ambient conditions [125,126]. In this study, c-AFM is a valid technique to investigate the local electrical properties at the nanoscale, as well as the electrical transport model in nc-SiO_xN_y thin films, where deposition parameters have been changed.

3.3 Kelvin probe force microscopy (KPFM)

In topographic imaging, the main forces on the AFM tip are the van der Waals interactions between the tip and the sample (see Section 3.1 for more details) [127]. The most used operative mode for topography is the non-contact mode, where the cantilever is forced oscillating at its resonant frequency or close to it [101].
The motivation which led to the development of electrical force microscopy (EFM) and various related techniques was the possibility of exploiting an AFM tip to measure other local forces. Initially, scientists investigated magnetic forces, employing an iron cantilever briefly magnetized by exposure to a strong magnetic field [127,128]. The advances obtained in magnetic imaging inspired the development of the so-called localized charge force microscopy [129], based on the following principle: if a local charge is present at the surface, the Coulomb interaction between the charge and its image charge induced on the tip will influence the force gradient experienced by the cantilever [127]. EFM maps electric properties on a sample surface by measuring the electrostatic force between the surface and the biased tip. However, van der Waals forces are also always present and change according to the tip-sample distance. Topographic and EFM imaging can be acquired together if the two signals are successfully separated. Two different modes of acquisition can be performed [127,130].

The first mode is the Force Range technique, which relies on the differences in the dominant regimes of the van der Waals and electrostatic forces. The first are inversely proportional to r^6, while the latter to r^2, where r is the tip-sample distance. Thus, van der Waals forces are dominant for short distances, while they rapidly decrease as the tip is moved away, where electrostatic forces become dominant. In the Force Range technique, the first scan is performed near the sample (van der Waals forces regime); then, the EFM image is acquired at an increased tip-sample distance (electrostatic forces regime), which is schematically shown in Figure 3.4a [130].
The second mode is the Two Pass technique, which relies on following the topography line as the line of constant tip-sample distance, where the van der Waals forces are constant as well. In this technique, the first scan is performed to obtain the topography by scanning the tip near the surface; in the second scan, the tip-sample distance is increased to place the tip in the region where electrostatic forces are dominant. The tip is then biased and scanned without feedback parallel to the topography line obtained from the first scan, maintaining the tip-sample distance constant [127,130]. This method is shown in Figure 3.4b.

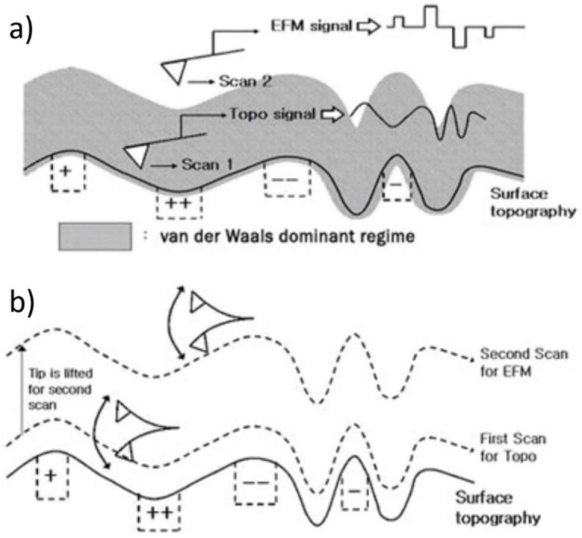

Figure 3.4 The schematics of a) Force Range technique and b) Two Pass technique for EFM acquisitions [130].

Kelvin probe force microscopy (KPFM) derives from the EFM technique. It was introduced as a tool to measure the local contact potential difference (CPD) between a conducting AFM tip and a sample, to map the work function or surface potential of the sample with high spatial resolution [131]. It

was first developed in 1991 by Nonnenmacher et al. [132] and Weaver et al. [133] and its name originates from the macroscopic method developed by Lord Kelvin in 1898 on metallic plates [97,131].
The KPFM measures the CPD between a conducting AFM tip and a sample, defined as [131]:

$$V_{CPD} = \frac{\phi_{tip} - \phi_{sample}}{-e} \tag{3.2}$$

where ϕ_{sample} and ϕ_{tip} are the work functions of the sample and tip, and e is the electronic charge. Generally, the tip and the sample surface have different Fermi energy levels; therefore, an electrical force is generated when the tip is brought close to the surface. Figure 3.5a represents the energy levels when the tip and the sample are at a distance d and not electrically connected (vacuum levels aligned but different Fermi levels) [131]. If the tip is close enough to the sample surface for electron tunnelling, the steady-state equilibrium requires Fermi levels to line-up and a current will flow (Figure 3.5b) [131]. The tip and sample surface will be charged, an apparent V_{CPD} will form due to the differences in the vacuum energy levels, and thus an electrical force will act on the contact area. As shown in Figure 3.5c, this force can be nullified applying an external bias (V_{DC}) which has the same magnitude as V_{CPD} with opposite direction [131].

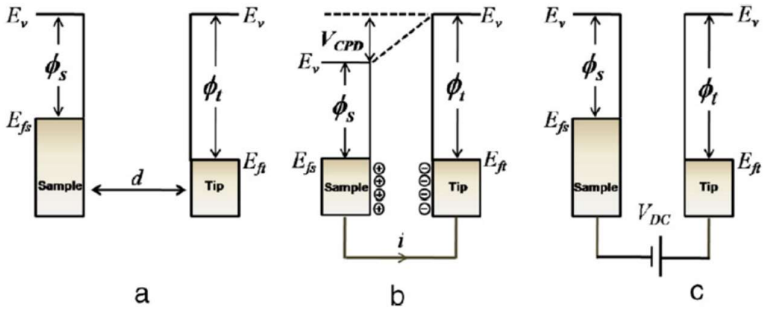

Figure 3.5 Electronic energy levels of the sample and AFM tip for: a) tip and sample separated by distance d with no electrical contact; b) tip and sample in electrical contact; c) external bias (V_{DC}) applied between tip and sample to nullify the tip–sample electrical force. E_V is the vacuum energy level; E_{Fs} and E_{Ft} are Fermi energy levels of the sample and tip, respectively. From [131].

The amount of applied external bias (V_{DC}) that nullifies the electrical force due to the V_{CPD} is equal to the work function difference between the tip and

sample; therefore, when one knows the tip work function, the work function of the sample can be calculated [131].
By applying to the AFM tip an AC voltage (V_{AC}) together with a DC voltage (V_{DC}), measuring the work function of the sample by KPFM becomes possible. V_{AC} generates oscillating electrical forces between the tip and the surface, and V_{DC} nullifies the oscillating electrical forces originated from CPD between tip and sample surface. The electrostatic force (F_{es}) between tip and sample is given by:

$$F_{es}(z) = -\frac{1}{2}\Delta V^2 \frac{dC(z)}{dz} \tag{3.3}$$

where z is the direction normal to the sample surface, ΔV is the potential difference between V_{CPD} and the voltage applied to the tip, and dC/dz is the gradient of the tip-sample capacitance [127]. When $V_{AC}\sin(\omega t) + V_{DC}$ is applied to the tip, ΔV will be:

$$\Delta V = V_{tip} \pm V_{CPD} = (V_{DC} \pm V_{CPD}) + V_{AC}\sin(\omega t) \tag{3.4}$$

Note that the $\pm$ sign depends whether V_{DC} is applied to the sample (+) or the tip (−) [131]. Substituting Equation (3.4) in Equation (3.3), one obtains the expression for the electrostatic force applied to the tip:

$$F_{es}(z,t) = -\frac{1}{2}\frac{\partial C(z)}{\partial z}[(V_{DC} \pm V_{CPD}) + V_{AC}\sin(\omega t)]^2 \tag{3.5}$$

This expression can be divided into three parts:

$$F_{DC} = -\frac{\partial C(z)}{\partial z}\left[\frac{1}{2}(V_{DC} \pm V_{CPD})^2\right] \tag{3.6}$$

$$F_{\omega} = -\frac{\partial C(z)}{\partial z}(V_{DC} \pm V_{CPD})V_{AC}\sin(\omega t) \tag{3.7}$$

$$F_{2\omega} = \frac{\partial C(z)}{\partial z}\frac{1}{4}{V_{AC}}^2[\cos(2\omega t) - 1] \tag{3.8}$$

F_{DC} results in a static deflection of the AFM tip; F_{ω} with frequency ω is used to measure the V_{CPD}, and $F_{2\omega}$ can be used for capacitance microscopy [131]. A lock-in amplifier is employed to measure the contact potential difference,

extracting F_ω, which is a function of V_{CPD} and V_{AC}. Since the output signal of the lock-in amplifier is directly proportional to $(V_{DC} - V_{CPD})$, the contact potential difference V_{CPD} value can be measured by applying a V_{DC} to the tip, such that the lock-in output signal is nullified and F_ω equals zero. Subsequently, V_{DC} is acquired for each point on the sample surface; it results in a map of the work function or surface potential of the whole sample surface area [131]. Since the KPFM acquisitions can be performed also in one-pass mode (see the aforementioned techniques for EFM), the frequency ω is chosen to be smaller than the cantilever oscillation frequency f, so that the two signals do not interfere with each other [130].
Invented in 1991, it took almost 10 years before there was a sizeable number of publications per year involving the KPFM technique. Nevertheless, starting with the new millennium, this technique found more and more applications and interest, visible in a considerably increased publication activity [97]. This trend went in conjunction with the more wide-spread availability of AFM equipment in many laboratories worldwide. In the recent years, the publication number is nearly 10 times as high as in the early years after its invention [97].
Recently, KPFM has been used to study charge effects [134,135], transport and dynamics [136–139] on very different structures, from nanostructures, 2D layers of organic, inorganic and mixed materials. Moreover, an investigation of the changes in work function [140] and polarization [141] under illumination have been performed on perovskites. At last, interface [142] and local properties [143] characterization, including strained areas [144] and grain boundaries [145], has been performed by KPFM. All these applications exhibit how versatile and useful this technique is in a wide range of fields.
By KPFM technique we could determine the barrier height value between the $LaVO_3$/ZnO interface, together with the work functions both the materials, individually. It is worth noting that $LaVO_3$ work function has been never reported in literature before [50,88].

3.4 Surface photovoltage (SPV)

SPV is a contactless and non-destructive technique that analyses the light-induced variations of the band-bending at different photon energies. For this reason, we also talk about surface photovoltage spectroscopy (SPS). This technique allows for a quantitative characterization of electronic properties of semiconductors, n-p type carriers, bandgap, minority carrier lifetime [146]. Studies of the effects of illumination on the surface voltage had begun in the late

1940s and early 1950s with the classical articles of Nobel prize laureates Brattain and Bardeen [147]. A major breakthrough in SPV technique took place in the early 1970s, when a systematic investigation research on the effects of sub-bandgap illumination on the surface voltage took place by Gatos et al. and the term SPS was coined [148]. Brillson used SPS extensively throughout the 1970s and 1980s to study a huge variety of semiconductor surfaces [149]. Later, during the 1990s, a renewed vigour in the development of SPV related techniques occurred. Indeed, Shapira's group and more recently Pollack's group have employed SPS to study heterostructures, interfaces and finite devices [146].
The SPV technique has several advantages: the measurements are ambient insensitive, they can be performed on either clean or real surfaces, at any reasonable temperature, reaching any lateral resolution, down to the atomic scale [150]. In SPV spectroscopy, electronic transitions are detected as changes in the slope of the SPV spectra, which correspond to band-to-band transitions or intra-band transitions at the surface or interface of a multi-layered structure [146,151,152]. One could say that SPS for the extraction of the energy bandgap is nothing more than an emulation of an absorption spectrum. However, as opposed to transmission spectroscopy, SPS does not require light collection and therefore it can be performed on arbitrarily thick samples without the need of a transparent substrate; in addition, in some ranges and configurations, SPS can even look at buried surfaces. Moreover, this method is insensitive to reflection and scattering of photons, which is an advantage for the investigation of nano- and micro-structures [150]. Indeed, for all these reasons, SPV can be applied on buried layers, deposited thin films, heterostructures, multi-phase materials and nanostructures, where standard transmission optical spectroscopies are not applicable [152]. Nowadays, the method is widely used to detect electronic transitions (band-to-band, defect-band, surface states-bands) in low dimensional semiconductor systems, thanks to the technique advantages [152].
For all these reasons, several information can be extracted by SPV on a-SiO_x and a-SiO_xN_y samples, such as optical bandgap, other transitions relative to different phases and minority carrier lifetimes.

3.4.1.SPV theoretical hints

To introduce the theory behind the SPV method, the electrical properties of a surface and the definition of surface potential are requested.

The bulk of an ideal (and infinite) crystalline semiconductor can be described as a periodic structure where electrons can be depicted as Bloch waves (periodic functions with the same periodicity of the crystal). However, a real semiconductor is not infinite and surfaces (with a gas) or interfaces (with a solid-state material) occur. A surface/interface is an abrupt termination of the periodic structure. The system at the surfaces tries to minimize its energy with different strategies: dangling bonds, adsorbed atoms, surface reconstruction, relaxation. All these defects (as compared to the ideal crystal) give rise to surface-localized electronic states within the semiconductor bandgap and/or a double layer of charge, known as a surface dipole [146,153].
Surface states on semiconductor surfaces possess either donor or acceptor character, thus they may be charged [154].
To rebuild charge neutrality at the surface, surface-localized states induce a charge transfer between the bulk and the surface, creating a surface charge region (SCR). According to the surface charge neutrality condition:

$$Q_{SS} + Q_{SC} = 0 \tag{3.9}$$

the SCR charge Q_{SC} exactly compensates the net surface charge Q_{SS} [153,154]. Therefore, a non-zero electric field is formed and the surface potential V_S differs from the potential in the bulk even under equilibrium conditions. The potential drop across the SCR appears as a bending of the semiconductor bands in the vicinity of the surface [150]. The surface potential can be defined by the following expression:

$$eV_S = E_V - E_{V_S} = E_C - E_{C_S} \tag{3.10}$$

where e is the elementary charge, E_V and E_C are respectively the energy positions of the valence and conduction bands in the bulk, whereas E_{V_S} and E_{C_S} indicate the position of the same bands at the semiconductor surface [154]. From Equation (3.10), it can be derived that a positive value of V_S corresponds to downward-bent bands, and a negative value of V_S to an upward band bending [146].
Generally, both n- and p-type semiconductors are in depletion conditions, in which the majority carrier concentration at the surface is smaller than its equilibrium value, but still larger than the minority carrier concentration at the surface. For this reason, n-type semiconductors exhibit an upward band bending, while p-type semiconductors a downward band bending, as shown in the light blue curves of Figure 3.6a.

The surface photovoltaic effect represents a specific variant of the photovoltaic effect. When no external field is present, the surface charge neutrality condition (Equation (3.9)) remains valid. However, both Q_{SS} and Q_{SC} may vary significantly under illumination [146]. Indeed, light absorption induces the generation of electron-hole pairs by means of both band-to-band transitions and trap-to-band transitions, depending on the photon energy [150].
The SPV is an illumination-induced change of the equilibrium surface potential V_S, followed by a charge transfer and/or redistribution within the layer [153]. The driving force for the transfer and separation of carriers is the built-in electric field generated by the SCR. The surface photovoltage is thus defined as:

$$SPV = V_S(light) - V_S(dark) \tag{3.11}$$

where $V_S(light)$ is the surface potential under illumination and $V_S(dark)$ is the surface potential in dark [153,155].
An SPV signal can be detected by illuminating the surface with above or below bandgap light; usually a tuneable source is employed to obtain a spectroscopy (SPS): a continuous spectrum of SPV versus the incident photon energy is extracted.
When photons at least equal the energy of the bandgap, electron-hole pairs are photogenerated and transferred in opposite directions helped by the built-in electric field towards the bulk or the surface. In this way, the surface potential becomes reduced. In a p-type semiconductor, the electric field drives the generated electrons towards the surface/interface and the holes towards the bulk. The reverse process occurs in an n-type semiconductor [153]. In this way, the band bending is decreased in both cases, as schematically shown in Figure 3.6a.
At the energy close to the bandgap, the SPV signal increases in module, becoming negative and positive for p-type and n-type semiconductors, respectively. Therefore, from the sign of SPV the type of the majority carriers can be extracted. The variation at the bandgap energy is the most significant feature in a spectrum [153].

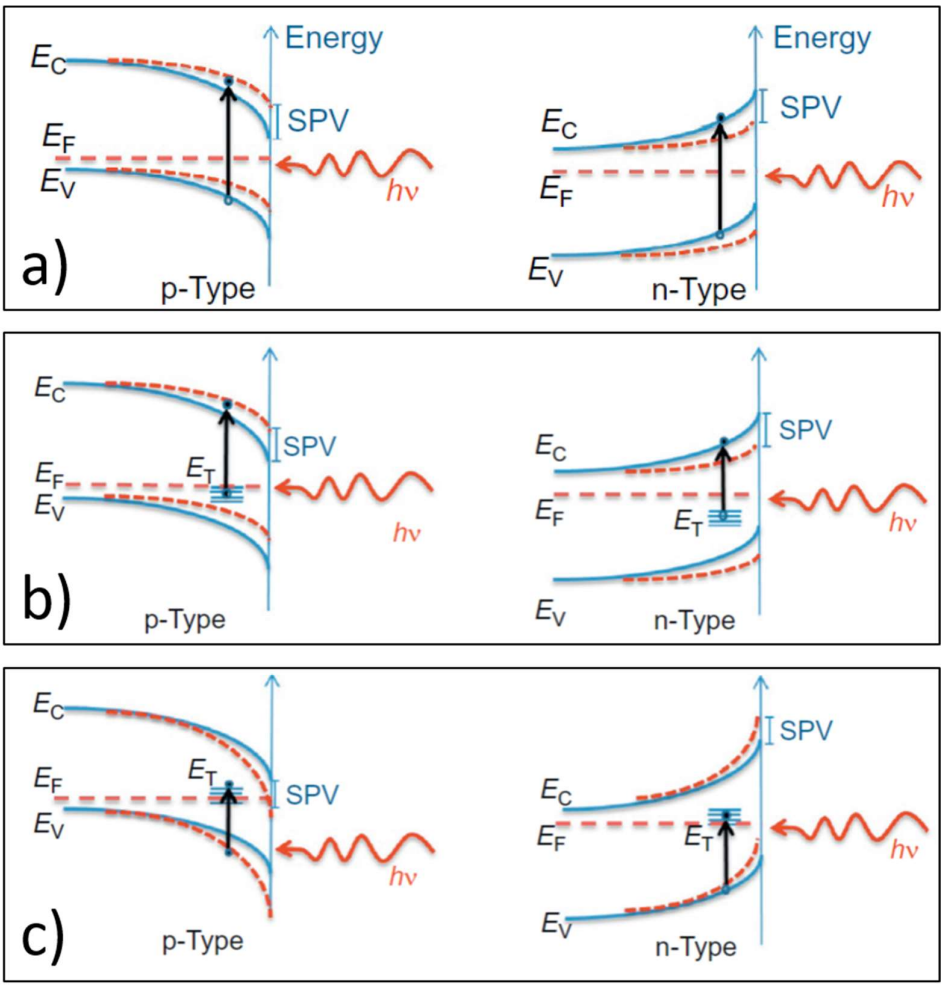

Figure 3.6 Band diagram of a p-type (left) and n-type (right) semiconductor close to the surface under equilibrium (solid light blue curves) and non-equilibrium (dashed red curves) for a) above bandgap illumination, b) below bandgap illumination with $h\upsilon = E_C - E_T$ and c) below bandgap illumination with $h\upsilon = E_T - E_V$ conditions. Band edges E_C and E_V, Fermi energy E_F, surface potential V_S, trap level E_T, and surface photovoltage SPV are indicated in the diagrams. Adapted from [153].

With the use of a sub-bandgap illumination, below bandgap transitions at defects or surface states can be revealed. Assuming that these states are associated to a deep trap level E_T, two different transitions are possible: from the trap state to the conduction band (Figure 3.6b, for p-type (left) and n-type (right)) or from the valence band to the trap state (Figure 3.6c). In the first case (Figure 3.6b), when an electron is promoted from the trapped state E_T to the conduction band E_C, the band bending would decrease in both p- and n-type semiconductors, achieving an increase of the SPV in module (as for

the band-to-band transition). In the second case (Figure 3.6c), the electronic transition from the valence band E_V to the trapped state E_T would increase the band bending, generating a positive SPV signal for the p-type and a negative one for the n-type semiconductors [153].
Optical absorption for photon energies below the optical gap may also occur as localized shallow states extend from the energy gap, the so-called Urbach tails [156,157]. The broadening of the onset of SPV spectra near the energy gap could then be an indicator of the presence of tail states in the bandgap of the investigated material [146].
In amorphous semiconductors this effect is enhanced, since the distribution of the electronic states of the conduction and valence bands do not abruptly terminate at the band edges. Indeed, huge disorder is present within the amorphous network [156,157]. The breadth of the tail states, and consequently the broadening of the measured SPV, reflects the amount of disorder within the amorphous material [146].

3.4.2. Nanostructures characterization

SPS has been used since the early seventies by Gatos and Lagowski (1973) [148] to characterize semiconductor surfaces (surface or flat band potential determination), oxides deposited on different surfaces (oxide thickness, integrity, charge, and plasma damage) and bulk properties (minority carrier lifetimes and diffusion lengths, doping densities measurements). In addition, starting from 1999 [146,150,153,158], the method has also been applied to the study of surface, interface and defect states in semiconductors.
Nowadays, surface photovoltage has also been used to investigate nanostructures and materials useful for different applications. For example: an efficient charge separation has been demonstrated in Ge nanocrystals by SPS for solar energy conversion and electronics applications [159]; local behaviour of the photogenerated carriers in silicon nanopillars has been investigated by SPV for hybrid organic-inorganic photovoltaic applications [160] and efficient charge transport in silicon photoanode for water oxidation has been demonstrated by SPV for water splitting devices [161]. Finally, SPS has always allowed for a clear understanding on the role of defects on optical properties; to cite an example, the role of yellow band on photoluminescence of AlGaN/GaN heterostructures has been clarified by SPS; these materials are innovative for different applications as high power/frequency high electron mobility transistor (HEMT), high efficiency light emitting diodes (LEDs), and solar/visible blind ultraviolet photodiodes [162].

The knowledge of band-to-band or defect-band electronic transitions in a certain material and/or nanostructure is fundamental to explore the capabilities of that system as complete device [152].
As an example, we report here some results on nc-Si:H thin films by SPV spectroscopy [152,163]. This investigation has allowed for the identification of electronic transitions at partially localized states of Si nanocrystals (NCs).
nc-Si:H is a multiphase material consisting of an amorphous Si matrix and dispersed Si NCs. This is a promising material to have distinguishing characteristics of higher carrier mobility, greater doping efficiency and efficient visible photoluminescence [164–166]. Generally, two paths can be followed to obtain a nanocrystalline phase within the amorphous network: a re-crystallization technique such as rapid thermal annealing, excimer laser, and aluminium-induced crystallization or several chemical vapour depositions (CVD) techniques including layer-by-layer deposition and magnetron sputtering [167]. The first way is mostly used for silicon-based tandem device solar cells applications, photovoltaic and optoelectronic devices, while the second (especially PECVD) is a standard industrial process in the solar cells and thin-film transistor (TFT) technology [167,168].
An SPV spectrum for a nc-Si:H sample deposited with low energy PECVD (LEPECVD) with high crystallinity (75%) and low hydrogen dilution (3%) is reported as an example in Figure 3.7a [152,163].
The knee that occurs in the spectrum at 1.59 eV corresponds to the energy gap (E_G) of the film, which is a typical value for highly crystalline films. The Si nanocrystals are small enough (5-15 nm) to induce the localization of free carriers giving rise to three different peaks in the spectrum. Then, in this region, the spectrum below bandgap could be fitted with the sum of three Lorentzian functions plus an exponential function whose factor determines the Urbach tails and thus the crystal disorder of the a-Si matrix (see Section 3.4.1). The Lorentzian peaks are linked to the transitions assisted by localized states, at 1.31, 1.41 and 1.51 eV, while Urbach tails in the present samples result of about 80 meV. Figure 3.7b shows a sketch of the proposed band diagram of the material. One could say that the analyses of spectra have allowed for the detection of electronic transitions between localized states, and so quantum confinement effects at Si NCs. However, SPV requires not only carrier generation but also carrier collection [152]. Therefore, one must conclude that free carriers at Si NCs are only partially localized, according to theoretical predictions from [169]. In conclusion, SPV spectroscopy has

allowed for the identification of electronic transitions at partially localized states at Si NCs in nc-Si:H thin films.

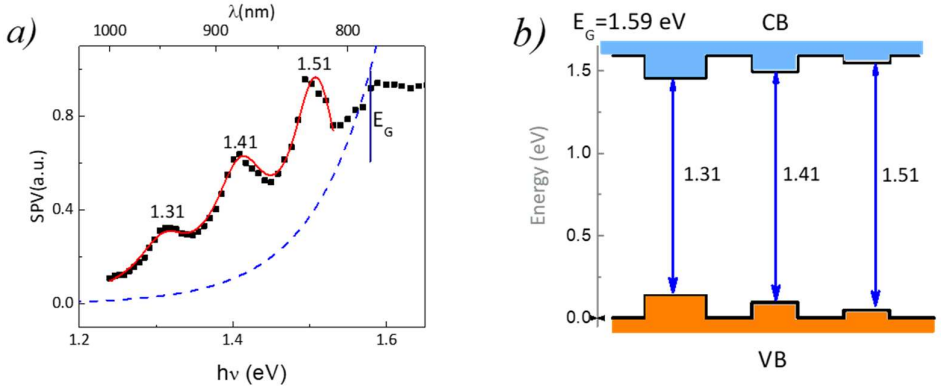

Figure 3.7 a) Experimental SPV spectrum (dark squares) of a highly crystalline (75%) grown at low hydrogen dilution (3%) nc-Si:H film. The fitting function is the sum of three Lorentz functions (centred at 1.31, 1.41 and 1.51 eV) (solid line) plus an Urbach tail contribution due to the amorphous matrix (dashed line). The Lorentzian peaks have been related to electronic transitions at partially localized states. b) Sketch of the band diagram resulting from the SPV spectrum of Figure 3.7a. Reprinted from [152,163].

3.4.3. Passivation quality

Additionally, information about the passivation quality of interfaces can be extracted from SPV spectra.

As an example, in Figure 3.8, SPV spectra in the range between 0.9 and 1.2 eV of nc-SiO_xN_y layers, respectively L3h and L0h samples (see Table 2.1) on c-Si are presented. The employed lamp is a quartz tungsten halogen (QTH) lamp (see Section 4.1.1.1 for details), with a black body emission spectrum with maximum emission around 1 eV [170]. The annealed sample (L3h) and the as-deposited sample (L0h) show spectra with different shape.

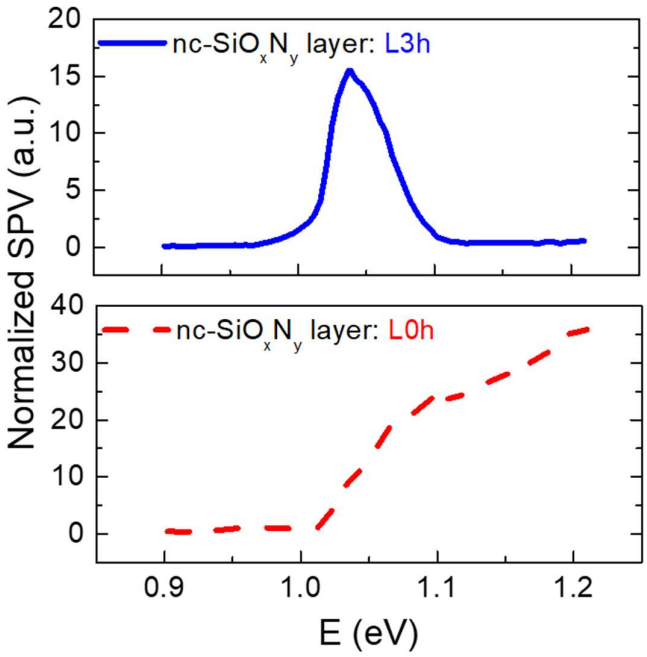

Figure 3.8 SPV spectra measured with a QTH lamp of nc-SiO_xN_y samples: L3h (annealed) in blue, solid line, and L0h (as-deposited) in red, dashed line. Both samples have identical deposition parameters, apart from the annealing step. The recombination is linked to a decrease of the signal at higher photon energies (solid blue curve), while good passivation leads still to a higher signal (dashed red curve). Information on the normalisation process is collected in Section 4.1.2.

In this spectral region, the top layers are transparent (their optical band gap is quite larger); for this reason, it is possible to investigate the interface with the c-Si substrate. Both spectra show an expected knee at around 1.05–1.1 eV, related to the band-to-band transition in the c-Si substrate. Above this photon energy a drop in the signal occurs for the annealed sample (L3h), whereas a further increase is present for the as-deposited sample (L0h).
It is already known that the inverse of the absorption coefficient, which equals the light penetration depth, generally decreases for above band gap energies; thus, in this spectral region the SPV signal is strongly affected by recombination phenomena at the interface [146]. Since the signal decreasing trend for L3h occurs in this specific spectral region, the drop can be related to a strong electron-hole recombination at the interface. This interpretation is in good agreement with the observation of oxygen precipitates formation at the

interface caused by the thermal treatment [19]. On the contrary, L0h demonstrates better interface characteristics and lower interface recombination, since the above bandgap region is not affected by carrier recombination.
Therefore, this experimental evidence clearly demonstrates the capability of SPV spectroscopy to reveal the passivation quality of an interface.
This process will be employed to collect information on the interface passivation quality between the layer and the substrate in our sub-stoichiometric a-SiO_x and a-SiO_xN_y thin films on Si.

3.4.4. Minority carrier lifetime

With the SPV technique it is also possible to extract information on the effective minority carrier lifetimes of materials. In detail, this method consists of monitoring the signal of several spectra at a fixed photon energy under variation of the chopper frequency (see SPV setup in Section 4.1.1.1). We will refer to this kind of SPV measurements as ac-SPV investigation.
The SPV signal is proportional to the number of photo-generated carriers at each chopper frequency; therefore, the lifetime related to a special feature of the spectrum could be extracted from an ac-SPV investigation. The word "feature" typically refers to a peak or a knee at the layer bandgap. The minority carrier lifetime can be estimated by fitting the frequency dependent amplitude of the feature at one photon energy with the following function [162,171,172]:

$$SPV = \frac{A\tau}{(1+\omega^2 \cdot \tau^2)^{1/2}} \tag{3.12}$$

where A is a proportionality constant, τ the effective minority carrier lifetime and ω the angular chopper frequency $\omega = 2\pi f$.
As an example, the spectra of L0h sample (nc-SiO_xN_y layer, see Table 2.1) at different chopper frequencies is shown in Figure 3.9a. The highest point after the transition has been selected as an interesting feature (indicated with an arrow). Then, the signal amplitude for each spectrum is extracted and plotted as a function of the chopper frequency, as reported in Figure 3.9b. This curve is successively fitted by Equation (3.12), red solid curve in Figure 3.9b, and

an estimate of the minority carrier lifetime can be carried out as a fitting parameter.

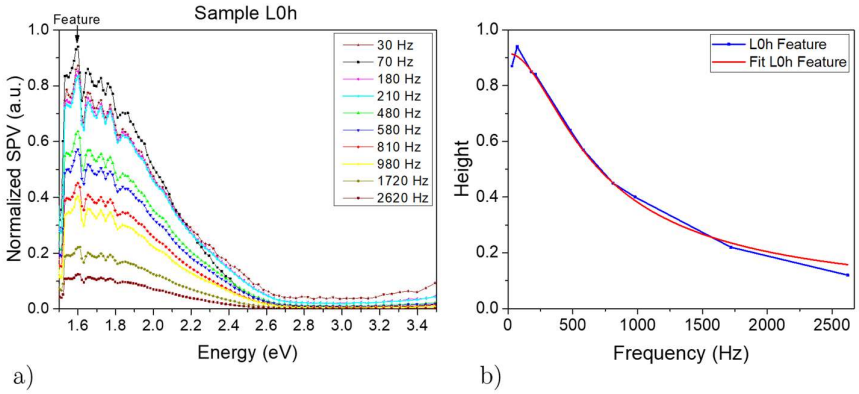

Figure 3.9 a) SPV spectra of L0h nc-SiO_xN_y sample at different chopper frequencies in different colours. A feature at around 1.6 eV is highlighted. b) The height of the highlighted feature as a function of the chopper frequency (blue solid line), with the corresponding fit by Equation (3.12) as a red solid line.

3.5 Additional techniques

Other more standard techniques have been employed in this study, such as spectral ellipsometry, Fourier transform infrared spectroscopy, and photoconductance decay. For this reason, they will be briefly described in the following Sections.

3.5.1. Spectral ellipsometry

Spectral ellipsometry measures the polarization variation of light after it is reflected or transmitted by a material structure. The polarization change is represented as an amplitude ratio, Ψ, and the phase difference, Δ. The measurement depends on both optical properties and thickness of individual materials. Indeed, ellipsometry is primarily used for film thickness and optical constants evaluation. However, it is also applied to characterize composition, crystallinity, roughness, doping concentration, and other material properties related to a change in optical response.

Since the 1960s, the interest in ellipsometry has steadily grown due to its sensitivity of nanometre scale in measuring thickness, a quite useful tool for the thin films employed in microelectronics. Today, the range of its applications has spread to the basic research in physical sciences, semiconductor and data storage solutions, flat panel display, communication, biosensor, and

optical coating industries [173]. The wide use is explained by two factors: many applications rely on thin film technology, and ellipsometry is flexible concerning the material type (dielectrics, semiconductors, metals, superconductors, organics, biological coatings, and composites of materials) [173].
Ellipsometry measurements mainly concern how p- and s-components of the light electric field change upon reflection or transmission in relation to each other, where p- and s- components are those parallel and perpendicular to the plane of incidence, respectively. A known polarization is reflected or transmitted from the sample and the output polarization is measured, with the change in polarization ρ commonly written as [173]:

$$\rho = \tan \Psi \, e^{i\Delta} \tag{3.13}$$

The primary tools for collecting ellipsometry data all include: light source, polarization generator, sample, polarization analyser, and detector. One common configuration includes a rotating analyser and it is sketched in Figure 3.10a [173]. It should be noticed that a sample is always deposited on a substrate. For each surface or interface present, the incident light is split each time into a reflected and a transmitted component, following the Fresnel rules. Eventually, while crossing a thickness of each absorbing material, the light intensity drops exponentially according to Beer's law. Indeed, a general situation is described in Figure 3.10b [173].
Briefly, a source of polarized light is then sent through a polarizer, so that its axis is oriented between the p- and s-planes. The linearly polarized light reflects from the sample surface, becomes elliptically polarized, and travels through a continuously rotating polarizer (referred to as the analyser). Afterwards, the detector converts light to an electronic signal to determine the reflected polarization; this information is compared to the known input polarization to determine the polarization change caused by the sample reflection (Ψ, Δ) [173]. The incident light passes through a spectrometer to make it monochromatic, so that a spectrum can be acquired.
After a sample is measured, a model is constructed to describe the sample to calculate the predicted response from Fresnel equations, which depends on

both thickness and optical constants of a material. The calculated values are then compared to the experimental data [173].

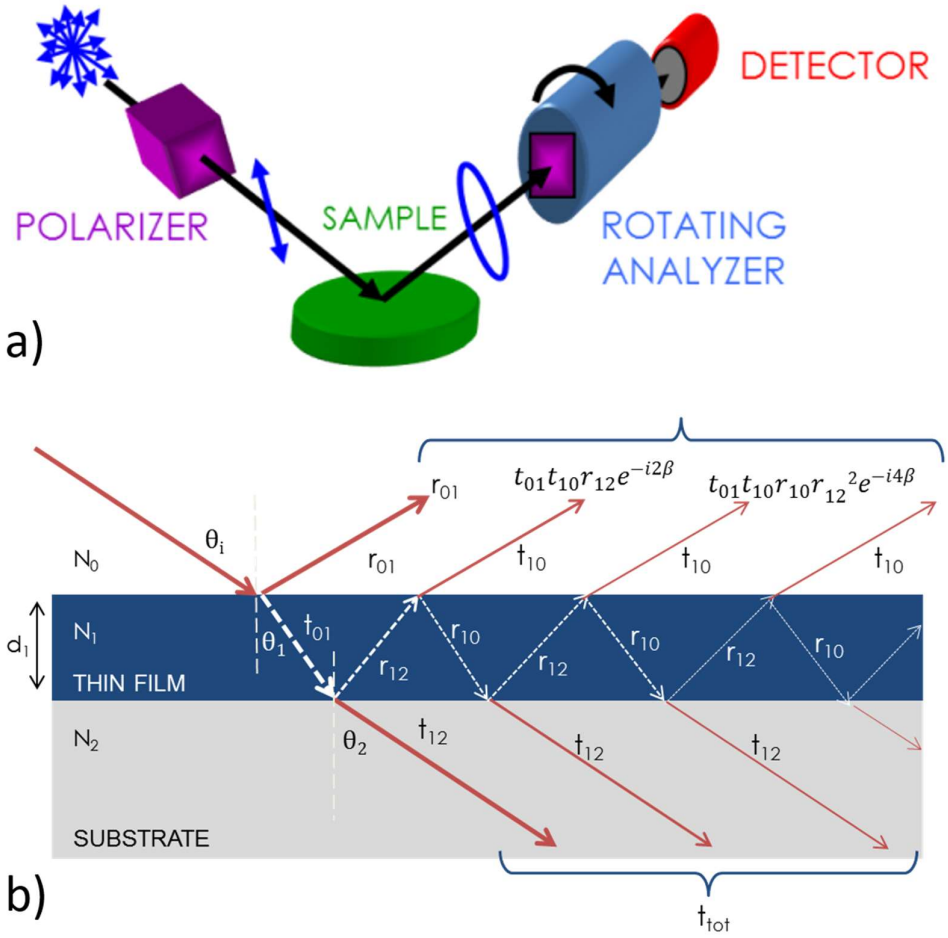

Figure 3.10 a) Sketch of an ellipsometry setup based on a rotating analyser. b) The path of a single light beam hitting a thin film spot deposited on a substrate [173].

The film thickness is determined by interference between light reflecting from the surface and light traveling through the film. For this reason, ellipsometry is typically used for films with thickness from sub-nanometres to a few microns maximum and quite transparent properties in the spectral range of investigation. Indeed, light should be able to come out from the sample to be analysed [173]. It should be noticed that thickness measurements are not independent of the optical constants; the thickness affects the path length of light traveling through the film, while the index determines its velocity and refracted angle. Thus, they are correlated with each other [173]. Generally, for the easiest case,

our samples can be generally treated as Cauchy layers, namely materials not showing any absorption peak in the spectral range of investigation [174]. For the so-called Cauchy layers, the refractive index n follows the Cauchy equation:

$$n(\lambda) = A_n + \frac{B_n}{\lambda^2} + \frac{C_n}{\lambda^4} \tag{3.14}$$

where λ is the wavelength and A_n, B_n and C_n are the fitting parameters [174].

3.5.2.Fourier transform infrared spectroscopy (FTIR)

Infrared spectroscopy has been a workhorse technique for materials analysis for over seventy years. Indeed, an infrared spectrum represents a fingerprint of one sample, since each absorption peak occurs at the vibration frequency of a specific atom bond present in the material [175]. Each different material is a unique combination of atoms, then two compounds never produce the exact same infrared spectrum. Therefore, infrared spectroscopy can result in a qualitative analysis of the sample composition [175]. In addition, the size of the peaks in the spectrum could act as a direct indication of the amount of present elements.

Fourier transform infrared (FTIR) spectroscopy was developed to overcome the slow scanning process of dispersive instruments, as it measures all the infrared frequencies simultaneously, rather than individually. The solution is given by the presence of an interferometer and the measurement usually takes few seconds [175].

The principle at the basis of FTIR spectrometry is the separation of an incoming infrared light beam into two individual beams using an optical beamsplitter, followed by variation of the optical path difference between these two beams using a movable mirror for one beam and a fixed mirror for the other, and by recombination on the beamsplitter of the two separate beams so that interference occurs (Figure 3.11a) [176]. After the recombination, the generated beam is sent to the sample, and then to a semiconductor detector. For generic polychromatic light sources, a complicated function is obtained, the interferogram, reported in Figure 3.11b. To obtain the original spectrum from it, the interferogram is numerically Fourier transformed using the fast Fourier transform (FFT) (Figure 3.11b) [176].

Although the experimental basis for FTIR spectroscopy was founded by Michelson in the late nineteenth century, it became widely distributed only in

the past decades of the twentieth century, due to the need of fast personal computers for the calculation of the FFT [176].

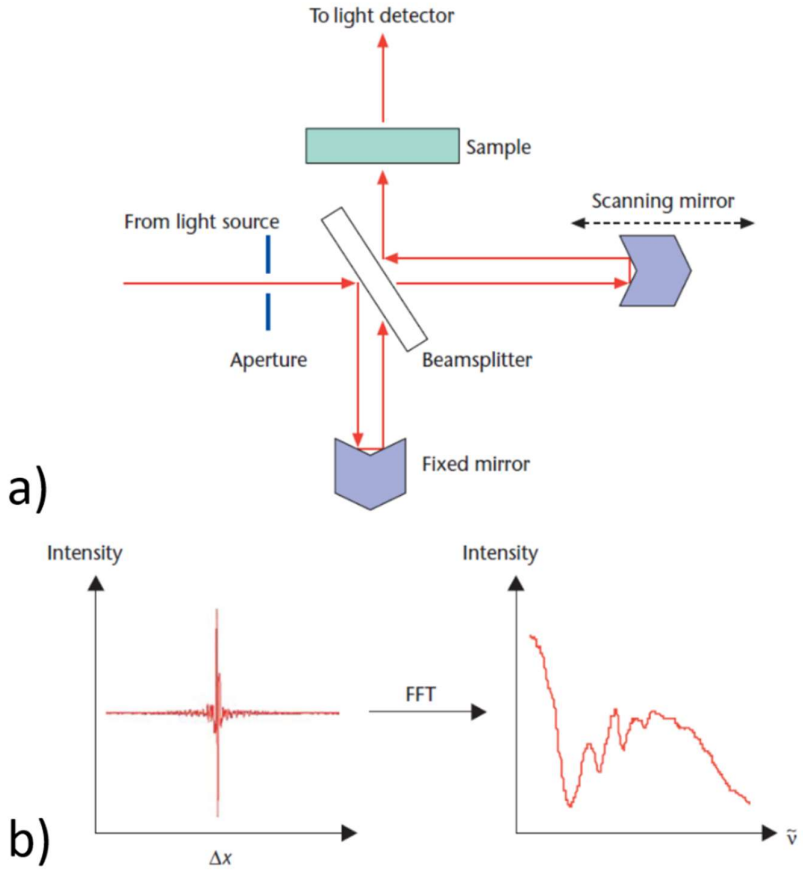

Figure 3.11 a) Typical setup of a FTIR spectrometer. b) The acquired interferogram, that is a function of the optical path difference between the two mirrors and the corresponding FFT calculation of the infrared spectrum [176].

3.5.3.Photoconductance decay (PCD)

The measurement of carrier lifetimes is based on the recombination dynamics of excess carriers which are normally generated optically. The techniques may differ in terms of the time dependence of the illumination and of measuring the excess carrier density. Concerning the first parameter, three operating regimes can be distinguished:

1. A sharp pulse of illumination is rapidly turned off and the excess carrier density is determined without illumination (transient regime).

2. The measurement is performed under steady-state illumination (steady-state regime); the major problem of this regime is the heating of the samples, which alters the real value of lifetime.
3. The illumination intensity is slowly reduced to zero over several milliseconds, so that the decay is long enough to ensure a steady state in terms of the recombination processes avoiding the heating issue (quasi-steady-state method).

The first two regimes are special cases of the third, which therefore represents the general case [177]. The detailed analysis of the recombination dynamics in all three cases is based on the continuity equation for the excess minority carriers:

$$\frac{\partial \Delta n}{\partial t} = G_{bulk}(t,x) - U_{bulk}(t,x) + \frac{1}{q}\frac{dJ_n}{dx} \tag{3.15}$$

where G_{bulk} and U_{bulk} are the photogeneration rate and the recombination rate in the bulk, Δn the excess minority carrier density and J_n the electron current density. When Equation (3.15) is integrated over the sample width, the transport term reduces to surface recombination, because the sample is in open-circuit conditions [177].
To define an effective lifetime regardless of the decay time of the illumination source, the bulk and surface recombination rates are generally combined into an effective recombination rate U_{eff}. In this way, an expression for the effective carrier lifetime τ_{eff} can be written; for the quasi-steady-state case it is:

$$\tau_{eff} = \frac{\Delta n_{av}}{G_{av}(t)} \tag{3.16}$$

where n_{av} is the average excess carrier density and G_{av} the average generation rate, both calculated over the whole wafer thickness. This expression is only valid when the carrier lifetime is significantly lower than the decay time of the illumination source [177].
In a PCD measurement, the photoconductor sample is uniformly illuminated by the light pulses, causing an adequate generation of the excess carriers and photocurrent variation. The photocurrent is then recorded as a drop of the voltage on the resistor connected in series. The decay of photocurrent can be observed on an oscilloscope and the effective lifetime can be measured [178].

An example of a photoconductance signal of a FZ silicon wafer is reported in Figure 3.12.

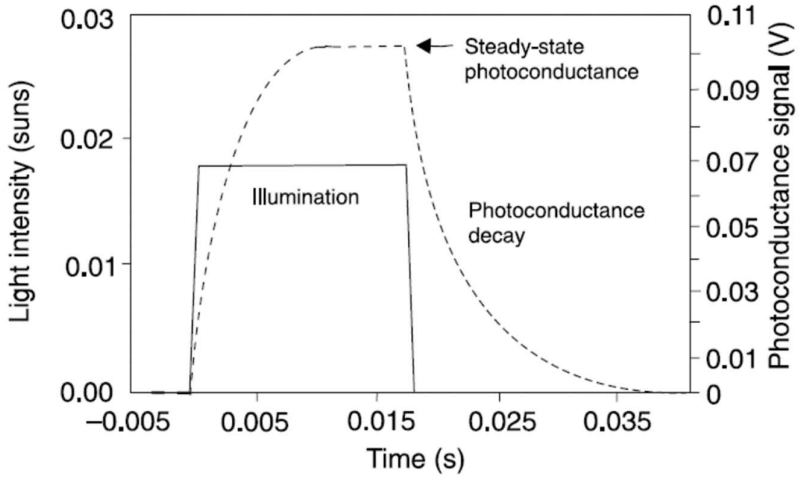

Figure 3.12 Photoconductance response of a high resistivity FZ silicon wafer to a square pulse of light produced by an array of red LEDs [178].

4 Experiments

In this section the details of the various experiments will be described.

4.1.1.c-AFM acquisitions on nc-SiO_xN_y layers

The acquisitions of the c-AFM maps on nc-SiO_xN_y layers were performed using the Park NX10 system in contact mode with entirely-Pt probe (RMN 25Pt300B), with tip radius smaller than 20 nm. A fixed bias is applied to the sample: indeed, an ohmic contact is produced with conductive silver paste on the sample top side (as shown in the inset of Figure 5.6, in Section 5.1). Fresh tips were always used, to avoid the well-known problem of the tip wearing [10]. Several maps in different areas of the same sample were acquired to check their reproducibility.
To avoid artefacts and the tip damaging, small interaction forces between the tip and the samples have been employed (600-650 nN). The investigation of always fresh areas of the surface was necessary, since we experienced huge local oxidation effects. As an example, the c-AFM maps of one nc-SiO_xN_y sample is shown in Figure 4.1.

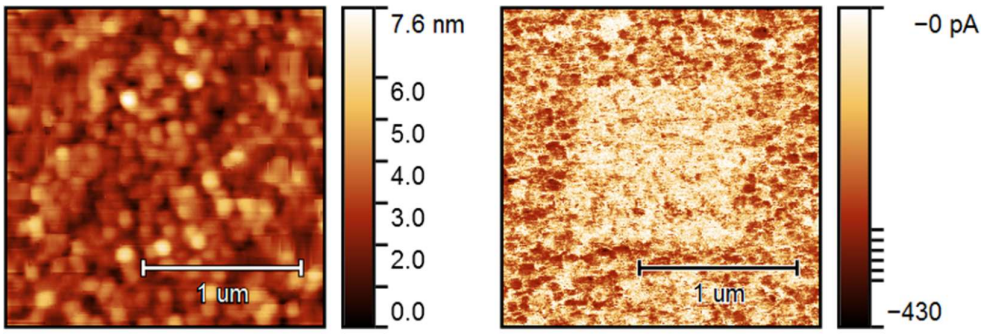

Figure 4.1 c-AFM acquisitions of sample H3h with an applied bias of -0.4 V of a) topography and b) current maps. An area of 1 μm^2 was previously scanned; then, a larger area of 4 μm^2 was investigated. The previously scanned area (lighter central area in the map b)) is charged and then less conductive [86].

This approach also helps to avoid hysteresis effects in the current-voltage characteristics. The effect of the tip-contact distance on the current values was also checked. The current flow between the tip and the sample (inset of Figure 5.6, in Section 5.1) is extracted from the tip in each point of the map

and recorded after being amplified. When positive and negative biases are applied to the sample, hole and electron currents are measured, respectively. After the acquisition of the maps, current-voltage (I-V) characteristics have been obtained in several selected highly conductive points of the sample; a continuous and linear variation of the bias is applied to the sample.

4.1.1.SPV measurements

In this subsection, a detailed description of the SPV setup is present together with the experiment details for each sample set.

4.1.1.1. SPV setup

A schematic view of our experimental set-up for SPV measurements is shown in Figure 4.2 [179]. To obtain spectroscopic measurements, a white light source has been employed in combination with a monochromator. As continuum white light sources, a QTH lamp and an ozone free short arc xenon (Xe) lamp have been employed. The former consists of a quartz bulb containing both a rare gas and small amounts of halogen, where a tungsten filament is able to emit light when heated at high temperatures. The spectral irradiance of a QTH lamp changes with the filament temperature, *i.e.* with the applied voltage (in our case, equal to 23 V) [180]. The Xe lamp is a gas discharge lamp, emitting light by passing electricity through ionized Xe gas at high pressure [181]. Both light sources can be considered as black-bodies in their emission spectra; however, their maximum emission occurs at different energy values: around 1 eV for the QTH, and at 2-3 eV for the Xe lamp. In this way, the use of both lamps has allowed us to perform the spectral analysis in different wavelength ranges. The overall range of investigation is shown in Figure 4.3, where the spectra of the lamps have been measured through a pyroelectric sensor [182].

Due to the very low signals investigated by SPV technique (generally from 10^{-3} to 10^{-7} V), the presence of a lock-in amplifier is mandatory. So, to provide an alternating signal, as well as a reference frequency for the amplifier, a chopper is placed just before the input entrance of the monochromator.

A spectrometer (500M SPEX) is needed to obtain a monochromatic light. The measurements of the light induced variations of surface or interface voltage are capacitively picked up in a metal-insulator-semiconductor (MIS) configuration, where the air acts as the insulator and either an ITO-coated glass (indium tin oxide) or a metallic (copper) grid has been placed in front of the sample (semiconductor) as transparent electrode. The samples have been

back-grounded with silver conductive paste. Before reaching the lock-in amplifier, the voltage signal passes through a high input impedance pre-amplifier, that works mostly as a buffer amplifier. All the data can be acquired by a LabVIEW Virtual Instrument real-time software SPS_Data_Acquisition.vi, previously developed to interface the SPS instrumental set-up [88]. In the setup, a focusing quartz lens (f = 20 mm) has been added to the exit to better focus the beam on the sample and achieve a higher signal.

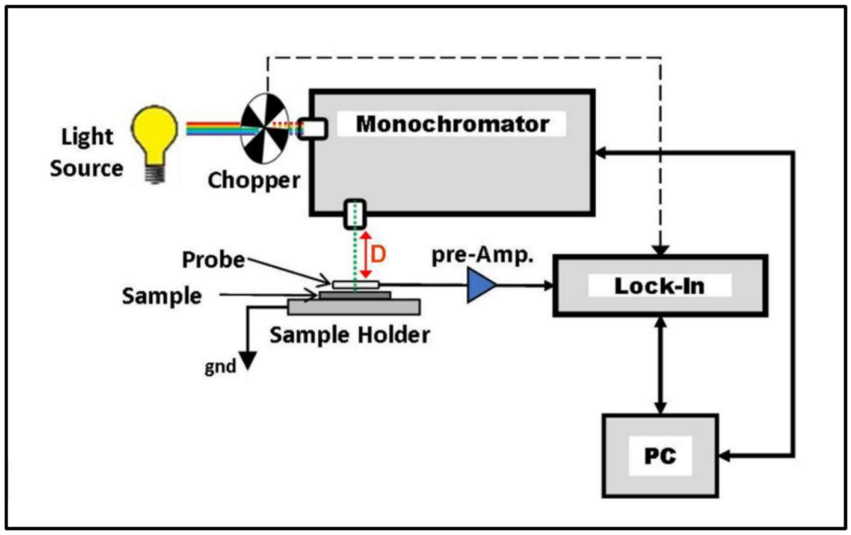

Figure 4.2 Block diagram of the SPV experimental apparatus [179].

Although the output light source is considered purely monochromatic, a spectral broadening (or effective bandwidth) of the wavelength will always exist in a real spectrometer. This finite width is called instrumental line profile or bandpass (BP) and represents an estimate of the instrument ability to isolate adjacent spectral lines. Since the monochromator has been never used at its resolution limit (*i.e.* 0.02 nm [183]), the width of the monochromator slits are the dominant factor of the bandpass.
Therefore, the BP is obtained from the convolution of the two functions $\Delta\lambda_1$ and $\Delta\lambda_2$ (as shown in Figure 4.4), each one defined as the product of the linear dispersion D and the width $w_{1,2}$ of the entrance and exit slits, respectively [184]. If the output and the input slits have the same width, the BP can be approximated as [184]:

$$BP \approx D \cdot w \tag{4.1}$$

A tradeoff is always necessary, since a narrow slit implicates fewer incident photons and, in the end, a lower SPV signal.

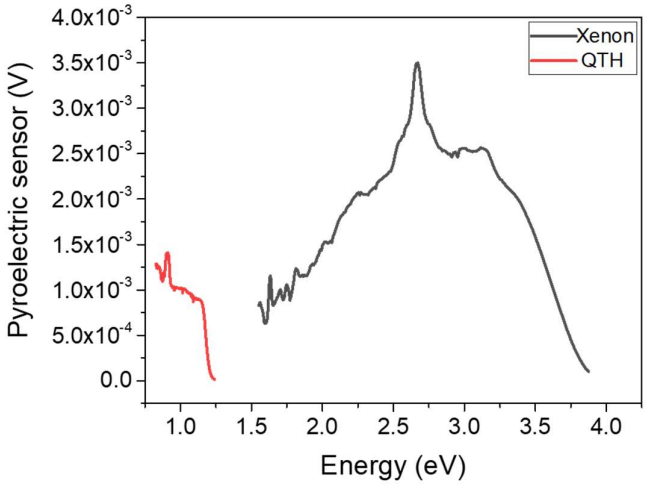

Figure 4.3 Spectra of the QTH (red solid curve) and Xe lamp (black solid curve). Adapted from [182].

The linear dispersion of the SPEX mounting a 600 gr/mm grating (the density of our diffraction grating) is equal to 3.2 nm/mm [183]; therefore, the uncertainty on the wavelength at the exit slit is given by:

$$\Delta\lambda = 1.6 \cdot w \text{ (nm)} \tag{4.2}$$

The width both slits may be varied from 3 μm to 3 mm by means of a micrometer-type knob.

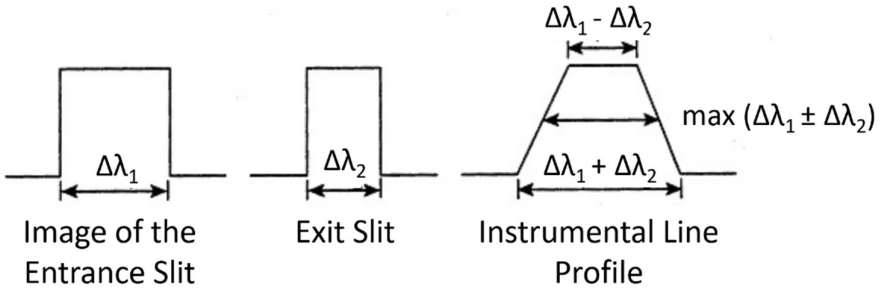

Figure 4.4 Instrumental line profile as the convolution of the entrance $\Delta\lambda_1$ and exit slits $\Delta\lambda_2$ functions [179,184].

The light intensity of both lamps is not constant with the energy of the incident photons; moreover, the diffraction grating efficiency varies within the spectrum as well. Therefore, to recognize features that exclusively belong to the SPV spectrum, the SPV signals are always normalized with respect to the number of photons as follows:

$$SPV_{norm} = \frac{SPV_{raw}}{\Phi / h\upsilon} \tag{4.3}$$

where SPV_{raw} is the signal as it is extracted from the lock-in amplifier, Φ is the photon flux measured by a pyroelectric sensor (which has a flat response in the overall range), and $h\upsilon$ is the energy of the incident photons.
In addition, since the main features of the SPV spectra (electronic transitions in the sample) are represented by slope changes (see Section 3.4.1), sometimes we can more easily distinguish these points as maxima or minima in the numerical derivative of the normalized SPV signal [146,151]. Since the SPV signal is proportional to the open-circuit voltage V_{oc}, it follows that it is proportional to the absorption coefficient α, so [146]:

$$\frac{d[SPV_{norm}(E)]}{dE} \propto \frac{d\alpha}{dE} \tag{4.4}$$

4.1.2. SPV analysis on nc-SiO_xN_y layers

Electronic transitions of nc-SiO_xN_y samples (see Table 2.1) have been determined by SPV measurements. The SPV setup has been described in Section 4.1.1.1. The short arc Xe lamp has been used as light source, to investigate high energy spectra (maximum efficiency at 2-3 eV). The raw SPV signal intensity has been normalized to the photon flux (see Section 4.1.1.1) and plotted as a function of the photon energy.
To easily detect the features in the spectra related to electronic transitions within the layers, derivative spectra have also been extracted and analysed (see Section 4.1.1.1).

4.1.1. SPV analysis on a-SiO_x and a-SiO_xN_y layers

Electronic transitions and effective minority carrier lifetimes of a-SiO_x and a-SiO_xN_y samples (see Table 2.3) have been determined by SPV measurements. SPV spectra have been recorded using the laboratory-made apparatus described in Section 4.1.1.1 based on a 500M SPEX spectrometer by a LabView software. Both QTH and Xe lamps were used to inject photons in different

spectral ranges. The raw SPV signal intensity was normalized to the photon flux (see Section 4.1.1.1) and plotted as a function of the photon energy.
Two standard methods of the spectra analysis have been employed. In the first method (referred to as SPV spectroscopy), the whole spectrum is measured at a fixed chopper frequency; whereas, the second method consists of ac-SPV (see Section 3.4.4). In this way, both electronic transitions and effective minority carrier lifetimes can be determined.

4.1.2.SPV on ternary and quaternary alloys of III-N on GaN structures

Electronic transitions of all ternary alloys III-N on GaN structures, Si doped $In_xGa_{1-x}N$, undoped $In_xGa_{1-x}N$ and $Al_xIn_yGa_{1-x-y}N$ thin films (see Table 2.6 and Table 2.8) have been determined by SPV measurements.
SPV spectra have been acquired using the laboratory-made apparatus described in Section 4.1.1.1 based on a 500M SPEX spectrometer by a LabView software. Xe lamp has been used to inject photons in high energy spectral ranges. The raw SPV signal intensity has been eventually normalized to the photon flux (see Section 4.1.1.1) and plotted as a function of the photon energy. Figure 4.5 shows the absorption coefficient α (blue curve) and the light penetration depth α^{-1} (black line) of InGaN as a function of the photon energy. It can be noticed that for $hv > E_{g,GaN}$, absorption occurs in InGaN top layer up to 50 nm, while the rest takes place in the GaN substrate. As far as we move the photon energy above $E_{g,GaN}$, we could get information about the InGaN/GaN interface by SPV measurements.

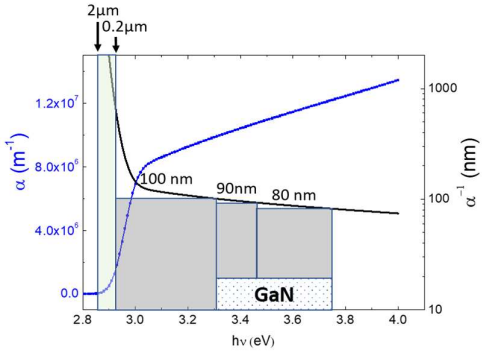

Figure 4.5 InGaN absorption coefficient α (blue curve) and penetration depth α^{-1} (black curve) *vs.* photon energy. The region where GaN absorption takes place is highlighted. A. Minj, private communication.

It should be noticed that the Xe lamp can investigate spectra up to 3.7 eV, since the photon flux dramatically decreases at higher energies. For this reason,

we could only investigate the GaN substrate and its interface with this setup on AlInGaN samples, due to the its very high band gap.

4.2 Additional techniques on a-SiO$_x$N$_y$ and a-SiO$_x$ thin films

Here we report all the additional techniques employed in the multi-characterization of a-SiO$_x$N$_y$ and a-SiO$_x$ thin films, such as FTIR spectroscopy, spectral ellipsometry and PCD measurements.

4.2.1. FTIR spectroscopy

In the a-SiO$_x$ and a-SiO$_x$N$_y$ layers microstructure and nitrogen and oxygen incorporation has been qualitatively determined by FTIR spectra from 500 to 2500 cm^{-1}. The FTIR spectroscopy technique is briefly reported in Section 3.5.2. The setup is a Vertex 80 from Bruker Optics spectrometer with a resolution of 8 cm^{-1}. Two main absorption bands have been identified, namely the low frequency band (LFB) (550–1200 cm^{-1}) and the high frequency band (HFB) (1950–2150 cm^{-1}). The two bands have been fitted with a multi-Gaussian approach, after individually applying a baseline correction. The peak positions as reported in literature are listed in Table 4.1.

Wavenumber (cm^{-1})	Bonds	Modes	Ref.
640	Si-H / Si-H$_2$	wag / roll	[185]
780	Si-H / Si-O-Si	coupling of both bonds	[186]
840	Si-H$_2$	interaction between two Si-H$_2$ groups	[185]
850	Si-N	asymmetric stretch	[187]
890	Si-H$_2$	interaction between two Si-H$_2$ groups	[185]
980	Si-O-Si	asymmetric stretch	[186]
1107	O$_i$	interstitial oxygen	[188]
2000	Si-H	stretch	[189]
2100	Si-H$_2$ / Si-H$_3$	stretch	[189]

Table 4.1 Infrared active absorption peaks values from literature, together with the corresponding bonds, their vibration types and the related references. The peaks are all present in the investigated samples [190].

To obtain a qualitative comparison of selected bond density in different samples, relative absorption strengths for each peak of interest have been calculated. This quantity has been determined as the ratio between the integral under the fitted Gaussian peak in the sample spectrum and the integral under the corresponding peak of a reference sample spectrum [190].

4.2.2.Spectral ellipsometry

Information on the layers refractive index and thicknesses has been extracted employing a Vertical VASE Rotating analyser ellipsometer (J.A. Woollam Co., Inc.), in a spectral range from 500 to 2000 nm. The theory behind this method is reported in Section 3.5.1.
The spectra were fitted by a graded Cauchy model, in which the layer is divided into several sublayers (21 in this case) and each sublayer is modelled as a Cauchy layer with an individual homogeneous refractive index. In the graded Cauchy model, each sublayer follows Equation (3.14); with this partition an evaluation of the differences in the optical constant within the same layer is possible, similarly to the approach in [191]. To simulate roughness on the top surface of the layer, an additional layer was added on top, composed by: 50% of the underlying layer material and 50% of void [174].

4.2.3.PCD measurements

A parallel estimate of passivation quality with respect to the ac-SPV was extracted by effective minority carrier lifetime measurements using a PCD tool (WCT 120 from Sinton Instruments Inc.). PCD technique have been explained in detail in Section 3.5.3. The excess carrier density was fixed at Δn of $1 \cdot 10^{15}$ cm^{-3}. The relative error for this characterization method is 8%, as suggested in [192,193].

4.3 AFM on $LaVO_3$ thin films

Non-contact AFM maps were acquired to investigate morphological properties of the $LaVO_3$ samples at the nanoscale. For each sample, maps of different size were acquired. The morphological maps have been acquired by a Park NX10 system at room temperature and in ambient atmosphere. The tips used feature a super-sharp apex, with a curvature radius less than 5 nm (Nanosensors SSS-NCHR). To acquire non-distorted images of the sample, several corrections are performed by the open-source software Gwyddion [81]. Firstly, a plane levelling is necessary to remove slopes due to a tilted installation of the

sample or by the intrinsic tilted surface of the sample. Then, a line-by-line average removal helps in the removal of steps parallel to the scanning direction caused by continuous changes in the tip-sample distance during the scanning.
After all image processing is done, morphological analysis can be performed on the maps. By Gwyddion software, the operator can extract several statistical parameters; for example, those correlated to surface roughness.
In detail, the root mean square roughness (RMS) can be obtained as the square root of the arithmetic mean of the square of the vertical deviation from the average height:

$$RMS = \sqrt{\frac{1}{N}\sum_{j=1}^{N}(r_j - \bar{r})^2} \tag{4.5}$$

where N is the number of pixels on a row/column, r_j is the value of the j-th point and $\bar{r}$ is the average height [81]. RMS is quite useful in this case to compare the roughness of different $LaVO_3$ samples and to correlate it with the changed parameters, such as substrate, deposition technique and thickness.

4.4 EFM and KPFM on $LaVO_3$ layers

EFM and KPFM maps have been acquired by the same system, employing Au coated tips with a nominal curvature radius less than 50 nm. The investigation has been performed both on the $LaVO_3$ surface and at the $LaVO_3$/ZnO interface. By Gwiddion, we could simply extract the average value of the measured bias from selected regions of the image. From the V_{CPD} (defined in Equation (3.2)) extracted from KPFM maps on both sides, the work functions of the two materials and the barrier height at the junction could be evaluated.

5 Results and discussion

In this Section all results have been presented, for each sample set.

5.1 Results on nc-SiO$_x$N$_y$

All the nc-SiO$_x$N$_y$ samples (see Table 2.1) have been analysed using c-AFM and SPV techniques.

5.1.1. c-AFM analysis

Electrical properties at the nanoscale of nc-SiO$_x$N$_y$ and nc-Si:H layers (see Table 2.1) have been measured by c-AFM technique. A constant bias (both negative and positive) is applied to the sample during the overall map acquisition. The maps are 1×1 μm^2 maps, with a resolution of 512×512 px. After recording each map, highly conductive points on the current maps have been selected and I-V characteristics have been extracted in these specific points.
Among an extended family of nc-SiO$_x$N$_y$ samples grown with different deposition conditions, the samples reported in Table 2.1 have been selected to analyse individually crystalline fraction and N_2O content effects on the nanoscale electrical properties.
In detail, as displayed in Table 2.1, the samples L0h and L3h have been deposited with the same N_2O content, whereas the thermal treatment duration differs; this dissimilarity generates a variation in crystallinity. On the contrary, samples H3h and L3h share the same annealing time, but the N_2O contents are different: the first is deposited with a higher flux and results in lower crystallinity than the second [19].
Secondary-ion mass spectrometry (SIMS) measurements have already shown that increasing R_{N2O} (see Equation (2.1)) is mostly correlated to an oxygen content rise, whereas nitrogen concentration remains almost unchanged [18]. As N_2O dilution increases (*i.e.* with higher oxygen contents within the layers), both crystallinity fraction and electrical conductivity decrease [19]. Moreover, an additional annealing step after deposition promotes recrystallization of the layers, since an increase of the crystalline fraction occurs [19]. In addition, the thermal process induces clustering of grain-like structures on nc-SiO$_x$N$_y$ surface (as shown in Section 2.1) and boosts the optical bandgap up to 2.5 eV [30].

As regards the nc-Si:H samples, a very abrupt transition from the amorphous to the nanocrystalline phase occurs as the R_{H2} dilution increases; this

transition occurs with a large variation in the dark conductivity of the samples [194,195]. Since the crystallites' growth is island-like, both crystallinity and macroscopic conductivity boost with the layer thickness [195,196]. In this analysis, two samples of nc-Si:H have been investigated with different thicknesses, but same deposition conditions (see Table 2.1); it is worth noting that changes in thickness result in a different crystal fraction (Table 2.1).
Figure 5.1a,c,e report AFM topography maps of the nc-SiO_xN_y samples L3h, L0h and H3h, respectively, whereas Figure 5.1b,d,f show the corresponding current maps. L3h and L0h have the same low amount of incorporated oxygen but different annealing times, whereas H3h has the highest O inclusion but the same annealing time (3 hours) of L3h. The lowest values of applied bias capable to give measurable signals have been used, to reduce tip induced damage and possible artefacts in the maps [105]. Moreover, since the contact to provide the voltage to the samples was made on the top of the sample (see inset of Figure 5.6), we are sure that the current is coming from the sample layer only and so the extracted electrical conductance belongs exclusively to the sample and not to the FZ-Si substrate.

Several maps of different sizes have been acquired for each sample; the maps reported in Figure 5.1 show typical examples. We can assume that the current maps reflect the transport properties of the top layers, since the substrate has a higher electrical resistance than the deposited samples. Both topography and current maps on nc-SiO_xN_y samples show grain-like structures on the surface, probably related to nanocrystals clustering [19]. Moreover, comparing topography and current maps, it is visible that these highest conductive areas correspond to the grain structures. Indeed, the lightest areas in the current maps correspond to the highest conductive regions (positive bias). It is visible that the grain conductivity is affected by annealing time and/or oxygen content; this result is evident if one compares the current ranges in the c-AFM maps. Lastly, looking at the maps, the grains are surrounded by darker less conductive areas, meaning that the grains are embedded into an amorphous and less conductive matrix. A further comparison between the conductance distributions of the samples has been performed to achieve quantitative information on the influence of annealing time and O content on the grain conductivity. The electrical conductance has been classically extracted as the ratio between the flowing current and the applied voltage for each point of the map. To obtain conductance distributions, a binning process has been performed on the data. The first bin centre has been selected at $5 \cdot 10^{-14}$ S and

the bin width of $1 \cdot 10^{-13}$ S for all the samples for positive and negative biases. This choice has been made as a compromise to give a fine binning process for all the samples.

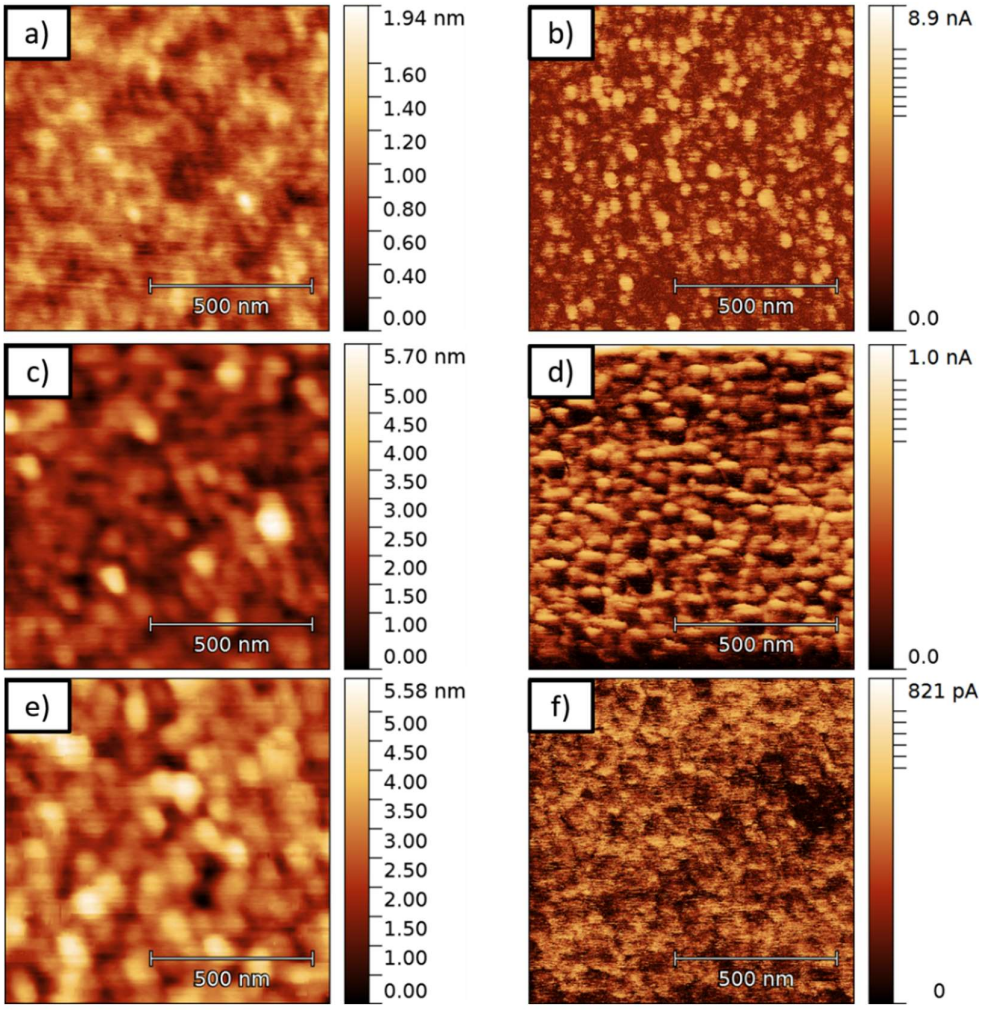

Figure 5.1 Morphological (left) and current (right) maps, respectively, of nc-SiO_xN_y samples a)-b) L3h at 0.1 V, c)-d) L0h at 1.5 V and e)-f) H3h at 0.4 V.

The results are reported in Figure 5.2 for negative and positive biases; a reduced conductivity range of 0-40 pS has been considered for sake of clarity. L0h and H3h show a higher number of counts at negative bias, while L3h at positive bias. This result indicates that without annealing (L0h) and with annealing but increasing the O content (H3h), the main contribution to the electrical current comes from the electrons; whereas the coupling of annealing and low O content (L3h) leads to a prevailing holes contribution to the current.

Moreover, the conductance distributions vary also in shape; in addition, a difference is observable the conductive grains distribution over the c-AFM maps. To quantitatively evaluate this difference, the approach shown in Figure 5.3 was used. Here, the conductance distributions at negative applied bias are reported in their entire range.

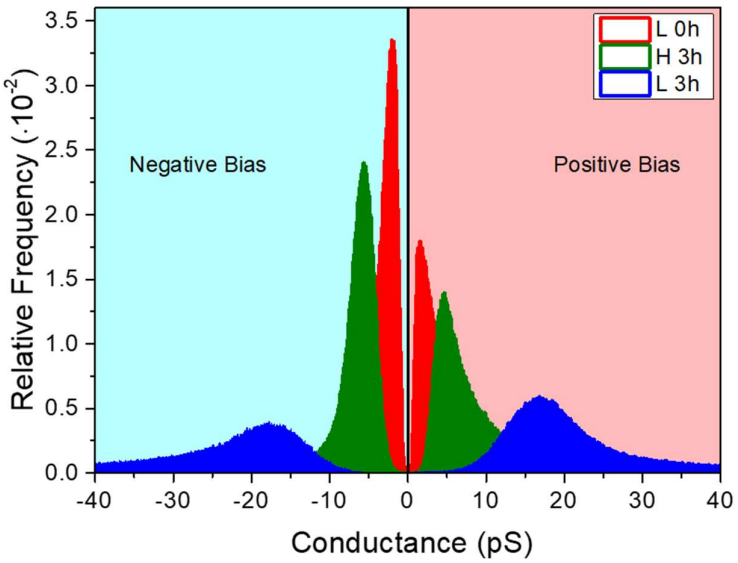

Figure 5.2 Conductance distributions for L0h (red), H3h (green) and L3h (blue) nc-SiO_xN_y samples for negative (light blue zone) and positive (light red zone) applied biases. Negative conductance values refer to negative applied values.

Comparing the ranges of the different samples, it is visible that the conductance range significantly differs and spreads over four orders of magnitude (from 0.04 to 100 nS); whereas the distribution peak, corresponding to the value of highest frequency, shifts from 2 to 16 pS as the sample changes. From this distribution investigation, it can be concluded that the most conductive sample is L3h, the one with low oxygen content and annealed, followed by H3h, with high O inclusion and annealed, close to L0h, with low O content and as-deposited. This result is in good agreement with the macroscopic electrical characterization of previous studies [19].
To better observe the differences in the distribution of the highly conductive grains over the maps, an arbitrary threshold is fixed at 20% of all the counts in Figure 5.3.

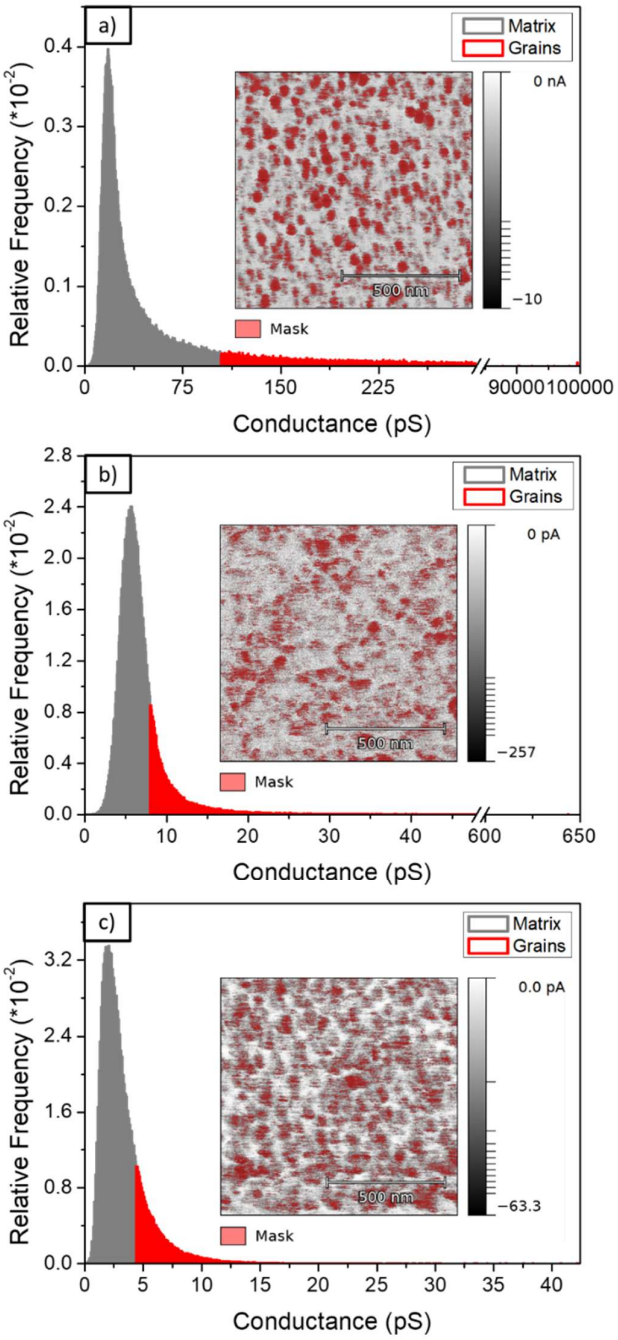

Figure 5.3 Conductance distributions for negative biases of a) L3h (-0.1 V), b) H3h (-0.4 V), c) L0h (-1.5 V) nc-SiO_xN_y samples, respectively. A fixed threshold at 20% of all counts separates the high conductive contribution (red tail) from the low conductive one (grey peak). The corresponding current maps are reported in the respective insets.

This method visually separates the high conductive tail (red bins) from the low conductive peak (grey bins). The threshold in the conductance distributions is then reported in the c-AFM maps (Figure 5.3a-c insets). As the pictures show, in the most conductive layer (L3h) there is a net separation between highly conductive grains and the amorphous surrounding. Indeed, high conductive grains agglomerate forming clusters in this sample, while the high conductive points are more homogeneously distributed within the map for the less conductive ones. This result is in agreement with coalescence and clustering of nanocrystals and O relocation in L3h evidenced in previous studies [19]. Figure 5.4 shows the morphological (a-c) and current (b-d) maps for the nc-Si:H samples with different thicknesses (different deposition times, see Table 2.1) obtained with a negative applied bias.

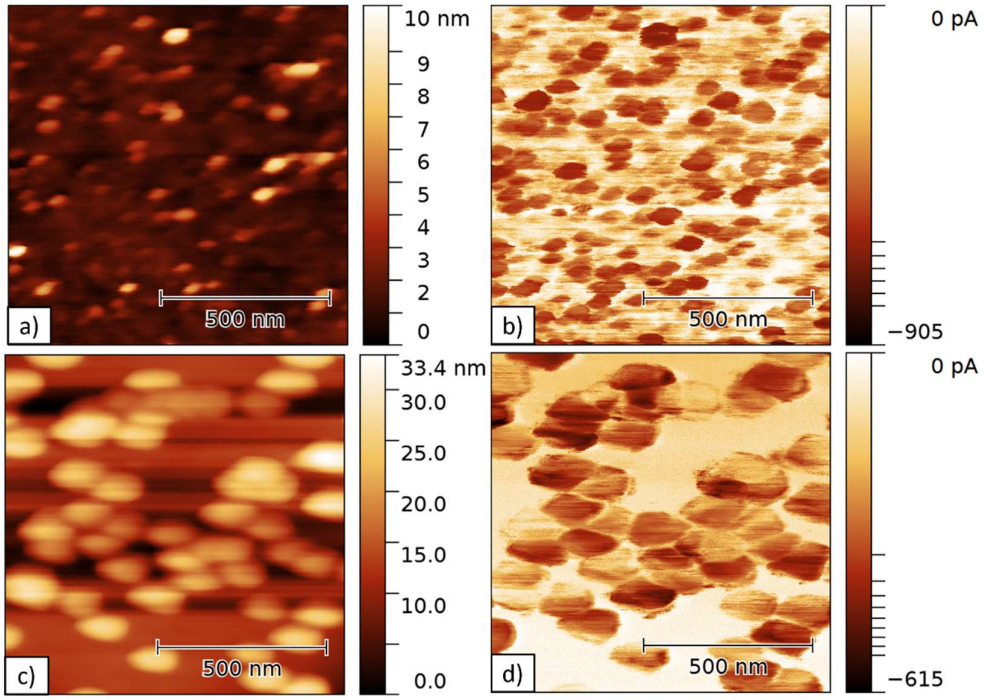

Figure 5.4 Morphological and current maps, respectively, of a)-b) Sit and c)-d) SiT nc-Si:H samples with -1.5 V and -2.5 V negative applied biases.

The grains constitute the highest conductive areas in the maps (the darker ones, negative bias); they become bigger and less numerous as the sample thickness increases. This variation is probably due to the clustering of the island-like crystalline structures as the deposition time increases.
The crystallites show different conductivities within the same map, whose range is also affected by the layer thickness if a comparison is done between

the samples (changes in the current range, Figure 5.4b,d). Macroscopically, we expected that the thicker sample (SiT), which shows the highest crystallinity [194], would also be more conductive than the thinner one (Sit). However, in the present nanoscale maps the opposite occurs, since the range in the Sit map is broader than in the SiT one. The reason could be the following: the microscopic transport is reduced in sample SiT, since the current must pass through a large amorphous non-conductive area (Figure 5.4d). This region is wider than in an equivalent area of sample Sit (Figure 5.4b).
Moreover, larger grain boundaries occur in the thicker sample, due to the crystallites clustering, adding a further obstacle to the current path.
The distribution of conductivity values for negative and positive applied bias is reported in Figure 5.5. The same binning process of nc-SiO_xN_y samples has been used. It must be noted here, from the distribution height and shape differences, that the main contribution to the current for both the samples comes from hole flow.

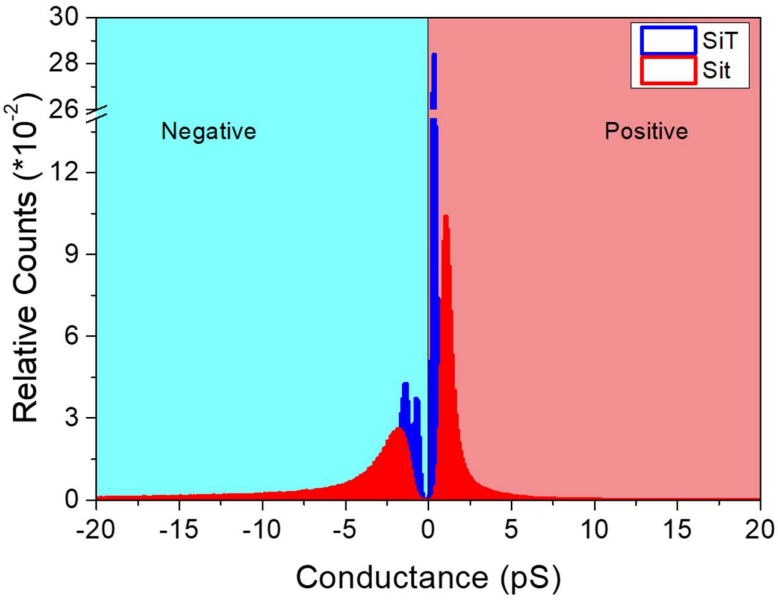

Figure 5.5 Conductance distributions for SiT (blue) and Sit (red) nc-Si:H samples for negative (light blue zone) and positive (light red zone) applied biases. Negative conductance values refer to negative applied values.

Local I-V characteristics have been measured at different highly conductive points (present in the surface grains) of the nc-SiO_xN_y samples. An example is reported in Figure 5.6 for H3h sample. A sketch of the experimental setup is shown in the relative inset. I-V curves on the amorphous non-conductive regions are not reported as they show almost zero current in the overall bias range. Stable and reproducible I-V curves have been always obtained; the differences in the curves in Figure 5.6 reflect the variation in the electrical conductivity of the grains, probably related to their dimensions and possible dopant inclusion. The curves are reported as extracted since around zero bias in a semi-log scale they would appear quite noisy.

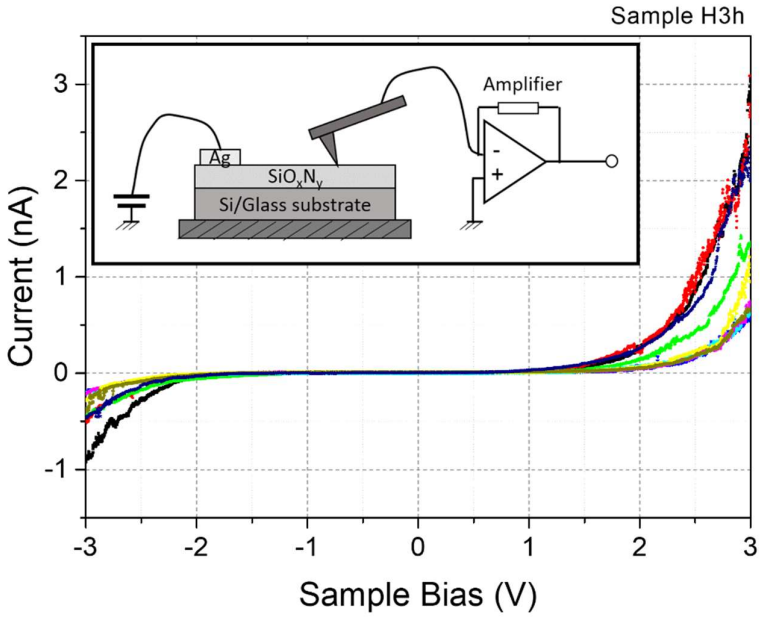

Figure 5.6 Example of several I-V characteristics for H3h nc-SiO_xN_y sample with a varying bias from -3 V to 3 V. The inset shows a scheme of the experimental setup.

This type of I-V characteristics is usually modelled as a structure of back-to-back Schottky contacts [197]. The tip-sample contact can be considered as a Schottky contact and the electronic conduction can be modelled through a thermionic-emission mechanism [198]. According to this mechanism, the free carriers emission through the interface between the metal and the semiconductor of the Schottky barrier is considered as the fundamental limiting factor in the electrical conduction [199]. In this particular case, the Schottky barrier is formed between the metallic tip and the semiconductor high conductive areas on the nc-SiO_xN_y and nc-Si:H samples surfaces. According to the thermionic-emission theory, the current-voltage characteristics at both low ($V <$

$3k_BT/q$) and reversed applied voltages can be described by the following non-ideal equation:

$$J = J_0 e^{qV/nk_BT}[1 - e^{-qV/k_BT}] \tag{5.1}$$

where $J_0 = A^{**}e^{-q\varphi_B/k_BT}$ is the inverse saturation density current, q is the elementary electrical charge, n the ideality factor, V the applied bias to the junction, k_B the Boltzmann constant, A^{**} the Richardson's constant and φ_B the barrier height of the junction [199].

By means of Equation (5.1), parameters such as the ideality factor n and the barrier height φ_B can be extracted from the current-voltage characteristics [199]. This method is also effective in the analysis of back-to-back real ohmic contacts, in order to extract their parameters at the junction [200].

In Figure 5.7 experimental data for $\ln[I/(1 - e^{-qV/k_BT})]$ of H3h sample are plotted for reverse bias values where Equation (5.1) is valid and the corresponding fit are represented as black squares and red line, respectively. The fit procedure has been performed accordingly to Equation (5.1). Similar analyses have been carried out for all the nc-SiO_xN_y and nc-Si:H samples listed in Table 2.1 in Section 2.1, and a very good agreement between the experimental I-V curves for low direct and reverse applied biases, and the fit given by Equation (5.1) has been always obtained.

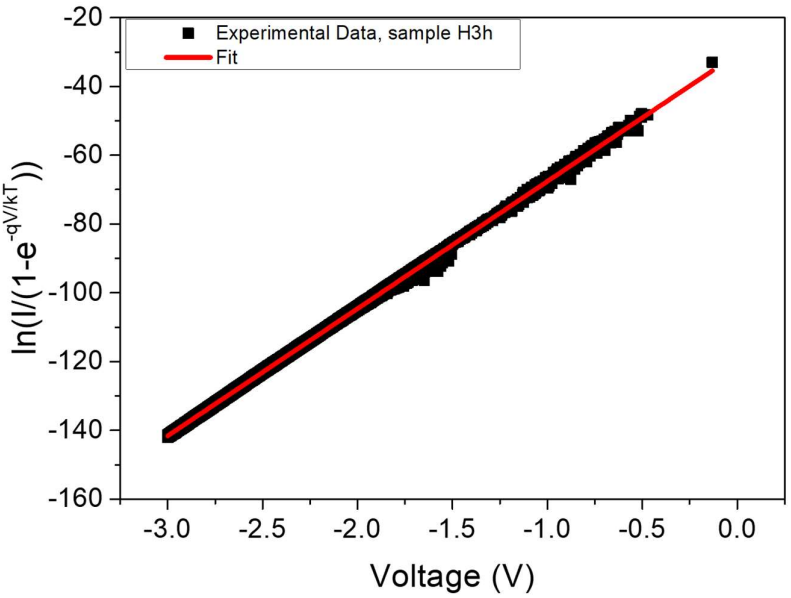

Figure 5.7 Selection of $ln[I/(1 - e^{-qV/k_BT})]$ experimental data for H3h nc-SiO_xN_y sample (black squares) and the corresponding fit (red line).

In Table 5.1 the fitting parameters are listed; in detail, the ideality factor n and the height of the Schottky barrier φ_B between the metallic tip and the high conductive areas of the samples are reported. From the listed values we can conclude that the thermionic-emission model is consistent; indeed, the ideality factor values are around 1 and the barrier height is of the same order of magnitude of the value relevant to Pt/Si junction (*i.e.* 0.5 eV) [199,201,202]. The errors in Table 5.1 also include the large uncertainties of quantities estimated from the literature (such as Richardson constant, temperature at the junction, and tip-sample contact area). It is worth noting the presence of some differences among the samples: the more conductive the samples, the lower the barrier height φ_B in the high conductive areas. Indeed, the most conductive sample L3h (both macroscopically [19] and at the nanoscale) shows the lowest barrier to the conduction from the conductive grains to the tip. The overall trend in the junction barrier height follows that of the electrical conductance at the nanoscale of the nc-SiO_xN_y samples.

Sample (label)	n	φ_B (V)
nc-SiO_xN_y (L3h)	0.9924±0.0008	0.42±0.04
nc-SiO_xN_y (L0h)	1.0422±0.0008	0.61±0.07
nc-SiO_xN_y (H3h)	1.0445±0.0006	0.60±0.07
nc-Si:H (Sit)	1.088±0.001	0.7±0.1
nc-Si:H (SiT)	1.0032±0.0005	0.44±0.04

Table 5.1 Extracted parameters of the investigated nanocrystalline samples from Equation (5.1).

In conclusion, c-AFM studies have allowed us to fulfil an in-depth characterization of the microscopic electrical properties of nc-SiO_xN_y; an analysis of the properties variations in samples deposited with different O content and annealing treatment has been carried out. Moreover, an additional comparison with nc-Si:H layers has allowed us to clarify the role of O and N content and annealing treatment on the microscopic electrical properties.
The obtained results can be summarized as follows.
In all the investigated samples, the current maps display a surface composed of conductive grains embedded in a less conductive (likely amorphous) matrix, similarly to previous results obtained on nc-Si [10,18]. Indeed, nc-SiO_xN_y layers show transport properties similar to those of nc-Si:H; however, marked differences in the conductivity range and grain distribution arise when deposition conditions change.

The comparison between nc-SiO_xN_y samples with the same O content, but different annealing time (L0h and L3h) shows that:
i) The annealing treatment enhances the Si crystallized fraction which, in turns, promotes conductivity at the nanoscale, in agreement with macroscopic measurements reported elsewhere [19].
ii) The annealing also promotes a redistribution of the conductive grains, which coalesce after 3 hours of annealing (see also Section 2.1). This redistribution is probably linked to the annealing induced O relocation, which can produce a marked separation between well-shaped highly conductive grains and a likely-amorphous matrix [19].
iii) Moreover, annealing affects the transport properties of the layers: L0h is characterized by a higher contribution of electrons, while L3h of holes on the overall current flow. This conclusion means that the holes contribution to the current prevails over the electrons contribution after annealing for samples with low O inclusion.
The comparison between samples with the same annealing conditions, but different O content (L3h, low N_2O dilution, H3h, high N_2O dilution), leads to the following results:
i) High O content prevents the formation of high Si crystallized fraction [19], and, thus, high conductivity.
ii) High O content prevents the enhancement of holes flow in electrical transport; indeed, H3h sample shows enhanced electrons flow.
At last, the comparison between nc-SiO_xN_y and nc-Si:H layers shows a prevailing hole transport in the second set of samples; however, nc-Si:H layers have a less efficient conductivity with respect to nc-SiO_xN_y ones.

5.1.2. SPV spectroscopy

The nc-SiO_xN_y samples (see Table 2.1) have been investigated by SPV technique (the details of the method in Section 4.1.2) to analyse how varying O content and/or adding an annealing step after deposition can affect the spectra. Figure 5.8 shows the normalised SPV spectra of all the samples as black lines. As main features in a SPV spectrum are related to slope changes, the derivatives of the signal dSPV/dE are also reported in Figure 5.8 as red lines. Indeed, a derivative spectrum shows peaks that can be directly related to the electronic transitions, that could be less visible directly in an SPV spectrum. The derivative at a given point is computed by taking the average of the slopes between the point and its two closest neighbours. Moreover, due to the noisiness of the SPV spectra, which is then amplified by the derivative

operation, an adjacent-averaging smoothing of the derivative curves has been performed as well. In this way, the changes in the SPV spectra slope, related to the electronic transitions in the material [146,151], are more evidenced.

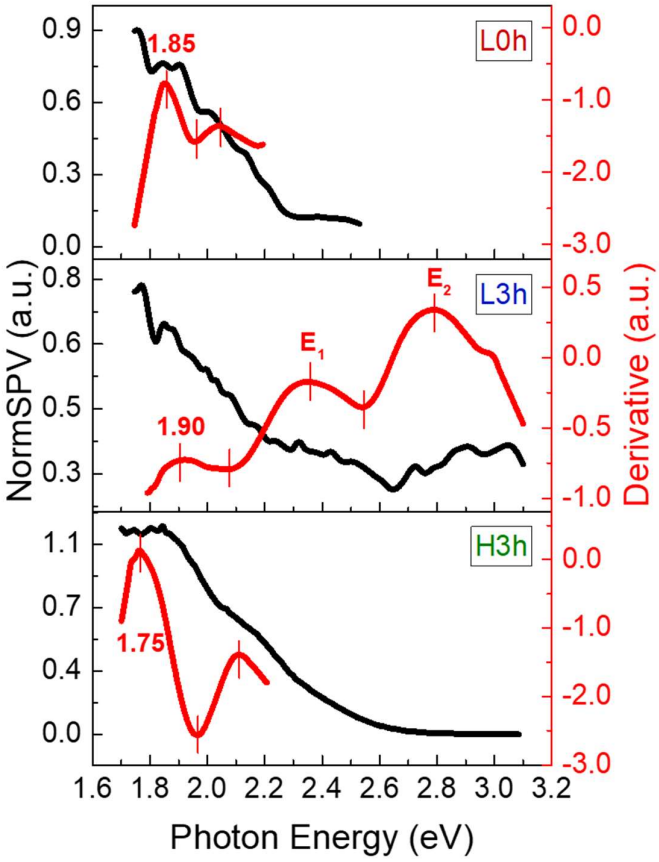

Figure 5.8 Normalized SPV (black line) and corresponding derivative (red line) spectra, obtained using the xenon lamp, for the nc-SiO_xN_y samples. Samples characteristics as follows: L0h (low O content, as-deposited), top; L3h (low O content, 3 h annealed), centre; and H3h (high O content, 3 h annealed) bottom.

At first sight, a general decrease of the SPV signal with increasing energy can be observed for all the samples. This effect is related to a decrease of the light penetration depth with increasing photon energy [146]. However, the drop is different from sample to sample. In particular, the effect is more pronounced for H3h sample (black curve in Figure 5.8, bottom position), whose spectrum is characterized by a significant broadening of the decreasing curve. The emphasised broadening might be due to wider Urbach tails (see Section 3.4.1) [146], revealing a more enhanced degree of crystal disorder in sample H3h with respect to the others [146,152,156]. This result agrees with previous studies:

the incorporation of more oxygen within the amorphous network followed by an annealing step leads to oxygen relocation, higher disorder and lower crystalline fraction [19].
On the contrary, sample L3h, the one with the highest crystal fraction, shows features in the spectrum even at higher photon energies, better evidenced in its derivative (red curve in Figure 5.8, central position). Due to the drop towards zero in L0h and H3h spectra, their derivative spectra have been considered up to almost 2.2 eV. Indeed, above this value the SPV signal almost vanishes and thus the derivative investigation becomes useless.
A maximum can be clearly distinguished in the derivative spectra of the three samples at lower photon energies, which might indicate the energy position of the bandgaps of the layers, ranging from 1.75 to 1.90 eV. These values have a trend in agreement with the Tauc gaps trend extracted from absorption measurements [19]. The derivative spectra of all the samples show a series of features (minima and maxima). These features might be indicators of quantum confinement effects occurring at the Si NCs, which are formed within the amorphous matrix due to the annealing treatment and/or H_2 gas flux during deposition, as reported in [19]. The absorption spectra of 0D confined structures typically consist of a series of discrete peaks at energies higher than the corresponding bulk bandgap, linked to optical transitions between different electron and hole levels, similar to the scheme reported in Figure 3.7 [203]. However, as commented in Section 3.4.2, the confinement could be only partial, since completely confined carries could not be able to overcome the potential barrier of the crystalline phases and to be collected and detected by the SPV setup.
In our case, the derivative spectrum of L3h layer shows a higher signal with respect to the other samples, probably less affected by the broadening due to Urbach states. Then, the spectrum can reveal the presence of additional features at energies higher than the bandgap. Some of the features in the L3h derivative spectrum ($E_1 = (2.33 \pm 0.05)$ eV and $E_2 = (2.78 \pm 0.05)$ eV) appear in agreement with the results from studies of single-dot spectroscopy on silicon quantum dots in an amorphous oxide matrix, reported by Sychugov et al. [204]. The reported errors are evaluated following the approach in Section 4.1.2. The appearance of above band-gap features also in the L0h and H3h derivative spectra could be related as well to quantum confinement at Si nanocrystals, even if nanocrystals are present in smaller density in these samples [19].

5.2 Results on a-SiO_x and a-SiO_xN_y thin films

All the a-SiO_x and a-SiO_xN_y samples (see Table 2.3) have been analysed using different techniques: FTIR, spectral ellipsometry, SPV spectroscopy, and PCD to determine the relevant surface properties of the layers and the interface quality with the c-Si substrate.

5.2.1. FTIR spectroscopy analysis

In the FTIR absorption spectra the two main bands, LFB and HFB, respectively at low and high frequencies (see Section 4.2.1), have been analysed separately. The LFB embraces all the bonds related to hydrogen, oxygen and nitrogen, whereas the HFB includes solely those correlated with hydrogen. All observed peaks are linked to the bonds listed in Table 4.1.
The overall FTIR spectra after the baseline correction for both N and C sample sets and the a-Si:H reference sample are reported in Figure 5.9a and Figure 5.9b, respectively. The two bands, HFB and LFB are highlighted.

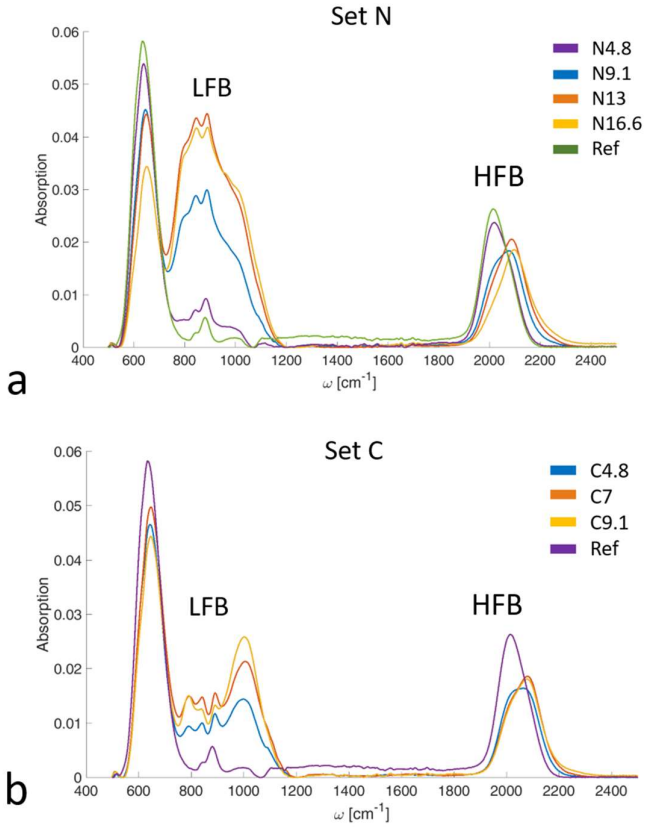

Figure 5.9 FTIR absorption spectra of a) N set, b) C set of samples, and the reference sample. The LF and HF bands are highlighted.

Surprisingly, in the C set absorption spectra, no peaks related to carbon bonds occur (to remind the sample labelling, see Section 2.2). An explanation can be found following the study in [116], in which the authors deposited similar layers with R_{CO2} range of 0%-50% and determined the carbon concentration. Following a rough linear fit from these results, a C concentration of approximately $7 \cdot 10^{18}$ cm^{-3} or $1.4 \cdot 10^{-2}$ at% can be estimated for $R_{CO2} = 9.1\%$ (*i.e.* the highest flux ratio in our C sample set). It seems reasonable that C-related absorption peaks in the FTIR spectra are not visible for such a low concentration. Anyway, this low concentration may still have an influence on the optical and electrical properties of the layers.
Contrary to carbon, a significant incorporation of N results in the N sample set. Indeed, a broad absorption peak at 850 cm^{-1} is visible in the FTIR spectra, ascribed to the asymmetric stretching mode of Si-N bond [187]. To obtain its relative absorption strength, the absorption peak integral has been normalized to that of the sample with the highest nitrogen content (*i.e.* N16.6). In the overall investigated dilution range, this quantity increases by almost a factor of six with higher R_{N2O}, as visible in Figure 5.10a (inverted blue triangles).
The three absorption peaks related to oxygen have been identified: at 780 cm^{-1} (coupling of Si–H and Si–O–Si bonds [186]), at 980 cm^{-1} (Si-O-Si asymmetrical stretching mode [186]) and at 1107 cm^{-1} (interstitial oxygen [188]). In this case, the absorption strengths have been normalized to the corresponding sample with the largest oxygen content (N16.6 or C9.1), since the reference sample does not exhibit obviously such peaks. In both sample sets, the O-related relative absorption strengths simultaneously rise with higher R_x, as reported in Figure 5.10a,b. This shared trend suggests a similar increase in the oxygen inclusion, regardless of the gas type, as expected. It can be noted for the C sample set that the 1107 cm^{-1}-peak relative absorption strength shows no clear trend (green triangles in Figure 5.10b). This unexpected inconsistency will be discussed in detail later.

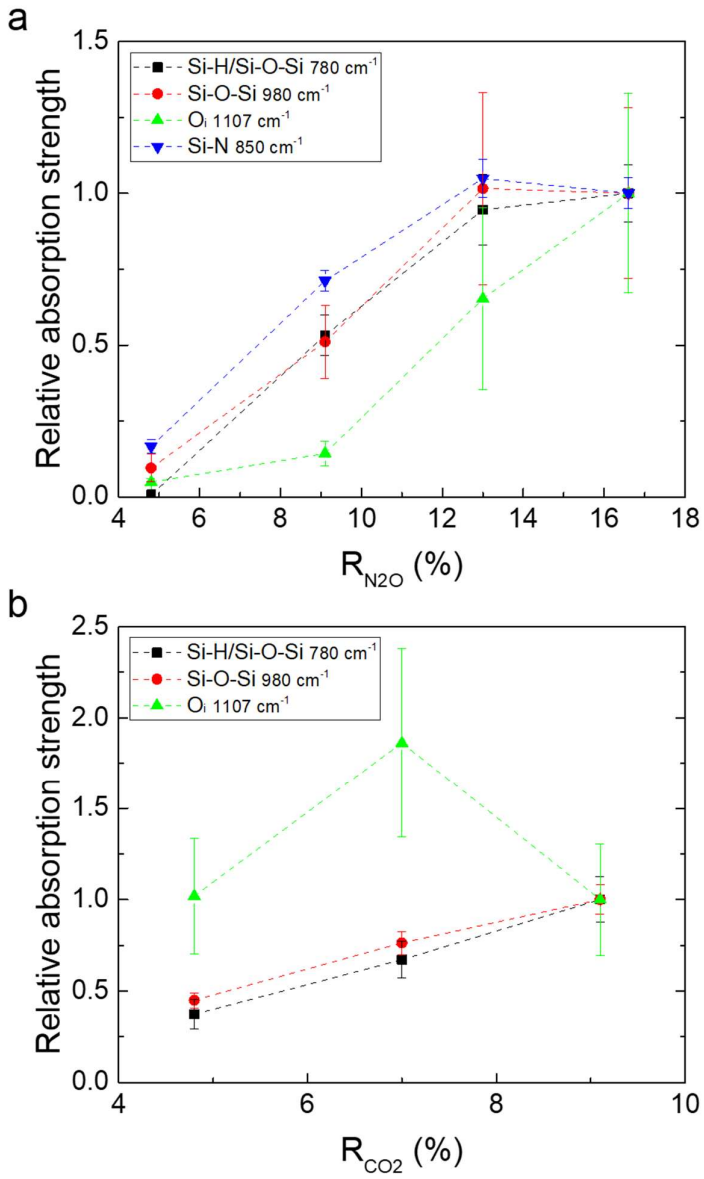

Figure 5.10 Relative absorption strengths of all oxygen (780 cm^{-1}, 980 cm^{-1}, 1107 cm^{-1}) and nitrogen (850 cm^{-1}) bonds as reported in Table 4.1 for a) the N sample set and b) the C sample set. The normalization of the absorption strengths is carried out with respect to N16.6 and C9.1 samples, respectively.

On the contrary, the absorption strengths of the peaks corresponding to hydrogen bonds have been normalized to the absorption strengths of the pure a-Si:H reference sample. They are all displayed in Figure 5.11a,b for both N and

C sample sets, respectively. For both sets the same trends occur; thus, they are discussed simultaneously.

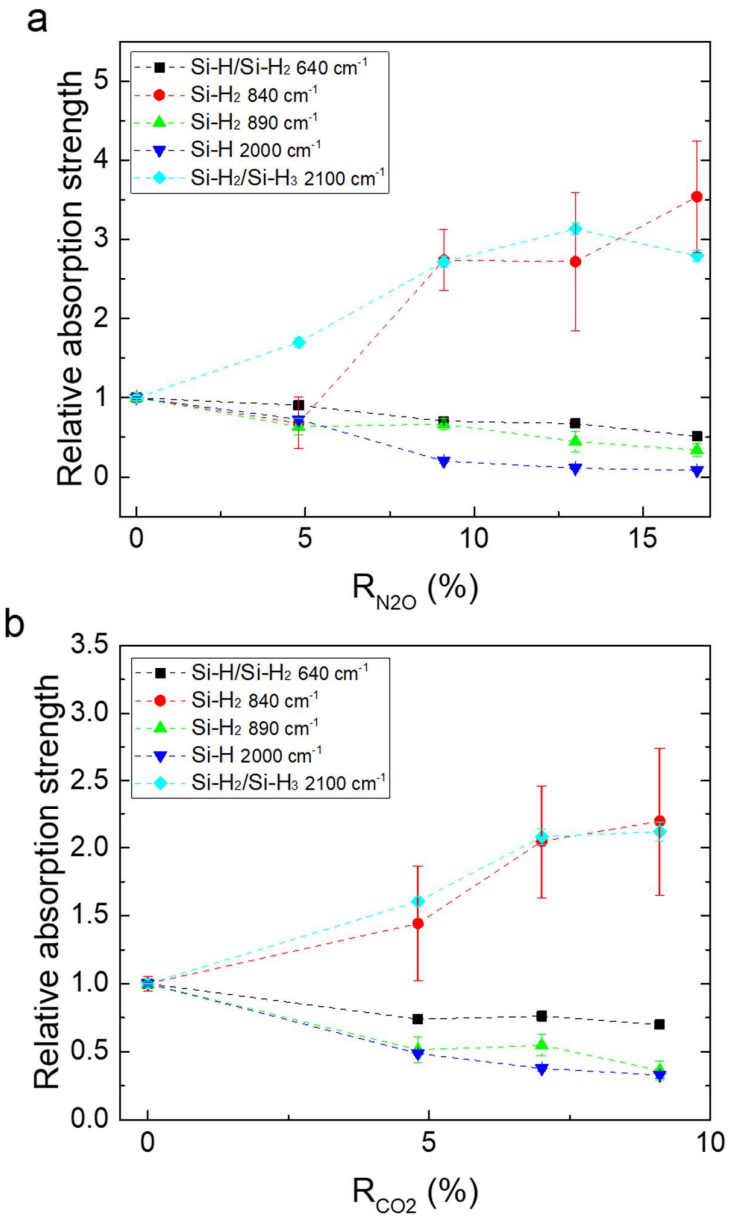

Figure 5.11 Relative absorption strengths of all hydrogen bonds as described in Table 4.1, for a) the N sample set and b) the C sample set. The normalization of the absorption strengths is carried out with respect to the a-Si:H reference sample.

The absorption peak at 640 cm^{-1} is related to both the wagging mode of Si–H bonds and the rolling mode of Si–H_2 bonds. Therefore, it commonly acts as a marker of the total hydrogen content within the layer [189,205]. Since its relative absorption strength diminishes with increasing R_x (black squares in Figure 5.11), we can conclude that the total hydrogen content is reduced.
The only two peaks occurring in the HFB can be identified with the stretching modes of Si-H (2000 cm^{-1}) and Si-H_2/Si-H_3 (2100 cm^{-1}) bonds [189].
This identification is not completely clear; a controversial discussion is still present in the literature [205,206]. In particular, theoretical works predict a finer splitting in distinct modes; nonetheless, the splitting is below the typical resolutions of FTIR measurement devices [185].
However, we decided to follow a similar pattern of [207]; we can introduce a new variable f, defined as follows:

$$f = \frac{I_{2100}}{I_{2000} + I_{2100}} \tag{5.2}$$

where I_{2100} and I_{2000} are the absorption strengths of the corresponding peaks. The increase of the ratio f is an expression of an increasing disorder in the amorphous network. An increase in the disorder can be ascribed either to an increased number of Si atoms with multiple dangling bonds possibly saturated by H atoms or to the placement and bonding of H atoms at nanovoids inner surfaces [205]. In both cases, the overall number of silicon atoms bonded to two or more hydrogen atoms (related to the peak at 2100 cm^{-1}) becomes larger, leading to an increase of f.
From Figure 5.11 a growth of f with increasing R_x can be deduced. Indeed, the 2000 cm^{-1} peak relative absorption strength (inverted blue triangles) is reduced, whereas the 2100 cm^{-1} peak (light blue diamonds) is increased as R_x rises. This behaviour is also reflected in a similar trend of f (not shown), increasing from an initial value of 0.28 for the reference sample to a value of 0.93 for N16.6 sample and of 0.72 for C9.1 sample, respectively. This discussion leads to the following result: the Si-H_2 bond density increases in the layers with higher values of R_x dilution, promoting the formation of progressively higher-disordered layers.
Furthermore, the two absorption peaks at 840 cm^{-1} and 890 cm^{-1} are considered as a doublet, generated from the interactions of two Si-H_2 groups. They typically appear for hydrogen concentrations large enough that the distance of such two groups becomes comparably small [185]. The peak at 840 cm^{-1} is

weak for low H concentrations, but it becomes more intense than the 890 cm^{-1} peak as the Si–H_2 bond density grows.
This effect can be clearly observed in both sample sets in Figure 5.11. The relative absorption strength of the 840 cm^{-1} peak (red circles) has an increasing trend with growing R_x (up to 3.5 times), whereas the relative absorption strength of the 890 cm^{-1} peak (blue triangles) decreases at the same time (up to one-third of the a-Si:H value). However, if we relate this last result to an enhancement of hydrogen concentration as R_x increases, it would be in contrast with the conclusion found from the 640 cm^{-1} peak, where a decreasing trend of hydrogen incorporation has been derived with increasing gas dilutions. Then, the increasing interaction between Si-H_2 bonds with higher R_x should be considered an effect of the higher Si–H_2 bond density; in addition, this result agrees with the previous discussion on the increasing trend of f.
In summary, the FTIR analysis revealed a general similarity between the N and C sample sets in terms of an increasing disorder of the amorphous network with increasing flux ratios R_x; in detail, increased Si–H_2 and Si–H_3 bond densities are revealed, as well as a probable formation of nanovoids.

5.2.2. Spectral ellipsometry

The spectral ellipsometry data have been fitted with the model described in Section 3.5.1; in this way, we can determine variations of the optical constants within the samples layers. In Figure 5.12 each one of the 21 sublayers refractive index extracted from the fitted model is represented by a single data point (the refractive index is at 600 nm wavelength).
A refractive index reduction close to the c-Si substrate is visible for all the samples. For this reason, we distinguish between a refractive index close to the interface and a “steady-state” refractive index far from the interface. Considering the reference sample (black squares), the refractive index is approximately constant over the whole range of the layer, except for the first sublayer at the interface to the substrate.
The reduction of the refractive index close to the interface with the substrate broadens even to few sublayers from the interface for larger R_x flux ratios. The decrease in the refractive index at the substrate interface can be attributed to the formation of a less dense microstructure [208]. Hence, an island growth can occur in the initial part of the deposition, when the growth has not reached its steady state condition. Following this explanation, the amorphous network density at the interface with the substrate decreases with increasing R_x, probably accompanied by nanovoid formation.

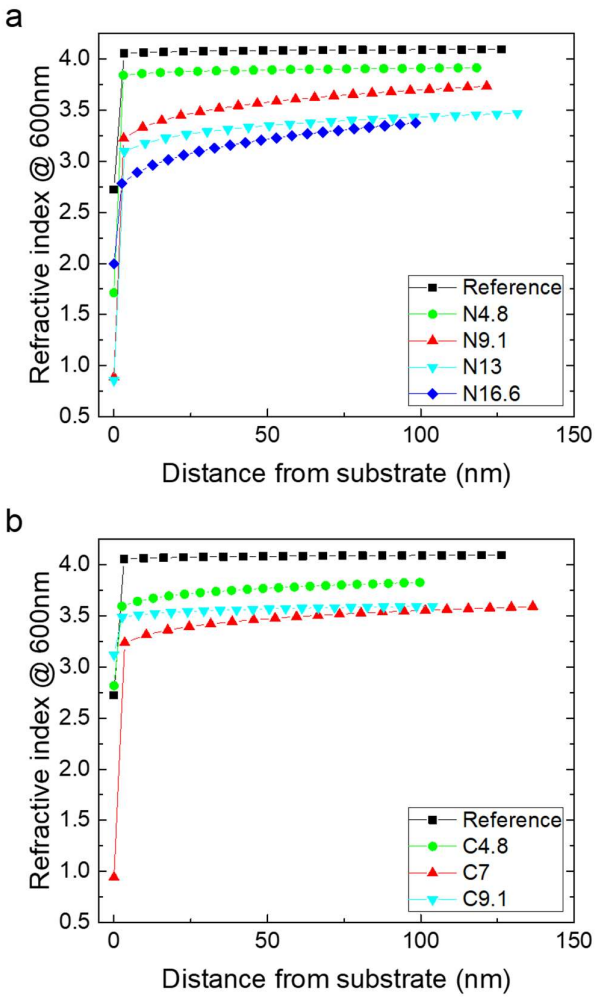

Figure 5.12 Refractive index variation as function of the distance from the substrate for a) the N sample set and b) the C sample set. Each data point represents the refractive index (at 600 nm) in one of the 21 sublayers considered in the fitting process.

Considering the steady-state refractive indices, they lie in a range from 3 to 4 for the a-SiO_xN_y samples, whereas for a-SiO_x samples a shorter range from 3.3 to 4 occurs. To make a comparison, stoichiometric silicon oxide (SiO_2) has typically a refractive index of around $n_{SiO2} = 1.5$ and stoichiometric silicon nitride (Si_3N_4) of around $n_{Si3N4} = 2.0$ (all the values are extracted at a wavelength of 600 nm) [209]. All the measured refractive indices are quite close to the pure a-Si:H refractive index (roughly 4.0) and we can conclude that each layer of both sample sets should be considered strongly sub-stoichiometric.

Moreover, the steady-state refractive index shows a decreasing trend with increasing R_{N2O} in the N sample set, as shown in Figure 5.12a. This behaviour is explainable with an increasing oxygen content within the layers with increasing N_2O dilution, in accordance with the FTIR results (Section 5.2.1). Indeed, the refractive index tends towards lower values, closer to SiO_2 refractive index. On the contrary, the trend is not that clear for the C sample set, as a similar trend to the N set was expected. Indeed, sample C7 shows an anomalous lower "steady-state" refractive index than sample C9.1; in addition, a much stronger reduction of the refractive index in the sublayer at the interface occurs with respect to the other C samples. A similar deviation is present in the FTIR absorption peak of interstitial oxygen at 1107 cm^{-1} (see Figure 5.10), where the corresponding relative absorption strength of the sample C7 is increased by a factor of two compared to the other C samples. This increase is not present in the other two oxygen absorption peaks. These considerations suggest an increased amount of interstitial oxygen. The increasing interstitial oxygen content can be associated with the formation of more or larger nanovoids, which offer more space for interstitial oxygen accommodation. This double effect can explain the reduction of both the steady-state refractive index and the refractive index at the interface. Somehow, the growth of sample C7 differed from all the other depositions.
Comparing the N and C sample sets, a stronger reduction of the steady-state refractive index for the set N occurs with higher R_{N2O}. This difference is quite unexpected, since the flux ratios were chosen to approximately match the total number of oxygen atoms inside the PECVD plasma, hence, to have a comparable amount of oxygen available during deposition.
However, an explanation has been found in [210]: the refractive index is a mostly linear function of the silicon concentration. From this observation it is now clear why the refractive index of the a-SiO_xN_y samples is lower than the one of the a-SiO_x layers. In the a-SiO_xN_y layers, the silicon concentration is reduced by the additional nitrogen, whereas no such significant carbon incorporation occurs in the a-SiO_x layers (see Section 3.1).
In summary, an expected reduction of the steady-state refractive index with increasing R_x occurs due to a lower silicon concentration within the layers. In addition, a reduction of the refractive index at the interface is present, suggesting a less dense microstructure, probably supplemented by nanovoid formation. In conclusion, the amorphous network is less ordered with increasing R_x, in agreement with the results of the FTIR discussion in Section 5.2.1. The observed reduction of the refractive index is also related to a reduction of the

extinction coefficient for wavelengths less than 500 nm, which consequently reduces parasitic absorption compared to a pure a-Si:H standard SHJ cell, making these layers more feasible for the application.

5.2.3. SPV spectroscopy

Figure 5.13 shows the SPV spectra of the N (a) and C (b) sample sets acquired with the QTH lamp (see Section 4.1.1). Both sets are compared with the a-Si:H reference sample. A slight slope change at around 1.05–1.09 eV is visible in the spectra of the samples deposited at higher flux ratios (N9.1, N13, N16.6, C9.1), which is related to the band-to-band transition in the c-Si substrate (transition (1) in Figure 2.4). In the spectral range of the QTH lamp, the light penetration depth, which equals the inverse of the absorption coefficient, is comparable with the whole sample thickness [211]; therefore, the top layer turns out to be transparent and the interface with the c-Si substrate is observable.

Above the c-Si band gap, none of the samples show a decrease in the SPV signal; this effect indicates a low interface recombination, similar to the as-deposited sample in Figure 2.4 (for the details, see the discussion in Section 3.4.3). The low interface recombination velocity is an indicator of a good passivation of the layer.

The layers deposited at lower flux ratios R_x (N4.8, C4.8, C7 and the reference) exhibit a small signal variation above the c-Si band gap. This effect can be justified by a low efficiency of the interface potential in separating photogenerated carriers. Indeed, visible SPV signal requires both photon absorption and a net carrier separation by an electric field. The interface potential can be weaker for the layers deposited with lower flux ratios because the band gap discontinuity from the c-Si substrate and the top layer is too small to create an efficient heterojunction capable to separate carriers. In particular, this consideration is quite valid for the pure a-Si:H sample. Although the optical properties of our layers are very similar to the a-Si:H layer (see the refractive index in Figure 5.12), the electrical properties and their interface with the Si substrate strongly differ from it.

Unexpectedly, even sample C7 shows an inefficient charge separation, showing a lower variation than sample C4.8, which indicates a reduced electric field at the interface. However, a deviation from the expected trend for the sample C7 was also found in the FTIR and spectral ellipsometry results in Sections 5.2.1 and 5.2.2. Then, all the results are in agreement with the altered behaviour of sample C7.

Figure 5.15 shows SPV spectra of both sample sets acquired with the Xe lamp. Due to the higher photon energy range, the light penetration depth is smaller than in the previous case. Thus, the photoinduced charges are separated mainly by the top layer surface potential and the features of the spectra can be related mostly to transitions in the top layer.

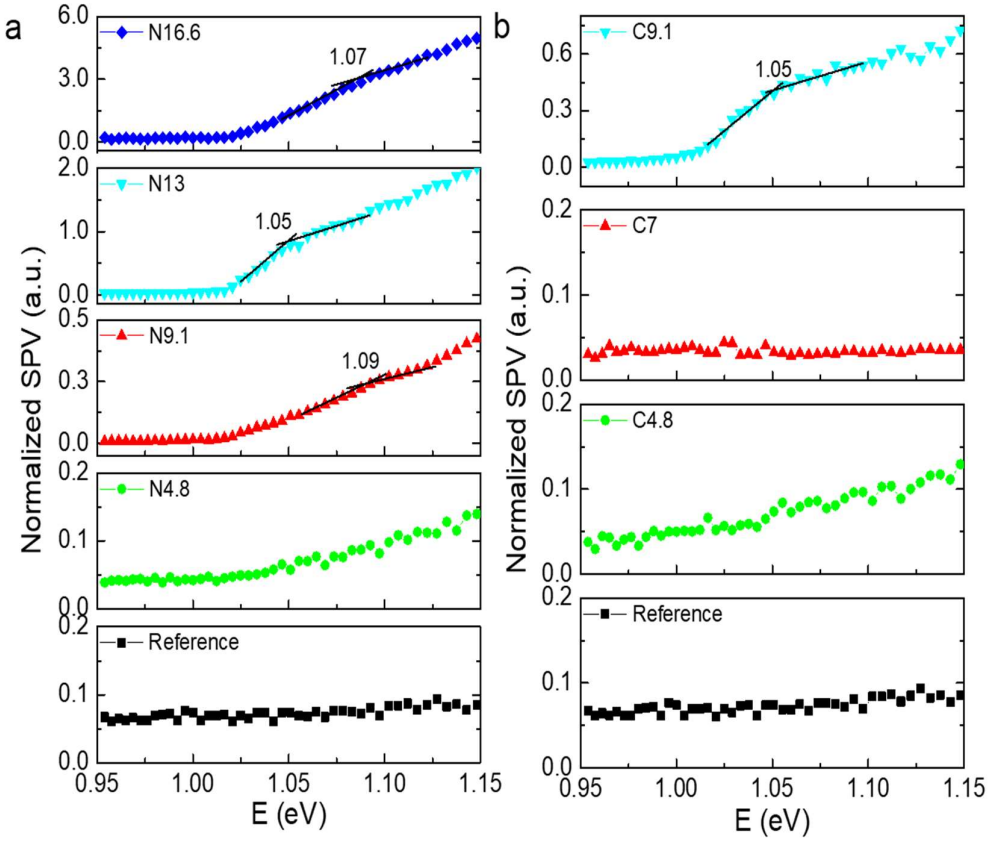

Figure 5.13 SPV spectra measured with QTH lamp of a) the N sample set and b) the C sample set. The energies of the relevant features, determined as slope changes in the curves, are marked in the spectra (the numbers refer to eV).

Again, for the reference sample no slope change is observable; probably, a high surface passivation is present, and it prevents the surface potential from effectively separating the carriers.

For the layers deposited at lower R_x, three slope changes occur in the spectra at 1.65–1.73 eV (N4.8, C4.8, C7), at 1.88–1.94 eV (N4.8, N9.1, C4.8) and at 2.31–2.32 eV (N4.8, C4.8, C7). All three slope changes in the SPV spectra can be related to the transitions highlighted in Figure 2.4: the transition from the c-Si valence band to the top layer conduction band (transition (2)), to the

transition from the top layer valence band to the c-Si conduction band (transition (3)) and to the band-to-band transition in the top layer (transition (4)), respectively. For sake of clarity, we report again Figure 2.4.

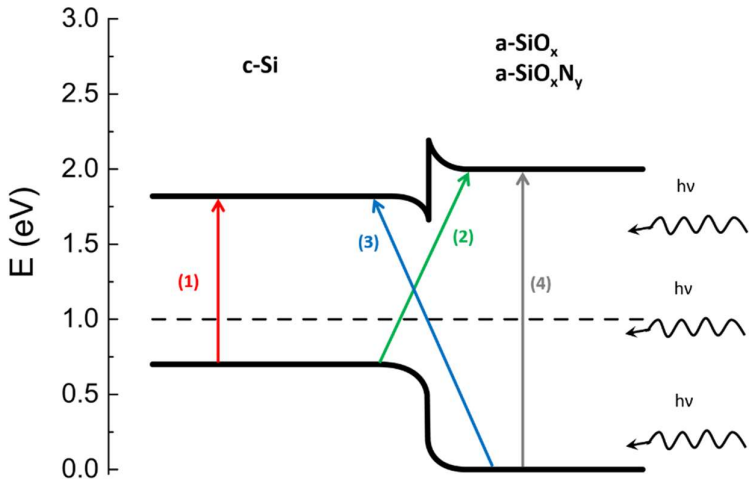

Figure 5.14 Sketch of the band diagram of a-SiO_x and a-SiO_xN_y layers (right) at the interface with the c-Si substrate (left). The possible electronic transitions under illumination are highlighted with numbers and arrows of different colours. A 2-eV bandgap for the top layer has been considered.

Following these observations, the effective optical energy gap of the a-SiO_xN_y and a-SiO_x layers is determined to range from 2.30 to 2.32 eV; these values are in agreement with previous studies [18,19,30,212] and larger than the energy gap of pure a-Si:H (1.8–1.9 eV), as expected.
For the layers deposited at higher R_x values (N13, N16.6, C9.1), one would expect a widening of the optical gap due to an increased oxygen and nitrogen concentration, and a consequent shift of the slope change to larger values than 2.3 eV. However, this expectation could not be verified since none of the three transitions was observable in those samples' spectra. This absence can be justified by the larger disorder of the amorphous network, as it was observed by the FTIR (Section 5.2.1) and spectral ellipsometry (Section 5.2.2) analyses. Indeed, as it is known, a huge disorder induces the formation of large tail states in the band gap, eventually producing a significant broadening of the whole spectrum [146].

Beside the observed transitions, a strong signal decrease above the energy gap of the top layer can be observed in all samples apart from the reference; the drop is likely related to electron-hole recombination at the top layer surface (see Section 3.4.3) [146]. Additionally, in the spectra of N9.1 and N13 samples, a further increase of the SPV signal at photon energies larger than 3 eV can be observed. This new feature might be produced by a band-to-band transition in a silicon nitride cluster phase, whose energy gap is supposed to be at around 3.2 eV [213,214]. This effect is not visible for the sample N16.6, since the broadening of the spectrum covers eventual features, as discussed above.

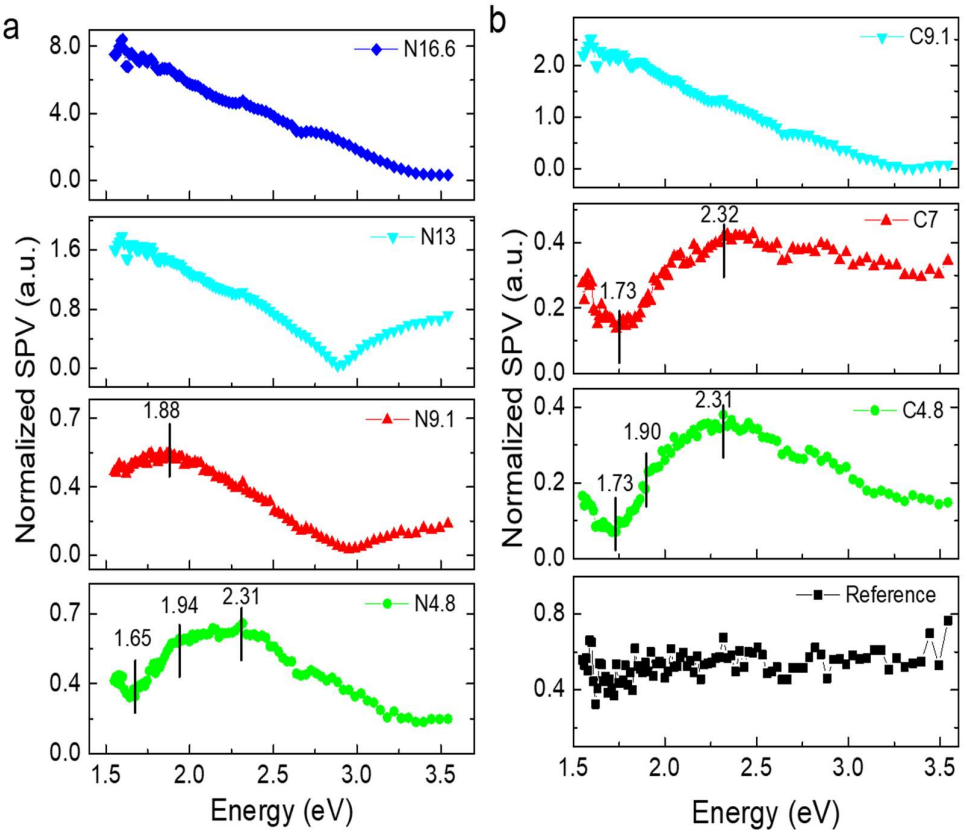

Figure 5.15 SPV spectra measured with Xe lamp of a) the N sample set and b) the C sample set. The energies of the relevant features, determined as slope changes in the curves, are marked in the spectra (the numbers refer to eV) [190].

The SPV technique has allowed us to extract two spectra in two distinct spectral ranges; from this investigation, the energy gap of the a-SiO_xN_y and SiO_x layers deposited at low flux ratios has been estimated at roughly 2.3 eV. Furthermore, the determination of the main electronic transition energy

positions and the passivation quality of the interfaces and surfaces has been achieved.

5.2.4. Passivation quality by lifetime measurements

The effective minority carrier lifetimes were determined using ac-SPV (Equation (3.14) in Section 3.4.4) as well as PCD. The ac-SPV chopper frequency variation was selected at the photon energy of 2.3 eV, corresponding approximately to the top layer energy gap determined in the previous section. Typically, effective minority carrier lifetimes measured by PCD are much smaller than the ones measured by ac-SPV. This difference occurs due to the surface recombination velocity, which influences the lifetime values evaluated by PCD more than the ones obtained by ac-SPV [215]. Indeed, the lifetime acquired by PCD is an effective lifetime that takes into account both the bulk and the surface lifetimes.

Regarding the type of passivation, the authors in [216] have built a model to distinguish between chemical passivation, due to the reduction of interface density of dangling bonds, and a field effect passivation, due to charged defects. Following this model, both chemical passivation through saturation of dangling bonds with hydrogen and a field effect caused by the band offset between crystalline and amorphous silicon are present in a-Si:H layers. Then, in the following results, we refer to passivation as a combination of both effects, since the applied techniques do not allow any separation of the contributions.

The lifetime values τ calculated from both techniques are reported in Figure 5.15. The PCD measured lifetimes vary in the range of 1.4–2.9 ms, while the ac-SPV measured lifetimes vary in the range of 0.6–9.0 ms. The differences in the values extracted by the two techniques follow the expected behaviour (*i.e.* $\tau_{PCD} < \tau_{ac-SPV}$) only for the samples with lower R_x values, whereas a reverse behaviour is present for the samples with higher R_x values. This anomaly can be explained considering that the ac-SPV lifetime values may also be affected by interface recombination, which is quite strong in the samples with higher R_x.

Both techniques show a similar overall trend: a reduction in passivation quality with increasing R_x (Figure 5.16). The result is in good agreement with the FTIR and spectral ellipsometry results, as they both showed an increase of disorder within the amorphous network with increasing gas dilution (Section 5.2.1 and Section 5.2.2). However, some differences are present between the two sample sets, as well as between the two investigation techniques; thus, a clarification is required.

At first, the lack of a clear decreasing trend for the C sample set is related again to an anomalous value for sample C7 for the PCD measurements. Indeed, sample C7 shows a PCD lifetime of 1.5 ms, which is unexpectedly low compared to 2.2 ms for the sample C9.1.

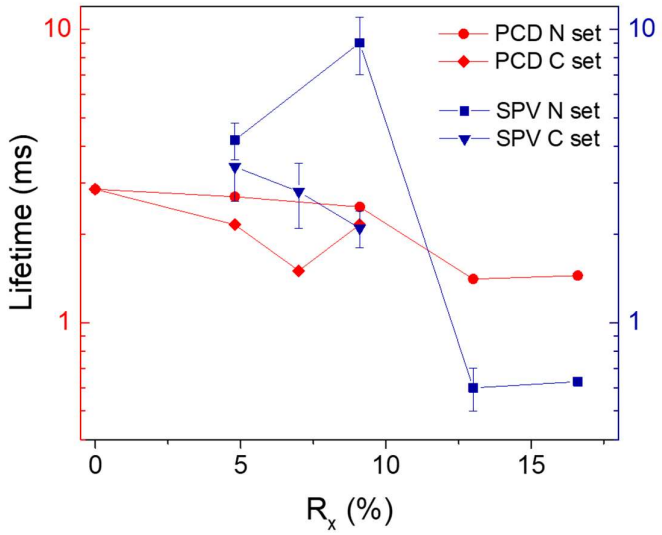

Figure 5.16 Effective minority carrier lifetimes measured by PCD and ac-SPV of the N and C sample sets, plotted as a function of the gas flux ratio.

In the FTIR and spectral ellipsometry analyses (Sections 5.2.1 and 5.2.2), a deviation from the expected trend in C7 sample was found and related to a large content of interstitial oxygen and defects in the amorphous network at the interface.
Thus, the low PCD lifetime of this sample can be explained by a larger interface recombination. It should be mentioned that a deviation from a clear trend is not observable in the ac-SPV measured lifetimes. On the contrary, a similar trend using the two techniques occurs for the N sample set.
A significant drop in the lifetime in the samples with R_{N2O} values larger than 9.1% occurs; this result suggests the employment of such layers in SHJ cells only within a range of $R_x < 9.1\%$. In detail, the lifetime values drop from 2.4 ms to 1.4 ms for the PCD measurements and even stronger from 9.0 ms to 0.6 ms for the ac-SPV measured lifetimes. A little deviation from the trend occurs for the sample N13, although it is not supported by the investigation by spectral ellipsometry. However, the drop in lifetime is present for both

measurement techniques, thus it cannot be completely attributed to a defective network at the interface.
Instead, the reason for this drop can be found in the FTIR results: from the relative absorption spectra of Si-N bond in Figure 5.10a, the nitrogen content of sample N13 turns out to be larger than sample N16.6. FTIR absorption spectra contain information of the whole layer. Supposing the larger nitrogen content homogeneously distributed, this discussion might explain why the ac-SPV measured lifetime is also affected.
Additionally, the ac-SPV measured lifetime of the sample N9.1 is anomalously high with a value of 9.0 ms, more than twice the value of the sample N4.8 with 4.2 ms. This deviation must be an effect of the ac-SPV measurement technique, since no deviation from the trend was measured using PCD.
The total reduction in lifetime with increasing R_x is stronger for the N sample set compared to the C sample set, although we chose the flux ratios to approximately match the oxygen atoms availability inside the PECVD plasma. As already discussed in the ellipsometry results, we can conclude that, beside the oxygen content, the additional nitrogen content in the a-SiO_xN_y layers causes an increased amorphous network disorder responsible for a stronger lifetime reduction.

5.3 Results on $LaVO_3$ structures

All the $LaVO_3$ samples and $LaVO_3$/ZnO structures (see Table 2.4) have been analysed using both AFM and KPFM techniques to determine the changes of the layer surface properties, to evaluate the $LaVO_3$ work function and the barrier height at the $LaVO_3$/ZnO interface, mandatory for a further operative solar cell production.

5.3.1. AFM results

The LaVO3 samples listed in Table 2.4 differ for substrate, deposition technique or thickness. Sample LVO55Q has been used as a reference for comparing the other samples. Indeed, the other samples differ from it only in one parameter. In this way the influence of a single parameter on surface morphology can be easily identified and understood. LVO55Q AFM maps of different sizes are reported in Figure 5.17a,b. Both maps present several areas separated by grain boundaries; this structure simulates the one of the quartz substrate, which is known to have a very pleated surface. Moreover, ring-like structures of 100-200 nm diameter are present.

LVO55S maps of different sizes are reported in Figure 5.18a,b. Comparing the height ranges of the map, a roughness decrease of one order of magnitude is evident with respect to the sample deposited on quartz; in addition, grain boundaries disappear. Both the effects are related to the different substrate; indeed, Si has a very flat surface compared to quartz, and this reflects on the top layers surface [88]. However, ring-like structures with a hole of 5-10 nm of depth are still present (clearly visible in the extracted profile reported in Figure 5.18c). Since the deposition technique is the same for both samples, these ring-like defects are probably caused by molecular impact during sputtering. It is likely that these structures may be reduced or even avoided by further lowering the deposition power [88].

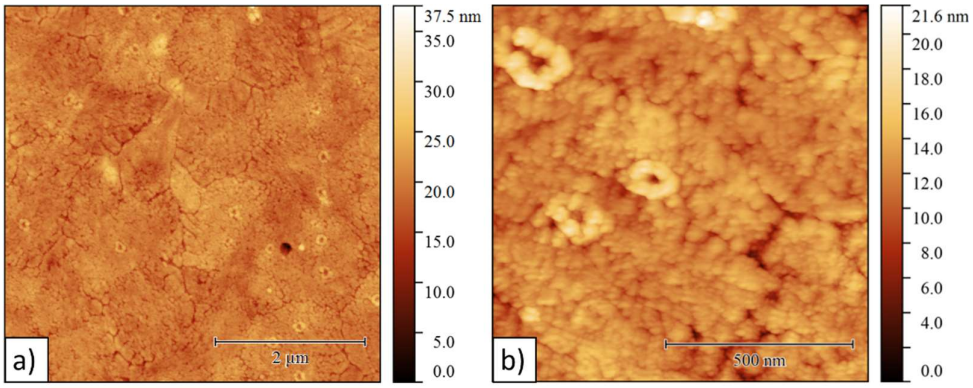

Figure 5.17 Surface morphology of LVO55Q: 55 nm $LaVO_3$ on quartz deposited by sputtering. The scan area is a) 5×5 μm^2 and b) 1×1 μm^2, respectively. Also reported in [88].

LVOsg36Q maps in Figure 5.19 also show a less emphasised roughness decrease with respect to the LVO55Q sample, but grain boundaries are still visible. This result is a double check to prove the certain correlation between the grain boundaries and the quartz substrate. Ring-like structures disappear in the sample deposited by sol-gel, confirming that their existence is related to the sputtering technique [88].
Since the ZLVO100Q and ZLVO130Q samples have very similar features as far as structure, substrate and deposition techniques, the surface morphology of the two samples is approximately the same. Moreover, the maps acquired on sample ZLVO130Q showed more stable signals and better reproducibility. For both these reasons, only for one sample (ZLVO130Q) maps of different sizes have been reported in Figure 5.20a,b.

In ZLVO130Q maps the roughness increases with respect to the LVO55Q sample; moreover, grain boundaries disappear with higher thicknesses. The ring-like structures are still present, due to their link to the sputtering technique; but they show smaller depth and diffusion [88].
The same structure characterizes both $LaVO_3$ and ZnO sides. With larger deposition time (to obtain greater thicknesses) the atoms have the chance to migrate and rearrange on the surface, partially filling up the holes and covering the grain boundaries. In this way a more homogeneous but rougher surface is obtained in the thicker samples (ZLVO100-130Q).

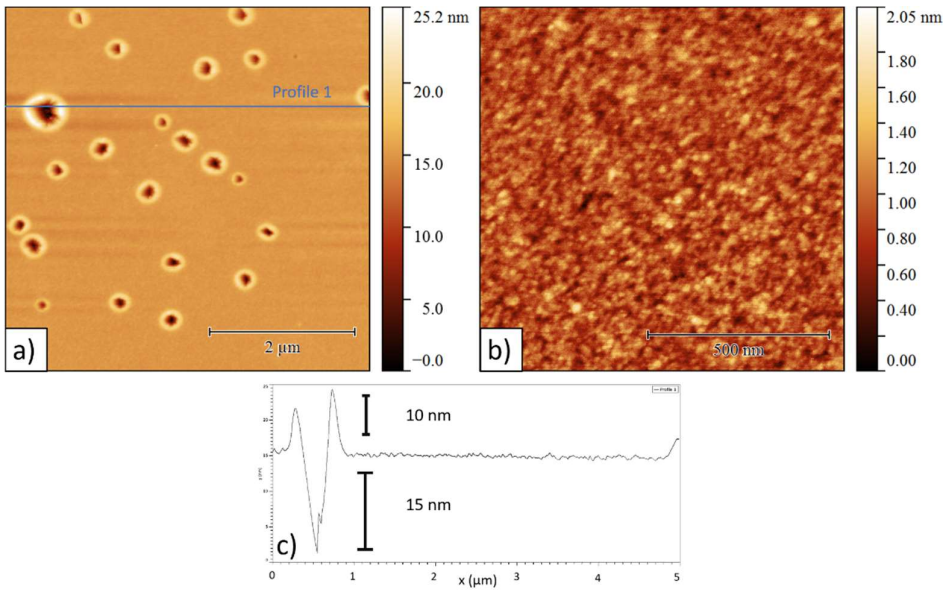

Figure 5.18 Surface morphology of LVO55S: 55 nm $LaVO_3$ on Si deposited by sputtering. The scan area is a) 5×5 μm^2 and b) 1×1 μm^2, respectively. The smallest map has been acquired on a surface part with no ring-like structures. c) Profile height of the light blue line indicated in the map a), with an esteem of hole dimensions. Also reported in [88].

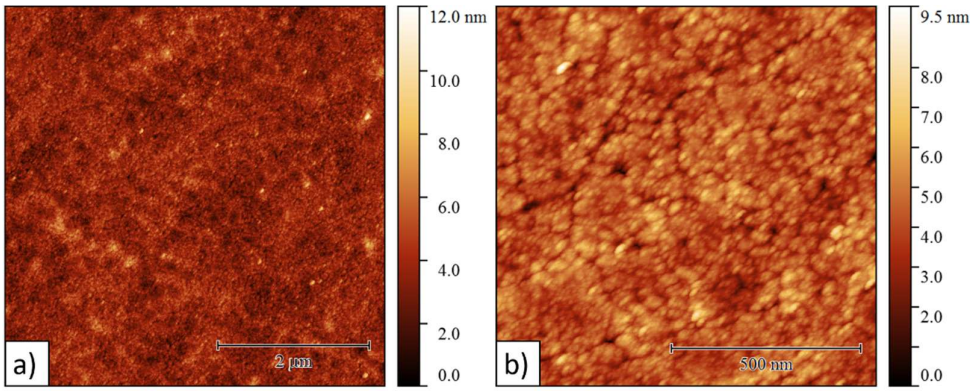

Figure 5.19 Surface morphology of LVOsg36Q: 36 nm $LaVO_3$ on quartz deposited by sol-gel. The scan area is a) 5×5 μm^2 and 1×1 μm^2, respectively. Also reported in [88].

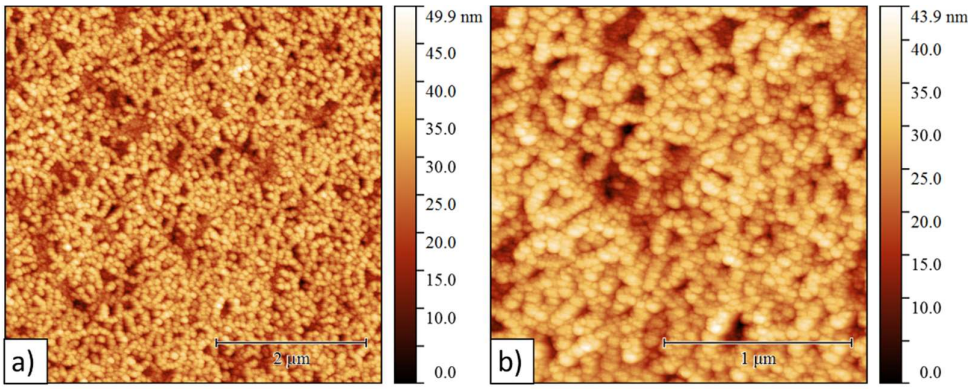

Figure 5.20 Surface morphology of ZLVO130Q: ZnO (100 nm) // $LaVO_3$ (130 nm) // quartz architecture deposited by sputtering. The scan area is a) 5×5 μm^2 and 2×2 μm^2, respectively. Also reported in [88].

By the software Gwyddion an RMS roughness could be extracted for all the samples (see Section 4.3 for the details). We focused in the areas without the big ring-like structures in LVO55S sample. All the RMS values are reported in [88].

Label	Substrate	Technique	Thickness (nm)	RMS (nm)
LVO55Q	quartz	sputtering	55	2.7±0.5
LVO55S	silicon	sputtering	55	0.20±0.02
LVOsg36Q	quartz	sol-gel	36	0.9±0.1
ZLVO130Q	quartz	sol-gel	130	5±1

Table 5.2 RMS roughness values of all the investigated samples, measured in zones without deep ring-like structures. Also reported in [88].

The results on the AFM morphological analysis on $LaVO_3$ samples can be summarized as follows [88].

- The presence of ring-like features can be correlated to the sputtering deposition, since they occur in samples with different substrates deposited by sputtering and they disappear when the sol-gel technique is used.
- The ring-like features change in dimensions and number with the thickness of the layer. Higher deposition times seem to promote atom migration, creating a rougher and more homogeneous surface. The power of 130 W is too high to prevent the formation of these rings.
- Thinner layers deposited on quartz show several grain boundaries related to the high roughness of the quartz substrate. The features disappear as the layer thickness is increased.

5.3.2.KPFM results

EFM and KPFM maps have been acquired on sample ZLVO130Q to investigate the surface and interface electrical properties of the structure at the nanoscale. EFM and KPFM techniques have been described in Section 3.3. They differ in the detection of the signal. Indeed, in EFM maps the bare tip-sample electrostatic potential is mapped; in this case, the signal could be correlated to the morphology of the surface. Conversely, a feedback signal is used to cancel out the measured surface potential and the bias applied to the feedback loop is then recorded in KPFM maps. In this way, the KPFM allows for the determination of the contact potential difference V_{CPD} defined in Equation (3.2).
In Figure 5.21a,b,c, 30×30 μm^2 maps of the area between $LaVO_3$ and ZnO in sample ZLVO130Q are reported. The topography map in Figure 5.21a shows a depression at the edge between the two layers. This feature is likely due to the feedback-based acquisition of constant force mode. Indeed, a huge 100 nm

step should be expected at the border, due to the difference in height of the ZnO- and $LaVO_3$-areas (see Figure 2.5 for the sample structure). In addition, the morphology is similar on both sides, as already seen from the topography maps analysis in the previous section. On the contrary, from EFM and KPFM images in Figure 5.21b,c, a clear difference between the two materials is visible. The average values of the measured potentials from both EFM and KPFM maps and the extracted $LaVO_3$ and ZnO work functions are here reported in Table 5.3.

	$LaVO_3$	ZnO
EFM (electrostatic potential) (V)	$(0.10\pm0.05)\cdot10^{-3}$	$(1.88\pm0.04)\cdot10^{-3}$
KPFM (V_{CPD}) (V)	0.175±0.005	0.300±0.005
ϕ calculated value (eV)	4.625±0.005	4.500±0.005

Table 5.3 EFM and KPFM potential average values and calculated work functions for $LaVO_3$ and ZnO. Reported also in [88].

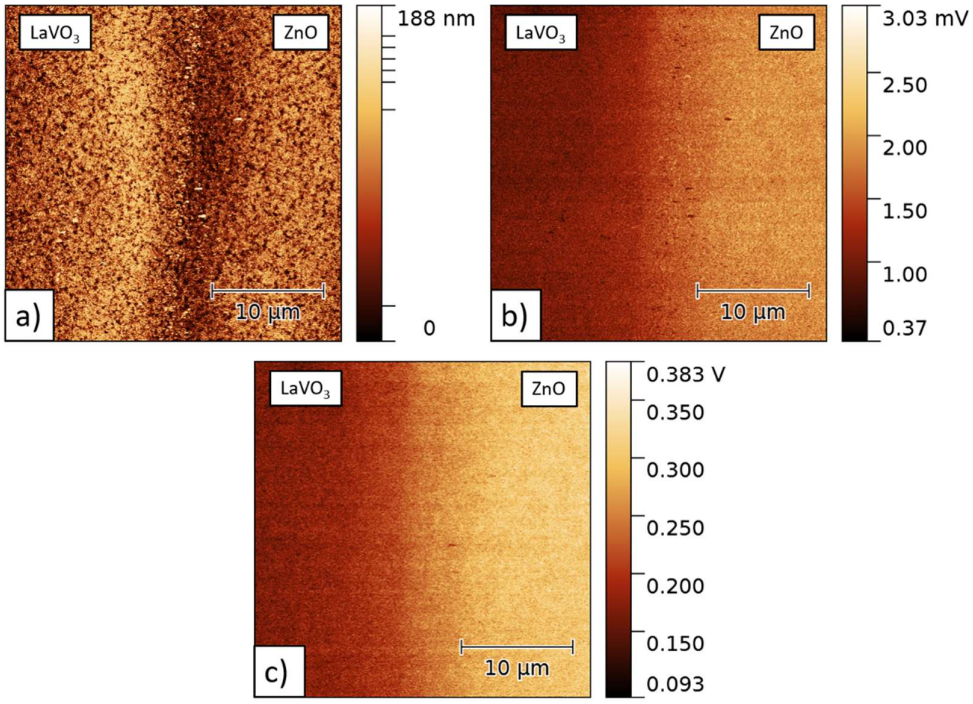

Figure 5.21 a) Topography, b) EFM and c) KPFM maps of ZLVO130Q sample at the edge between $LaVO_3$ and ZnO. The scan area is 30×30 μm^2. $LaVO_3$ is on the left side and ZnO on the right side of the map. Also reported in [88].

KPFM maps are pretty much unaffected by morphology, and a reliable average value of V_{CPD} can then be extracted. This process allows for the evaluation of the work function ϕ for both materials. As the tip is made of gold, with $\phi_{Au} = 4.8$ eV as listed in [157], the work function values of $LaVO_3$ and ZnO have been extracted and reported in Table 5.3. Since the result for ZnO well agrees with literature values, spanning from 3.7 to 6.0 eV depending on the surface orientation and deposition methods [217], the result for $LaVO_3$ can be considered reliable as well. It is noteworthy that the measured value of the $LaVO_3$ work function has never been reported in literature up to now [50]. Moreover, the barrier height value of $ZnO/LaVO_3$ could be extracted as well, and it is equal to 0.125 V. Current-voltage characteristics reported in Figure 2.6b showed a built-in potential around 0.1 eV, which is in very good agreement with the KPFM results [50]. Some attempts of measurements by SPV technique (see Section 3.4) have been done on the sample junction as well, but no signal was detected [50,88]. Anyway, the impossibility of an SPV signal extraction can be explained through the results on the barrier height of the junction. Indeed, the low value of the built-in potential indicates an ineffective separation of the photogenerated carriers and thus no collection is possible [50]. This behaviour explains also why the I-V characteristics (Figure 2.6b) in light and dark almost overlap: the free carriers are not efficiently separated and collected [50].

Thereafter, a more enlarged map of 2×2 μm^2 has been acquired only on the $LaVO_3$ side to investigate the surface potential variations at the nanoscale. It is reported in Figure 5.22a,b,c. The EFM signal in Figure 5.22b is deeply correlated to morphology, as expected. However, the KPFM map in Figure 5.22c shows tiny variations, probably due only to noise effects. Indeed, the grains reported in topography maps do not show appreciable variations in the surface potential, within the sensitivity of the method.

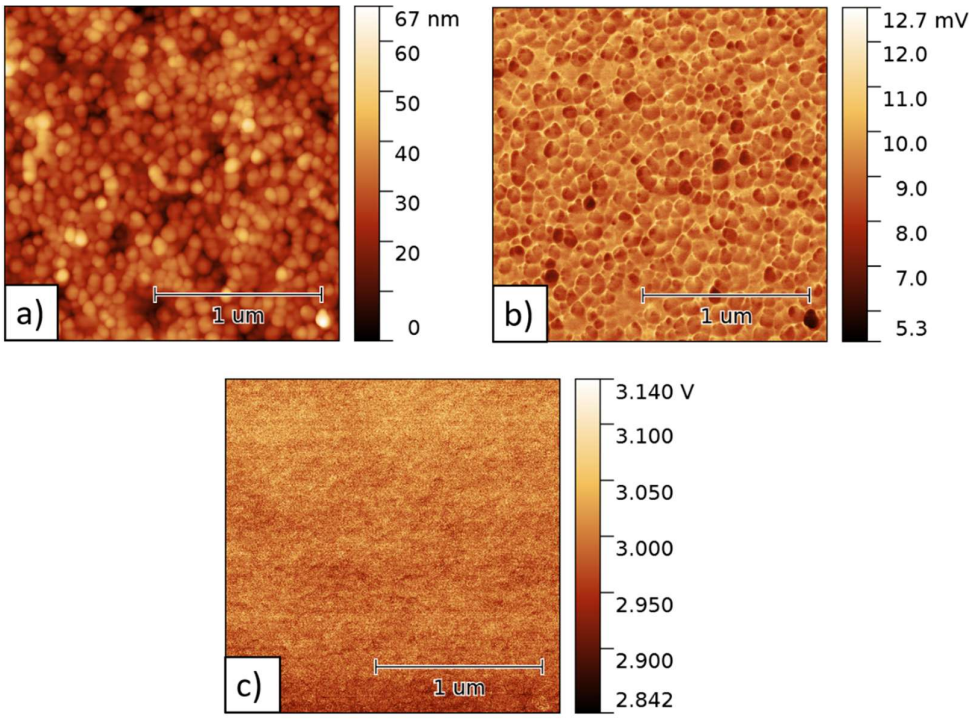

Figure 5.22 a) Topography, b) EFM, c) KPFM maps of sample ZLVO130Q on $LaVO_3$ side (scan area 30×30 μm^2). Reported also in [88].

5.4 Results on $In_xGa_{1-x}N$/GaN structures

Si doped $In_xGa_{1-x}N$/GaN samples, reported in Table 2.6, have been investigated by SPV technique. The spectra have been acquired both from the front side and the back side of the samples (see insets of Figure 5.23a,c), so that the incident light hits InGaN and sapphire layers, respectively. In Figure 5.23a, all the sample spectra with the photon beam impinging over the sample from the front side are reported. As already mentioned in Section 3.4.1, the most relevant features in an SPV spectrum occur at the energy corresponding to the band gap of the investigated materials. Indeed, the spectra in Figure 5.23a present an increase of the signal in two different regions, corresponding to the InGaN and GaN energy gaps at lower and higher energies, respectively. These spectra show the capacity of the technique to "see" also at buried layers and interfaces, if the top layer is transparent in the right energy range. It should be noticed from the spectra that InGaN bandgap occurs at different energies ranging approximately from 2.6 to 2.9 eV depending on the In content within the layers; whereas the GaN peak always occurs at 3.4 eV. In Figure 5.23b, our results for the InGaN bandgaps are shown as pink stars, compared with

different previously reported results and theoretical calculations with different bowing parameters (see Section 1.4 for definitions). All the references are reported elsewhere [90]. It should be noticed that no strain correction has been performed for the band gap evaluation, since the materials can be considered fully relaxed, due to the presence of misfit dislocations. The band gap values result to be in agreement mostly with the theoretical results which consider the bowing parameter $b = 1$. Better focusing on the spectral regions between the two energy bandgaps in Figure 5.23a, one can notice that there is a drop of the signal with an increasing depth from low to high Si doping. Generally, as shown also in Section 3.4.3, a decrease of the signal at higher energies is related to an interface recombination effect. In this sample set, high Si doping corresponds to a higher interface recombination, due to an increased dip in the spectra, as well as a lower SPV signal. In other words, good quality interfaces belong to samples with a combination of lower In content and lower Si doping. Moreover, both indium content and silicon doping affect the steepness of the InGaN peak. An ideal peak should be a step function that rises precisely at the energy of the bandgap. In real spectra the signal increases more gradually with a certain slope. As already mentioned in Section 3.4.1, this slope can be attributed to the formation of Urbach tails due to a disordered structure. In Figure 5.23a, it is visible that the slope decreases as both Si doping and In content increase; indeed, the increment of both element concentration creates more defects and disorder, leading to more pronounced Urbach tails. A correlation between In content and disorder has already been shown in [218]. The spectra acquired from the back side are reported in Figure 5.23. In these spectra, only the GaN peak is visible, whereas InGaN peak is not visible anymore. The GaN layer is too thick to allow light reaching the InGaN/GaN interface.

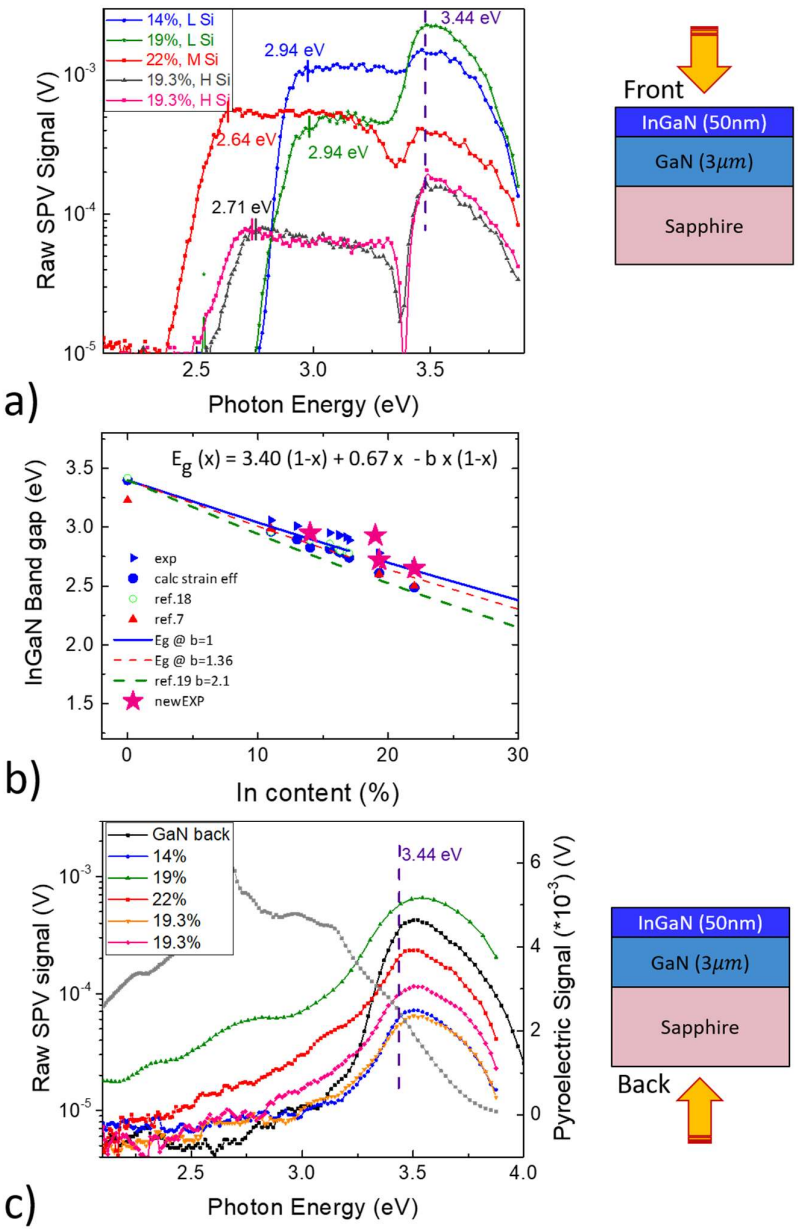

Figure 5.23 SPV spectra acquired by Xe lamp of Si doped $In_xGa_{1-x}N$/GaN samples (see Table 2.6) from a) front and c) back of the structure. In c) the lamp photon flux is also reported in grey squares. b) Calculated energy gap values of InGaN layers for different bowing parameters (lines) and our new results (pink stars) compared with earlier results in references reported in [90].

Undoped $In_xGa_{1-x}N$/GaN samples, reported in Table 2.7, have been investigated by SPV technique. The normalised spectra acquired with the Xe lamp are reported in Figure 5.24a for both samples. The signal increases in both the spectra at the GaN and InGaN bandgaps. As expected, the InGaN peak occurs at different energies (2.7 eV for sample L571 and 2.85 eV for sample L605), since it depends on the In content within the layers (see Section 1.4), while the GaN peak occurs at 3.4 eV. However, the signals appear quite different in the transition range between the two gaps, which corresponds to the crossing of the interface. Indeed, a dip occurs in the sample L571 at around 3.3 eV. The dip could be related to recombination processes at the interface; MDs generate a strong recombination at the InGaN/GaN interface. The signal drop in this region does not occur in the sample without MDs (L605). In Figure 5.24a, another feature is evident in both samples at around 2.3 eV. This feature can be related to the yellow band transition (YB) which is very common in GaN and widely reported in literature [219]. Comparing the spectra with those in Figure 5.24b acquired on a GaN buffer layer in different spots of the surface (Scan 1, 2, etc.), we can be sure that this feature belongs exclusively to the GaN substrate.

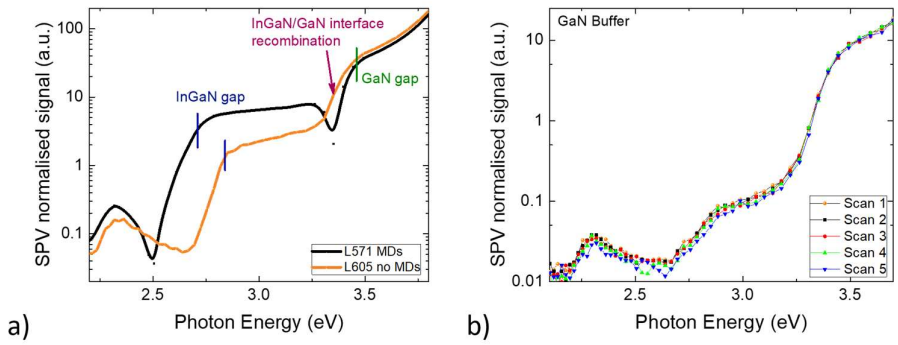

Figure 5.24 a) Normalised spectra of L571 sample (black line) and L605 sample (orange line) as a function of the photon energy. b) GaN buffer layer normalised spectra acquired in different spots of the surface.

5.5 Results on $Al_xIn_yGa_{1-x-y}N$/GaN structures

$Al_xIn_yGa_{1-x-y}N$/GaN samples, reported in Table 2.8, have been investigated by SPV technique. The spectra have been acquired from the front side of the samples, so that the incident light hits the top layer. In Figure 5.25, all the samples spectra with the photon beam impinging the sample from the front

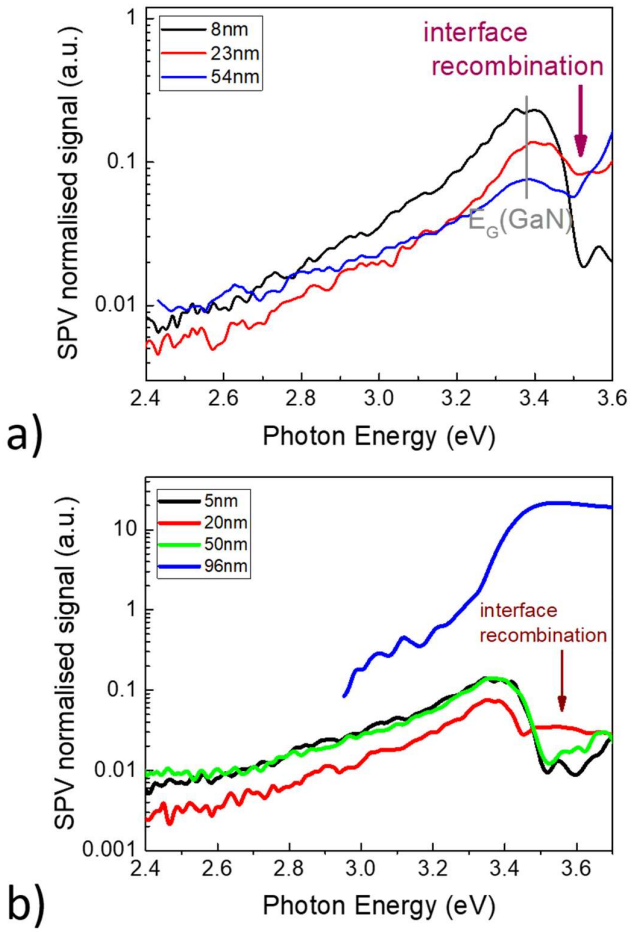

Figure 5.25 SPV normalised spectra for AlInGaN on GaN with a) compressive strain and b) with tensile strain, with different thicknesses expressed in the legend.

side are reported. As already mentioned in Section 3.4.1, the most relevant features in an SPV spectrum occur at the energy corresponding to the band gap of the investigated materials. Indeed, the spectra in Figure 5.25a,b present an increase of the signal in the region around 3.4 eV, which represents the GaN layer energy bandgap. Whereas the increase of the signal at higher energies related to the top layer cannot be investigated by Xe lamp. However, what is visible is the region in-between that corresponds to the interface between the two layers (since the AlInGaN layer is still transparent at such energies. The eventual drop of the signal in this region can be related to recombination effect at the interface. It should be reminded that as the thickness increases, the AlInGaN layers exhibit a higher relaxation of the strain

with an increased number of pinholes generated at the surface (see Section 2.5, Figure 2.13 and Figure 2.14). This effect is present in both compressed and tensile strained sample sets. It is evident from Figure 5.25a,b that there is a more pronounced decrease of the signal in this region for the thinner layers, while the drop is less visible or no present anymore (see the blue curves in both sample sets) for the thicker layers. From this analysis, one can deduce that: as AlInGaN layers increase their thickness, a strain relaxation occurs with pinholes formation and, as the material is less strained, the recombination effects at the AlInGaN/GaN interface become less dramatic.

Conclusions

Photovoltaics is a market in development due to the infinite availability of its source, its low-impact on the environment and its buildability in isolated areas. This field is led by Si-wafer based technology, with crystalline silicon solar cell new world record efficiency of 26.7% in 2017 [6].
Nowadays, the bulk electrical properties of the crystalline silicon wafers have reached such a high quality that obtaining further progresses in the device has become quite difficult. Innovative strategies such as improving the passivation quality of the layers and introducing different materials in the solar cell structure can overcome the limits in the efficiency. Apart from Si-based technology, new technologies still lack in the market due to stability issues (for example, in the case of perovskites) or low efficiencies (in the case of III-group nitride ternary alloys). In this perspective, a study of different materials appealing for photovoltaic applications can be useful to lead the research towards higher efficiencies. Indeed, the solar cell performance is strictly correlated to the structure, composition, optical and electrical properties of the materials. In this work, both innovative materials for Si based solar cells (nanocrystalline and amorphous sub-stoichiometric silicon oxy-nitride and oxide thin films, nc-SiO_xN_y, a-SiO_xN_y and a-SiO_x) and materials for newer solar cell concepts (as perovskite lanthanum-vanadium oxide, $LaVO_3$, thin films, and indium gallium nitride, $In_xGa_{1-x}N$, and aluminium indium gallium nitride, $Al_xIn_yGa_{1-x-y}N$, thin films) have been investigated to correlate different deposition conditions with their compositional, optical, electrical properties.
Here we report the conclusions of all the investigations, divided per material.

Nanocrystalline sub-stoichiometric silicon oxy-nitrides (nc-SiO_xN_y)

c-AFM investigations on nc-SiO_xN_y thin films deposited by PECVD technique, with different O and N inclusion, and different thermal treatments, showed that the presence of O and N in the matrix enhances the overall conductivity of the thin films, as they show higher conductivities at the nanoscale with respect to nc-Si:H layers. However, the presence of O and N may contrast the dopant (B in the present case), but B is active as a dopant in nc-Si:H. To achieve its activation in nc-SiO_xN_y films, low O content and a 3 hour long annealing treatment are both required. Indeed, the incorporation of nitrogen and oxygen induces an increase of disorder [19,115] and B atoms in these samples mostly passivate disorder-induced defects. For this reason, an n-type

conduction prevails. B activation does not occur in high O content nc-SiO_xN_y layers due to high disorder formation, and an O induced n-type conductivity prevails.
This study has allowed us to clarify the role of O, N, and B content, and annealing treatment on the microscopic transport properties and electronic transitions of nanocrystalline Si-based thin films for SHJ applications. O and N are beneficial because they lead to an increase of the conductivity of the layer, however they must be introduced in moderate quantity (with N_2O flux dilution less than 10%) to avoid high disorder.
More details can be found in our paper [220].

Amorphous sub-stoichiometric silicon oxides and silicon oxy-nitrides (a-SiO_x and a-SiO_xN_y)

The synergy of several characterization methods (*i.e.* FTIR, spectral ellipsometry, SPV, PCD) has allowed us to achieve several conclusions on a-SiO_x and a-SiO_xN_y thin films. The films are deposited by PECVD technique changing the N_2O and CO_2 precursor gases flux ratios (R_x).
By increasing the flux ratios R_x, the disorder of the amorphous network increases. The disorder is enhanced by larger Si–H_2 and Si–H_3 bond densities, probably accompanied and favoured by nanovoid formation, which is stronger at the interface with the substrate. SPV spectroscopy has allowed us to detect the energy gap of the layers at around 2.3 eV, which turns out larger than in a-Si:H; for this reason, these materials could exhibit a reduced parasitic light absorption. The effective minority carrier lifetimes, evaluated by two different techniques, PCD and ac-SPV, show a general decreasing trend as the flux ratio R_x increases. This result is in agreement with the degradation of the amorphous network evidenced by FTIR and spectral ellipsometry analyses.
An anomalous behaviour of one sample has been observed simultaneously with all techniques employed; in this way, we show the capabilities of these methods in the analysis of the physical processes involved in the passivation of silicon surfaces.
We conclude that the moderate insertion of O and N in a-Si:H, leads to a decrease of optical parasitic absorption, while maintaining the passivation quality of the layers. As generally those layers could also show quite good electrical properties [18,19,30], they might be successfully applied to improve SHJ solar cell efficiency.
More details can be found in our paper [190].

Inorganic perovskites ($LaVO_3$)

AFM analyses on $LaVO_3$ thin films showed how surface properties at the nanoscale change in relation to different deposition parameters, such as substrate, deposition technique and thickness. Sputtering deposition technique dramatically increases the surface roughness, due to molecular impact creating some ring-like structures. On the contrary, optimal surface properties with low roughness have been obtained for sol-gel deposition. Indeed, high surface roughness generally results in high surface recombination rate, with detrimental effects on the solar device performance [88]. By KPFM, we evaluated work functions of both $LaVO_3$ and ZnO and thus the barrier height at the interface at around 0.1 V, in good agreement with the one extracted by measured current-voltage characteristics. This low value explains why the junction cannot efficiently separate and collect the photogenerated e-h pairs, a necessary condition to obtain an efficient solar cell. In addition, besides the measurement of the $LaVO_3$/ZnO barrier height, KPFM has also allowed for the evaluation the surface potential, and thus the work functions of ZnO and $LaVO_3$. The ZnO has a 4.5 eV work function, a value in agreement with the range of values listed in literature [217]. We have found a work function for $LaVO_3$ at around 4.6 eV, which is quite large. It is noteworthy that the measured value of the work function of $LaVO_3$ has never been reported in literature up to now.

In conclusion, $LaVO_3$ is known to have optimal optical properties and high stability, considerable benefits for possible photovoltaic devices. However, all these measurements have clearly shown that this material is a poor charge-transport medium. To overcome this limitation, a solution could be the incorporation of an additional materials (electron and/or hole rich) into a structure similar to dye-sensitized solar cells, as proposed by Wang et al. in 2015 [54]. In this structure, the number of the internal interfaces between the individual solar absorber and nanostructured charge transport media is increased a lot, enabling charge separation and collection. All the previous considerations could pave the way for future developments on the optimization of $LaVO_3$ perovskite in the photovoltaic field.

More details can be found in our paper [50].

III-Nitrides thin films

Si doped $In_xGa_{1-x}N$/GaN samples grown with different In content and Si doping have been investigated. From SPV spectra InGaN bandgap has been

extracted, ranging approximately from 2.6 to 2.9 eV depending on the In content within the layers; furthermore, the GaN peak always occurs at 3.4 eV. The InGaN band gap values result to be in agreement mostly with the theoretical results which consider the bowing parameter $b = 1$. Moreover, high Si doping corresponds to a higher interface recombination, that affects the SPV spectra. Good quality interfaces belong to samples with a combination of low In content and low Si doping. In addition, the increment of both elements' content promotes the formation of more disorder, leading to more pronounced Urbach tails.

Undoped $In_xGa_{1-x}N$/GaN samples grown with different In content have been investigated by SPV technique. As expected, the InGaN peak occurs at different energies depending on the In content within the layers, while the GaN peak occurs at 3.4 eV. Moreover, misfit dislocations generate a strong recombination at the InGaN/GaN interface. Another feature at around 2.3 eV can be related to the yellow band transition in GaN, which has been widely reported in literature [219].

SPV studies of $Al_xIn_yGa_{1-x-y}N$/GaN samples grown with different element contents and different thicknesses allowed us to clarify the role of the strain (compressive or tensile) with the material properties. The layers relax with the formation of pinholes, with increasing thickness.

In conclusion, the recombination processes at the III-Ns/GaN interface are affected by element composition, doping, and strain within the layers.

More details could be found in our planned paper with A. Minj, D. Cavalcoli et al.

Acknowledgements

I would like to thank my Italian supervisor, Prof. Daniela Cavalcoli, for her guidance, help and suggestions throughout both my Master thesis and Ph.D. years. I would like to thank my German supervisor, Prof. Giso Hahn, for his helpfulness both *in loco* and from distance even with short notice. I would like to thank Dr. Barbara Terheiden for her guidance during my stay in Konstanz and Jonathan Steffens for practical advices and help, both belonging to the Photovoltaics Division at University of Konstanz. A special thank goes to Dr. Albert Minj for his advices in lab and during the research. I want to thank also Dr. Martina Perani for her guidance during my first Ph.D. year and friendship. Thanks to Simon Philipp of Martino Poggio's group in Basel for deeply helping me with my German abstract.
I would like to thank all people who have deposited my samples: Dr. Martina Perani and Jonathan Steffens for the Si based samples at University of Konstanz; Dr. Thomas Fix's group for the inorganic perovskite samples at MaCEPV (Materials for electronic and photovoltaic devices) laboratory, iCube, CNRS at Université de Strasbourg; Dr. Albert Minj and people from AIXTRON laboratory at Herzogenrath for the ternary and quaternary nitride alloys.
A special thank goes to Dr. Filippo Giorgi for the kind and constant help, advices and company.
Thanks also to all my colleagues (and Tommaso) for both research advices and company, especially during lunch time.

First of all, I would like to thank my boyfriend Lorenzo, for his love, patience, advices, kindness, help, and guidance during this hard journey. Thank you; without you I would not be the person I am now.
Thanks to all my close family for the emotional and (also) financial support. Special thanks go to my father, my grandfather, my sister and brothers, my uncles, my cousins for always being there for me. Thank you, Vale, for being the best friend ever despite the distance.
I would like to thank all my friends here and there. In particular, Sara, and our long talks and wanderings in Bologna; Ilaria, for our chats and Spring parties; Maggie, for her wisdom, kindness and "goofiness"; Ornella, for our conversations and meals at home. Thanks to Cristiano, the best librarian and book-pusher in the world; time for happy hour has come! Thanks to

Underdogs and Braves American football teammates for the great trainings and company.

Last but not least, thanks Alexandra Elbakyan for giving life to Sci-Hub so that research papers are reachable everywhere.

Bibliography

[1] IPCC, Climate Change 2014: Synthesis Report. Contribution of Working Groups I, II and III to the Fifth Assessment Report of the Intergovernmental Panel on Climate Change, Genève, Switzerland, 2014. https://www.ipcc.ch/pdf/assessment-report/ar5/syr/SYR_AR5_FINAL_full.pdf.

[2] United Nations Climate Change, The Paris Agreement, (2018). https://unfccc.int/process/the-paris-agreement/what-is-the-paris-agreement.

[3] Q. Schiermeier, J. Tollefson, T. Scully, A. Witze, O. Morton, Energy alternatives: Electricity without carbon, Nature. 454 (2008) 816–823. doi:10.1038/454816a.

[4] A. Luque, S. Hegedus, Handbook of Photovoltaic Science and Engineering, John Wiley & Sons, Ltd, 2011.

[5] F.I. for E.S. (ISE) Solar, Photovoltaics Report, 2018. https://www.ise.fraunhofer.de/content/dam/ise/de/documents/publications/studies/Photovoltaics-Report.pdf.

[6] K. Yamamoto, D. Adachi, K. Yoshikawa, W. Yoshida, T. Irie, K. Konishi, T. Fujimoto, H. Kawasaki, M. Kanematsu, H. Ishibashi, T. Uto, Y. Takahashi, T. Terashita, G. Koizumi, N. Nakanishi, M. Yoshimi, Record-breaking efficiency back-contact heterojunction crystalline Si solar cell and module, in: 33rd Eur. Photovolt. Sol. Energy Conf. Exhib., 2017: pp. 201–204.

[7] G. Cantele, E. Degoli, E. Luppi, R. Magri, D. Ninno, G. Iadonisi, S. Ossicini, First-principles study of n- and p-doped silicon nanoclusters, Phys. Rev. B. 72 (2005) 113303. doi:10.1103/PhysRevB.72.113303.

[8] L.E. Ramos, E. Degoli, G. Cantele, S. Ossicini, D. Ninno, J. Furthmüller, F. Bechstedt, Structural features and electronic properties of group-III-, group-IV-, and group-V-doped Si nanocrystallites, J. Phys. Condens. Matter. 19 (2007) 466211. doi:10.1088/0953-8984/19/46/466211.

[9] M. Fujii, Y. Yamaguchi, Y. Takase, K. Ninomiya, S. Hayashi, Control of photoluminescence properties of Si nanocrystals by simultaneously doping n- and p-type impurities, Appl. Phys. Lett. 85 (2004) 1158–1160. doi:10.1063/1.1779955.

[10] D. Cavalcoli, F. Detto, M. Rossi, A. Tomasi, A. Cavallini, The electrical conductivity of hydrogenated nanocrystalline silicon investigated at the

nanoscale, Nanotechnology. 21 (2010) 045702. doi:10.1088/0957-4484/21/4/045702.

[11] National Geographic, What Is Global Warming?, (2018). https://www.nationalgeographic.com/environment/global-warming/global-warming-overview/.

[12] United Nations, Department of Economic and Social Affairs, Population Division (2015). World Population Prospects: The 2015 Revision, World Population 2015 Wallchart, 2015. https://esa.un.org/unpd/wpp/publications/files/key_findings_wpp_2015.pdf.

[13] O. Edenhofer, R.P. Madruga, Y. Sokona, et al., Renewable Energy Sources and Climate Change Mitigation: Special Report of the Intergovernmental Panel on Climate Change, Cambridge University Press, 2012.

[14] C. Battaglia, A. Cuevas, S. De Wolf, High-efficiency crystalline silicon solar cells: status and perspectives, Energy Environ. Sci. 9 (2016) 1552–1576. doi:10.1039/C5EE03380B.

[15] S. De Wolf, A. Descoeudres, Z.C. Holman, C. Ballif, High-efficiency Silicon Heterojunction Solar Cells: A Review, Green. 2 (2012) 7–24. doi:10.1515/green-2011-0018.

[16] Panasonic Corporation, Panasonic HIT® Solar Cell Achieves World's Highest Energy Conversion Efficiency of 25.6% at Research Level, (2014). https://news.panasonic.com/global/press/data/2014/04/en140410-4/en140410-4.html.

[17] K. Yoshikawa, H. Kawasaki, W. Yoshida, T. Irie, K. Konishi, K. Nakano, T. Uto, D. Adachi, M. Kanematsu, H. Uzu, K. Yamamoto, Silicon heterojunction solar cell with interdigitated back contacts for a photoconversion efficiency over 26%, Nat. Energy. 2 (2017) 17032. doi:10.1038/nenergy.2017.32.

[18] N. Brinkmann, D. Sommer, G. Micard, G. Hahn, B. Terheiden, Electrical, optical and structural investigation of plasma-enhanced chemical-vapor-deposited amorphous silicon oxynitride films for solar cell applications, Sol. Energy Mater. Sol. Cells. 108 (2013) 180–188. doi:10.1016/j.solmat.2012.09.025.

[19] M. Perani, N. Brinkmann, A. Hammud, D. Cavalcoli, B. Terheiden, Nanocrystal formation in silicon oxy-nitride films for photovoltaic applications: Optical and electrical properties, J. Phys. Chem. C. 119

(2015) 13907–13914. doi:10.1021/acs.jpcc.5b02286.

[20] S. De Wolf, G. Beaucarne, Surface passivation properties of boron-doped plasma-enhanced chemical vapor deposited hydrogenated amorphous silicon films on p-type crystalline Si substrates, Appl. Phys. Lett. 88 (2006) 022104. doi:10.1063/1.2164902.

[21] S. Dauwe, J. Schmidt, R. Hezel, Very low surface recombination velocities on p- and n-type silicon wafers passivated with hydrogenated amorphous silicon films, in: Conf. Rec. Twenty-Ninth IEEE Photovolt. Spec. Conf., IEEE, 2002: pp. 1246–1249. doi:10.1109/PVSC.2002.1190834.

[22] H. Yang, E. Wang, H. Wang, W. Guo, Industrial Technology of Passivated Emitter and Rear Cells with Silicon Oxynitride and Silicon Nitride as Rear Passivation for High Efficiency BIPV Modules, Energy Procedia. 88 (2016) 389–393. doi:10.1016/J.EGYPRO.2016.06.007.

[23] L. Serenelli, L. Martini, L. Imbimbo, R. Asquini, F. Menchini, M. Izzi, M. Tucci, Metastability of a-SiO_x:H thin films for c-Si surface passivation, Appl. Surf. Sci. 392 (2017) 430–440. doi:10.1016/j.apsusc.2016.09.026.

[24] S. Heo, J. Lee, S. Heon Kim, D.-J. Yun, J.-B. Park, K. Kim, N. Kim, Y. Kim, D. Lee, K.-S. Kim, H. Jae Kang, Device performance enhancement via a Si-rich silicon oxynitride buffer layer for the organic photodetecting device, Sci. Rep. 7 (2017) 1516. doi:10.1038/s41598-017-01653-z.

[25] D.M. Zhigunov, A. Sarikov, Y.M. Chesnokov, A.L. Vasiliev, N. Zakharov, P.K. Kashkarov, Thickness and temperature depending intermixing of SiO_x/SiO_2 and SiO_xN_y/SiO_2 superlattices: Experimental observation and thermodynamic modeling, Appl. Phys. Lett. 108 (2016) 223102. doi:10.1063/1.4953095.

[26] J. Valenta, M. Greben, S. Gutsch, D. Hiller, M. Zacharias, Photoluminescence performance limits of Si nanocrystals in silicon oxynitride matrices, J. Appl. Phys. 122 (2017) 144303. doi:10.1063/1.4999023.

[27] A.O. Zamchiy, E.A. Baranov, I.E. Merkulova, V.A. Volodin, M.R. Sharafutdinov, S.Y. Khmel, Effect of annealing in oxidizing atmosphere on optical and structural properties of silicon suboxide thin films obtained by gas-jet electron beam plasma chemical vapor deposition method, Vacuum. 152 (2018) 319–326. doi:10.1016/J.VACUUM.2018.03.055.

[28] I.B. Olenych, L.S. Monastyrskii, Y.V. Boyko, A.P. Luchechko, A.M. Kostruba, Photoluminescent properties of nc-Si/SiO_x nanosystems, Appl. Nanosci. (2018) 1–6. doi:10.1007/s13204-018-0701-4.

[29] S. Olibet, Properties of interfaces in amorphous/crystalline silicon heterojunctions, Institut de Microtechnique, Université de Neuchâtel, Ph.D. Thesis, 2009. https://doc.rero.ch/record/11674/files/Th_OlibetS.pdf.

[30] M. Perani, N. Brinkmann, M.A. Fazio, A. Hammud, B. Terheiden, D. Cavalcoli, Annealing effects on SiO_xN_y thin films: Optical and morphological properties, Thin Solid Films. 617 (2016) 133–137. doi:10.1016/j.tsf.2016.03.067.

[31] Perovskite-info, Perovskite introduction, (2018). https://www.perovskite-info.com/perovskite-introduction.

[32] Ossila, Perovskites and Perovskite Solar Cells: An Introduction, (2018). https://www.ossila.com/pages/perovskites-and-perovskite-solar-cells-an-introduction.

[33] M. Zhang, M.A. Farid, Y. Wang, J. Xie, J. Geng, H. Zhang, J. Sun, G. Li, F. Liao, J. Lin, Superconductivity in Perovskite $Ba_{1-x}Ln_x(Bi_{0.20}Pb_{0.08})O_{3-\delta}$ (Ln = La, Ce, Pr, Nd, Sm, Eu, Gd, Tb, Dy, Ho, Er, Tm, Yb, Lu), Inorg. Chem. 57 (2018) 1269–1276. doi:10.1021/acs.inorgchem.7b02693.

[34] K. Kaminaga, D. Oka, T. Hasegawa, T. Fukumura, Superconductivity of Rock-Salt Structure LaO Epitaxial Thin Film, J. Am. Chem. Soc. 140 (2018) 6754–6757. doi:10.1021/jacs.8b03009.

[35] D. Szczęśniak, A.Z. Kaczmarek, R. Szczęśniak, S. V. Turchuk, H. Zhao, E.A. Drzazga, Superconducting properties of under- and over-doped $Ba_xK_{1-x}BiO_3$ perovskite oxide, Mod. Phys. Lett. B. 32 (2018) 1850174. doi:10.1142/S0217984918501749.

[36] B. Raveau, A. Maignan, V. Caignaert, Spectacular Giant Magnetoresistance Effects in the Polycrystalline Perovskite $Pr_{0.7}Sr_{0.05}Ca_{0.25}MnO_{3-\delta}$, J. Solid State Chem. 117 (1995) 424–426. doi:10.1006/JSSC.1995.1297.

[37] Y. Moritomo, A. Asamitsu, H. Kuwahara, Y. Tokura, Giant magnetoresistance of manganese oxides with a layered perovskite structure, Nature. 380 (1996) 141–144. doi:10.1038/380141a0.

[38] A. Dhahri, E. Dhahri, E.K. Hlil, Giant magnetoresistance and correlation between critical behavior and electrical properties in a new compound $La_{0.6}Gd_{0.1}Sr_{0.3}Mn_{0.8}Si_{0.2}O_3$ manganite, J. Alloys Compd. 727

(2017) 449–459. doi:10.1016/J.JALLCOM.2017.08.086.

[39] N. Ahmed, S. Khan, A.A. Khan, A.G. Nabi, H. Ahmed, Z. ur Rehman, M.H. Nasim, Synthesis, Structural, Electronic, and Magnetic Properties of Cubic Perovskite $La_{1-x}Ba_xMnO_3$ ($0.125 \leq x \leq 0.875$) for Spintronic Devices, J. Supercond. Nov. Magn. (2018) 1–11. doi:10.1007/s10948-018-4691-y.

[40] J. Wang, X. Pan, C. Zhang, H. Guo, Z.V. Vardeny, Light-controlled spintronic device based on hybrid organic–inorganic perovskites, J. Photonics Energy. 8 (2018) 1. doi:10.1117/1.JPE.8.032207.

[41] R.J.H. Voorhoeve, J.P. Remeika, D.W. Johnson, P.K. Gallagher, Rare-Earth Manganites: Catalysts with Low Ammonia Yield in the Reduction of Nitrogen Oxides, Science. 180 (1973) 62–64. doi:10.1126/science.180.4081.62.

[42] L.S. Gangurde, G.S.J. Sturm, M.J. Valero-Romero, R. Mallada, J. Santamaria, A.I. Stankiewicz, G.D. Stefanidis, Synthesis, characterization, and application of ruthenium-doped $SrTiO_3$ perovskite catalysts for microwave-assisted methane dry reforming, Chem. Eng. Process. - Process Intensif. 127 (2018) 178–190. doi:10.1016/J.CEP.2018.03.024.

[43] A. Kojima, K. Teshima, Y. Shirai, T. Miyasaka, Organometal Halide Perovskites as Visible-Light Sensitizers for Photovoltaic Cells, J. Am. Chem. Soc. 131 (2009) 6050–6051. doi:10.1021/ja809598r.

[44] M.M. Lee, J. Teuscher, T. Miyasaka, T.N. Murakami, H.J. Snaith, Efficient hybrid solar cells based on meso-superstructured organometal halide perovskites, Science. (2012) 1228604. doi:10.1126/science.1228604.

[45] H.-S. Kim, C.-R. Lee, J.-H. Im, K.-B. Lee, T. Moehl, A. Marchioro, S.-J. Moon, R. Humphry-Baker, J.-H. Yum, J.E. Moser, M. Grätzel, N.-G. Park, Lead Iodide Perovskite Sensitized All-Solid-State Submicron Thin Film Mesoscopic Solar Cell with Efficiency Exceeding 9%, Sci. Rep. 2 (2012) 591. doi:10.1038/srep00591.

[46] W.S. Yang, B.-W. Park, E.H. Jung, N.J. Jeon, Y.C. Kim, D.U. Lee, S.S. Shin, J. Seo, E.K. Kim, J.H. Noh, S. Il Seok, Iodide management in formamidinium-lead-halide-based perovskite layers for efficient solar cells., Science. 356 (2017) 1376–1379. doi:10.1126/science.aan2301.

[47] K.T. Cho, S. Paek, G. Grancini, C. Roldán-Carmona, P. Gao, Y. Lee, M.K. Nazeeruddin, Highly efficient perovskite solar cells with a compositionally engineered perovskite/hole transporting material

interface, Energy Environ. Sci. 10 (2017) 621–627. doi:10.1039/C6EE03182J.

[48] D. Yang, R. Yang, K. Wang, C. Wu, X. Zhu, J. Feng, X. Ren, G. Fang, S. Priya, S. Liu, High efficiency planar-type perovskite solar cells with negligible hysteresis using EDTA-complexed SnO_2, Nat. Commun. 9 (2018) 3239. doi:10.1038/s41467-018-05760-x.

[49] M. Petrović, V. Chellappan, S. Ramakrishna, Perovskites: Solar cells & engineering applications – materials and device developments, Sol. Energy. 122 (2015) 678–699. doi:10.1016/J.SOLENER.2015.09.041.

[50] M. Jellite, J.-L. Rehspringer, M.A. Fazio, D. Muller, G. Schmerber, G. Ferblantier, S. Colis, A. Dinia, M. Sugiyama, A. Slaoui, D. Cavalcoli, T. Fix, Investigation of $LaVO_3$ based compounds as a photovoltaic absorber, Sol. Energy. 162 (2018) 1–7. doi:10.1016/J.SOLENER.2017.12.061.

[51] Y. Ievskaya, R.L.Z. Hoye, A. Sadhanala, K.P. Musselman, J.L. MacManus-Driscoll, Fabrication of ZnO/Cu_2O heterojunctions in atmospheric conditions: Improved interface quality and solar cell performance, Sol. Energy Mater. Sol. Cells. 135 (2015) 43–48. doi:10.1016/J.SOLMAT.2014.09.018.

[52] Y. Hotta, T. Susaki, H.Y. Hwang, Polar Discontinuity Doping of the $LaVO_3/SrTiO_3$ Interface, Phys. Rev. Lett. 99 (2007) 236805. doi:10.1103/PhysRevLett.99.236805.

[53] C. He, T.D. Sanders, M.T. Gray, F.J. Wong, V. V. Mehta, Y. Suzuki, Metal-insulator transitions in epitaxial $LaVO_3$ and $LaTiO_3$ films, Phys. Rev. B. 86 (2012) 081401. doi:10.1103/PhysRevB.86.081401.

[54] L. Wang, Y. Li, A. Bera, C. Ma, F. Jin, K. Yuan, W. Yin, A. David, W. Chen, W. Wu, W. Prellier, S. Wei, T. Wu, Device Performance of the Mott Insulator $LaVO_3$ as a Photovoltaic Material, Phys. Rev. Appl. 3 (2015) 064015. doi:10.1103/PhysRevApplied.3.064015.

[55] B. Luk, Dye-Sensitized Solar Cells, (2010). http://large.stanford.edu/courses/2010/ph240/luk2/.

[56] F.K. Yam, Z. Hassan, InGaN: An overview of the growth kinetics, physical properties and emission mechanisms, Superlattices Microstruct. 43 (2008) 1–23. doi:10.1016/J.SPMI.2007.05.001.

[57] J. Wu, When group-III nitrides go infrared: New properties and perspectives, J. Appl. Phys. 106 (2009) 011101. doi:10.1063/1.3155798.

[58] V.Y. Davydov, A.A. Klochikhin, R.P. Seisyan, V.V. Emtsev, S.V. Ivanov, F. Bechstedt, J. Furthmüller, H. Harima, A.V. Mudryi, J.

Aderhold, O. Semchinova, J. Graul, Absorption and Emission of Hexagonal InN. Evidence of Narrow Fundamental Band Gap, Phys. Status Solidi. 229 (2002) r1–r3. doi:10.1002/1521-3951(200202)229:3<R1::AID-PSSB99991>3.0.CO;2-O.

[59] H. Yamashita, K. Fukui, S. Misawa, S. Yoshida, Optical properties of AlN epitaxial thin films in the vacuum ultraviolet region, J. Appl. Phys. 50 (1979) 896–898. doi:10.1063/1.326007.

[60] H.P. Maruska, J.J. Tietjen, The preparation and properties of vapo-deposited single-crystalline GaN, Appl. Phys. Lett. 15 (1969) 327–329. doi:10.1063/1.1652845.

[61] M. Gonschorek, Physical Properties of $Al_{1-x}In_xN$/(AlN)/GaN ($0.07 \leq x \leq 0.21$) Heterostructures and their Application for High Power Electronics, École Polytechnique Fédérale de Lausanne, Ph.D. Thesis, 2011.

[62] L. Lugani, Leakage mechanisms and contact technologies in InAlN/GaN high electron mobility transistors, École Polytechnique Fédérale de Lausanne, Ph.D. Thesis, 2015.

[63] K. Lorenz, N. Franco, E. Alves, I.M. Watson, R.W. Martin, K.P. O'Donnell, Anomalous Ion Channeling in AlInN/GaN Bilayers: Determination of the Strain State, Phys. Rev. Lett. 97 (2006) 085501. doi:10.1103/PhysRevLett.97.085501.

[64] O. Ambacher, Growth and applications of Group III-nitrides, J. Phys. D. Appl. Phys. 31 (1998) 2653–2710. doi:10.1088/0022-3727/31/20/001.

[65] J. Wu, W. Walukiewicz, K.M. Yu, W. Shan, J.W. Ager, E.E. Haller, H. Lu, W.J. Schaff, W.K. Metzger, S. Kurtz, Superior radiation resistance of $In_{1-x}Ga_xN$ alloys: Full-solar-spectrum photovoltaic material system, J. Appl. Phys. 94 (2003) 6477–6482. doi:10.1063/1.1618353.

[66] L. Sang, M. Liao, Y. Koide, M. Sumiya, InGaN-based thin film solar cells: Epitaxy, structural design, and photovoltaic properties, J. Appl. Phys. 117 (2015) 105706. doi:10.1063/1.4914908.

[67] C.J. Neufeld, N.G. Toledo, S.C. Cruz, M. Iza, S.P. DenBaars, U.K. Mishra, High quantum efficiency InGaN/GaN solar cells with 2.95 eV band gap, Appl. Phys. Lett. 93 (2008) 143502. doi:10.1063/1.2988894.

[68] S.C. Jain, M. Willander, J. Narayan, R. Van Overstraeten, III–nitrides: Growth, characterization, and properties, J. Appl. Phys. 87 (2000) 965. doi:10.1063/1.371971.

[69] D. Holec, P.M.F.J. Costa, M.J. Kappers, C.J. Humphreys, Critical

thickness calculations for InGaN/GaN, J. Cryst. Growth. 303 (2007) 314–317. doi:10.1016/J.JCRYSGRO.2006.12.054.

[70] J. Li, K.B. Nam, K.H. Kim, J.Y. Lin, H.X. Jiang, Growth and optical properties of $In_xAl_yGa_{1-x-y}N$ quaternary alloys, Appl. Phys. Lett. 78 (2001) 61–63. doi:10.1063/1.1331087.

[71] M.A. Khan, J.W. Yang, G. Simin, R. Gaska, M.S. Shur, H.-C. zur Loye, G. Tamulaitis, A. Zukauskas, D.J. Smith, D. Chandrasekhar, R. Bicknell-Tassius, Lattice and energy band engineering in AlInGaN/GaN heterostructures, Appl. Phys. Lett. 76 (2000) 1161–1163. doi:10.1007/978-3-662-45603-3_23.

[72] R.T. Fonash, S. Ashok, S.J. Fonash, Solar cell, (2018). https://www.britannica.com/technology/solar-cell.

[73] C. Hu, R.M. White, Solar Cells: From Basic to Advanced Systems, McGraw-Hill College, University of California, Berkeley, 1983. https://nanohub.org/resources/14073/download/Solar_cells_by_Hu_and_White_1.pdf.

[74] J. Nelson, The physics of solar cells, Imperial College Press, London, 2009.

[75] PVEducation, Open-Circuit Voltage, (2018). https://www.pveducation.org/pvcdrom/open-circuit-voltage.

[76] R.H. Bube, Photovoltaic Materials, Imperial College Press, London, 1998.

[77] V.C. Pham, Functional graphene: synthesis, characterization and application in optoelectronics, Albert-Ludwigs-Universität Freiburg im Breisgau, Ph.D. Thesis, 2015.

[78] Physics of Solar Cells, (2018). http://depts.washington.edu/cmditr/modules/opv/physics_of_solar_cells.html.

[79] M. Perani, Nanocrystalline Silicon Based Films for Renewable Energy Applications, Università di Bologna, Ph.D. Thesis, 2014.

[80] H.B.T. Li, R.H. Franken, J.K. Rath, R.E.I. Schropp, Structural defects caused by a rough substrate and their influence on the performance of hydrogenated nano-crystalline silicon n–i–p solar cells, Sol. Energy Mater. Sol. Cells. 93 (2009) 338–349. doi:10.1016/J.SOLMAT.2008.11.013.

[81] P. Klapetek, D. Nečas, C. Anderson, Gwyddion user guide, (2018). http://gwyddion.net/documentation/user-guide-en/.

[82] D. Nečas, P. Klapetek, One-dimensional autocorrelation and power

spectrum density functions of irregular regions, Ultramicroscopy. 124 (2013) 13–19. doi:10.1016/J.ULTRAMIC.2012.08.002.

[83] M. Pelliccione, T.M. Lu, Evolution of thin lm morphology, Springer, New York, 2007.

[84] Y. Zhao, G.-C. Wang, T.-M. Lu, Characterization of Amorphous and Crystalline Rough Surface: Principles and Applications, Academic Press, San Diego, 2000.

[85] M. Perani, S. Carapezzi, G.R. Mutta, D. Cavalcoli, Nanostructured surfaces investigated by quantitative morphological studies, Nanotechnology. 27 (2016) 185703. doi:10.1088/0957-4484/27/18/185703.

[86] M.A. Fazio, Nano-scale morphological and electrical characterization of nc-SiO_xN_y thin layers for photovoltaic applications, Università di Bologna, Master Thesis, 2015.

[87] M. Pomaska, J. Mock, F. Köhler, U. Zastrow, M. Perani, O. Astakhov, D. Cavalcoli, R. Carius, F. Finger, K. Ding, Role of oxygen and nitrogen in n-type microcrystalline silicon carbide grown by hot wire chemical vapor deposition, J. Appl. Phys. 120 (2016) 225105. doi:10.1063/1.4971402.

[88] M. Sola, Optoelectronic properties of $LaVO_3$ perovskite for photovoltaic applications investigated by surface potential measurements, Università di Bologna, Master Thesis, 2016.

[89] ALtermatt Lecture, The air mass (AM), (2018). https://www2.pvlighthouse.com.au/resources/courses/altermatt/The Solar Spectrum/The air mass (AM).aspx.

[90] S. Pandey, D. Cavalcoli, A. Cavallini, Band bowing and Si donor levels in InGaN layers investigated by surface photo voltage spectroscopy, Appl. Phys. Lett. 102 (2013) 142101. doi:10.1063/1.4799658.

[91] Q.T. Li, A. Minj, M.P. Chauvat, J. Chen, P. Ruterana, Interface dislocations in $In_xGa_{1-x}N$/GaN heterostructures, Phys. Status Solidi. 214 (2017) 1600442. doi:10.1002/pssa.201600442.

[92] L. Dong, First Principles Study of Band Offsets and Band Bending of $In_xGa_{1-x}N$/GaN and $Zn_{1-x}Be_xO$/ZnO Heterostructures and Quantum Wells, University of Connecticut, Ph.D. Thesis, 2013. http://digitalcommons.uconn.edu/cgi/viewcontent.cgi?article=6311&context=dissertations.

[93] S.M. Ting, J.C. Ramer, D.I. Florescu, V.N. Merai, B.E. Albert, A. Parekh, D.S. Lee, D. Lu, D. V. Christini, L. Liu, E.A. Armour,

Morphological evolution of InGaN/GaN quantum-well heterostructures grown by metalorganic chemical vapor deposition, J. Appl. Phys. 94 (2003) 1461–1467. doi:10.1063/1.1586972.

[94] H. Ben Ammar, Analyse d'alliages ternaire AlInN et quaternaire AlGaInN pour application aux transistors à haute mobilité electronique par microscopie electronique en transmission, Université de Caen Normandie, Ph.D. Thesis, 2017.

[95] Bruker, SPM Microscopes - Intro to Scanning Probe Microscopy - Atomic Force Microscopy | AFM Microscope | Bruker, (2018). https://www.bruker.com/products/surface-and-dimensional-analysis/atomic-force-microscopes/campaigns/spm-microscopes-intro-to-scanning-probe-microscopy.html.

[96] G. Binning, H. Rohrer, Nobel Lecture: Scanning Tunneling Microscopy - From Birth to Adolescence, (1986) 21. https://www.nobelprize.org/prizes/physics/1986/binnig/lecture/.

[97] S. Sadewasser, T. Glatzel, Kelvin Probe Force Microscopy: From Single Charge Detection to Device Characterization, Springer, Berlin, Heidelberg, 2012.

[98] P. Russell, D. Batchelor, A.I. Facility, P.E. Russell, SEM and AFM : Complementary Techniques for Surface Investigations, Microsc. Anal. (2001) 9–12. doi:10.4103/0974-2077.63301.

[99] G. Binnig, C.F. Quate, C. Gerber, Atomic Force Microscope, Phys. Rev. Lett. 56 (1986) 930–933. doi:10.1103/PhysRevLett.56.930.

[100] V.L. Mironov, Fundamentals of scanning probe microscopy, The Russian Academy of Sciences, Moscow, 2004.

[101] F.J. Giessibl, Advances in atomic force microscopy, Rev. Mod. Phys. 75 (2003) 949–983. doi:10.1103/RevModPhys.75.949.

[102] NREL Materials Science, Conductive Atomic Force Microscopy, (2018). https://www.nrel.gov/materials-science/conductive-atomic.html.

[103] NT-MDT, Spreading resistance imaging, (2015). https://www.ntmdt-si.com/resources/spm-principles/atomic-force-microscopy/contact-afm/spreading-resistance-imaging.

[104] P. Eyben, M. Xu, N. Duhayon, T. Clarysse, S. Callewaert, W. Vandervorst, Scanning spreading resistance microscopy and spectroscopy for routine and quantitative two-dimensional carrier profiling, J. Vac. Sci. Technol. B Microelectron. Nanom. Struct. 20 (2002) 471. doi:10.1116/1.1424280.

[105] D. Cavalcoli, M. Rossi, A. Tomasi, A. Cavallini, Degeneracy and

instability of nanocontacts between conductive tips and hydrogenated nanocrystalline Si surfaces in conductive atomic force microscopy, Nanotechnology. 20 (2009) 045702. doi:10.1088/0957-4484/20/4/045702.

[106] Park Systems, Conductive AFM, (2018). https://www.parksystems.com/index.php/park-spm-modes/94-electrical-properties/233-conductive-afm.

[107] B. Zhang, P. Kutalek, P. Knotek, L. Hromadko, J.M. Macak, T. Wagner, Investigation of the resistive switching in Ag_xAsS_2 layer by conductive AFM, Appl. Surf. Sci. 382 (2016) 336–340. doi:10.1016/J.APSUSC.2016.04.152.

[108] Y. Heo, D. Kan, Y. Shimakawa, J. Seidel, Resistive switching properties of epitaxial $BaTiO_{3-\delta}$ thin films tuned by after-growth oxygen cooling pressure, Phys. Chem. Chem. Phys. 18 (2016) 197–204. doi:10.1039/C5CP05333A.

[109] P. Bousoulas, J. Giannopoulos, K. Giannakopoulos, P. Dimitrakis, D. Tsoukalas, Memory programming of TiO_{2-x} films by Conductive Atomic Force Microscopy evidencing filamentary resistive switching, Appl. Surf. Sci. 332 (2015) 55–61. doi:10.1016/J.APSUSC.2015.01.133.

[110] A. Ranjan, N. Raghavan, S.J. O'Shea, S. Mei, M. Bosman, K. Shubhakar, K.L. Pey, Conductive Atomic Force Microscope Study of Bipolar and Threshold Resistive Switching in 2D Hexagonal Boron Nitride Films, Sci. Rep. 8 (2018) 2854. doi:10.1038/s41598-018-21138-x.

[111] M. Kumar, B. Satpati, T. Som, Revealing multimode resistive switching in Cu-O nanostructures using conductive atomic force microscopy, Appl. Surf. Sci. 454 (2018) 82–86. doi:10.1016/J.APSUSC.2018.05.137.

[112] Y. Xia, C. Musumeci, J. Bergqvist, W. Ma, F. Gao, Z. Tang, S. Bai, Y. Jin, C. Zhu, R. Kroon, C. Wang, M.R. Andersson, L. Hou, O. Inganäs, E. Wang, Inverted all-polymer solar cells based on a quinoxaline–thiophene/naphthalene-diimide polymer blend improved by annealing, J. Mater. Chem. A. 4 (2016) 3835–3843. doi:10.1039/C6TA00531D.

[113] S.K. Swami, N. Chaturvedi, A. Kumar, R. Kapoor, V. Dutta, J. Frey, T. Moehl, M. Grätzel, S. Mathew, M.K. Nazeeruddin, Investigation of electrodeposited cobalt sulphide counter electrodes and their application in next-generation dye sensitized solar cells featuring organic dyes and cobalt-based redox electrolytes, J. Power Sources. 275 (2015) 80–89. doi:10.1016/J.JPOWSOUR.2014.11.003.

[114] T. Mates, P.C.P. Bronsveld, A. Fejfar, B. Rezek, J. Kočka, J.K. Rath,

R.E.I. Schropp, Detailed structural study of low temperature mixed-phase Si films by X-TEM and ambient conductive AFM, J. Non. Cryst. Solids. 352 (2006) 1011–1015. doi:10.1016/J.JNONCRYSOL.2005.10.058.

[115] I. Tanaka, I. Kamiya, H. Sakaki, N. Qureshi, S.J.A. Jr., P.M. Petroff, Imaging and probing electronic properties of self-assembled InAs quantum dots by atomic force microscopy with conductive tip, Appl. Phys. Lett. 74 (1999) 844. doi:10.1063/1.123402.

[116] T. Mueller, S. Schwertheim, W.R. Fahrner, Crystalline silicon surface passivation by high-frequency plasma-enhanced chemical-vapor-deposited nanocomposite silicon suboxides for solar cell applications, J. Appl. Phys. 107 (2010) 014504. doi:10.1063/1.3264626.

[117] C. Villeneuve-Faure, D. Le Borgne, E. Bedel-Pereira, K.I. Moineau Chane-Ching, D. Hernandez-Maldonado, I. Séguy, Cross Kelvin force microscopy and conductive atomic force microscopy studies of organic bulk heterojunction blends for local morphology and electrical behavior analysis, J. Appl. Phys. 117 (2015) 055501. doi:10.1063/1.4907213.

[118] T. Hamachi, S. Takeuchi, T. Tohei, M. Imanishi, M. Imade, Y. Mori, A. Sakai, Leakage current analysis for dislocations in Na-flux GaN bulk single crystals by conductive atomic force microscopy, J. Appl. Phys. 123 (2018) 161417. doi:10.1063/1.5011345.

[119] A. Fejfar, M. Hývl, A. Vetushka, P. Pikna, Z. Hájková, M. Ledinský, J. Kočka, P. Klapetek, A. Marek, A. Mašková, J. Vyskočil, J. Merkel, C. Becker, T. Itoh, S. Misra, M. Foldyna, L. Yu, P. Roca i Cabarrocas, Correlative microscopy of radial junction nanowire solar cells using nanoindent position markers, Sol. Energy Mater. Sol. Cells. 135 (2015) 106–112. doi:10.1016/J.SOLMAT.2014.10.027.

[120] M. Pea, L. Maiolo, E. Giovine, A. Rinaldi, R. Araneo, A. Notargiacomo, Electrical characterization of FIB processed metal layers for reliable conductive-AFM on ZnO microstructures, Appl. Surf. Sci. 371 (2016) 83–90. doi:10.1016/J.APSUSC.2016.02.112.

[121] D. Mikulik, M. Ricci, G. Tutuncuoglu, F. Matteini, J. Vukajlovic, N. Vulic, E. Alarcon-Llado, A. Fontcuberta i Morral, Conductive-probe atomic force microscopy as a characterization tool for nanowire-based solar cells, Nano Energy. 41 (2017) 566–572. doi:10.1016/J.NANOEN.2017.10.016.

[122] X.Y. Yan, J.F. Peng, S.A. Yan, X.J. Zheng, Electromechanical Characterization of Single GaN Nanobelt Probed with Conductive

Atomic Force Microscope, J. Electron. Mater. 47 (2018) 3869–3875. doi:10.1007/s11664-018-6261-2.

[123] Y. Zhang, Study of Schottky contact between Au and NiO nanowire by conductive atomic force microscopy (C-AFM): The case of surface states, Phys. E Low-Dimensional Syst. Nanostructures. 69 (2015) 109–114. doi:10.1016/J.PHYSE.2015.01.029.

[124] O. Pluchery, Y. Zhang, R. Benbalagh, L. Caillard, J.J. Gallet, F. Bournel, A.-F. Lamic-Humblot, M. Salmeron, Y.J. Chabal, F. Rochet, Static and dynamic electronic characterization of organic monolayers grafted on a silicon surface, Phys. Chem. Chem. Phys. 18 (2016) 3675–3684. doi:10.1039/C5CP05943G.

[125] S. Bakhti, N. Destouches, C. Hubert, S. Reynaud, F. Vocanson, T. Ondarçuhu, T. Epicier, Growth of single gold nanofilaments at the apex of conductive atomic force microscope tips, Nanoscale. 8 (2016) 7496–7500. doi:10.1039/C5NR08310A.

[126] C. Ríos, P. Hosseini, R.A. Taylor, H. Bhaskaran, Color Depth Modulation and Resolution in Phase-Change Material Nanodisplays, Adv. Mater. 28 (2016) 4720–4726. doi:10.1002/adma.201506238.

[127] R.A. Oliver, Advances in AFM for the electrical characterization of semiconductors, Reports Prog. Phys. 71 (2008) 076501. doi:10.1088/0034-4885/71/7/076501.

[128] Y. Martin, H.K. Wickramasinghe, Magnetic imaging by '"force microscopy"' with 1000 Å resolution, Appl. Phys. Lett. 50 (1987) 1455–1457. doi:10.1063/1.97800.

[129] B.D. Terris, J.E. Stern, D. Rugar, H.J. Mamin, Localized charge force microscopy, J. Vac. Sci. Technol. A Vacuum, Surfaces, Film. 8 (1990) 374–377. doi:10.1116/1.576399.

[130] Park Systems, Electrostatic Force Microscopy (EFM), (2018). https://www.parksystems.com/index.php/parl-spm-modes/dielectricpiezoelectric-properties/228-electric-force-microscopy-efm.

[131] W. Melitz, J. Shen, A.C. Kummel, S. Lee, Kelvin probe force microscopy and its application, Surf. Sci. Rep. 66 (2011) 1–27. doi:10.1016/J.SURFREP.2010.10.001.

[132] M. Nonnenmacher, M.P. O'Boyle, H.K. Wickramasinghe, Kelvin probe force microscopy, Appl. Phys. Lett. 58 (1991) 2921–2923. doi:10.1063/1.105227.

[133] J.M.R. Weaver, D.W. Abraham, High resolution atomic force

microscopy potentiometry, J. Vac. Sci. Technol. B Microelectron. Nanom. Struct. 9 (1991) 1559. doi:10.1116/1.585423.

[134] S. Kölsch, F. Fritz, M.A. Fenner, S. Kurch, N. Wöhrl, A.J. Mayne, G. Dujardin, C. Meyer, Kelvin probe force microscopy studies of the charge effects upon adsorption of carbon nanotubes and C_{60} fullerenes on hydrogen-terminated diamond, J. Appl. Phys. 123 (2018) 015103. doi:10.1063/1.5019486.

[135] K. Neuhaus, G. Gregori, J. Maier, Room Temperature Polarization Phenomena in Nanocrystalline and Epitaxial Thin Films of Gd-Doped Ceria Studied by Kelvin Probe Force Microscopy, ECS J. Solid State Sci. Technol. 7 (2018) P362–P368. doi:10.1149/2.0011808jss.

[136] M. Konečný, M. Bartošík, J. Mach, V. Švarc, D. Nezval, J. Piastek, P. Procházka, A. Cahlík, T. Šikola, Kelvin Probe Force Microscopy and Calculation of Charge Transport in a Graphene/Silicon Dioxide System at Different Relative Humidity, ACS Appl. Mater. Interfaces. 10 (2018) 11987–11994. doi:10.1021/acsami.7b18041.

[137] Y. Zhang, Y. Zhang, L. Song, Y. Su, Y. Guo, L. Wu, T. Zhang, Illustration of charge transfer in graphene-coated hexagonal ZnO photocatalysts using Kelvin probe force microscopy, RSC Adv. 8 (2018) 885–894. doi:10.1039/C7RA12037K.

[138] J. Yin, B. Vanderheyden, B. Nysten, Dynamic charge transfer between polyester and conductive fibres by Kelvin probe force microscopy, J. Electrostat. 96 (2018) 30–39. doi:10.1016/J.ELSTAT.2018.09.006.

[139] Y. Yamagishi, K. Kobayashi, T. Kimura, K. Noda, H. Yamada, Local carrier dynamics in organic thin film transistors investigated by time-resolved Kelvin probe force microscopy, Org. Electron. 57 (2018) 118–122. doi:10.1016/J.ORGEL.2018.02.041.

[140] H. Kim, S.J. Park, B. Kim, Y.J. Hwang, B.K. Min, Investigation of Surface Sulfurization in $CuIn_{1-x}Ga_xS_{2-y}Se_y$ Thin Films by Using Kelvin Probe Force Microscopy, ChemPhysChem. 19 (2018) 261–265. doi:10.1002/cphc.201701019.

[141] L.A. Renna, Y. Liu, T.P. Russell, M. Bag, D. Venkataraman, Evidence of tunable macroscopic polarization in perovskite films using photo-Kelvin Probe Force Microscopy, Mater. Lett. 217 (2018) 308–311. doi:10.1016/J.MATLET.2018.01.106.

[142] X. Niu, J. Chen, Z. Wang, X. Zhou, Z. Wang, L. Huang, L. Chi, Interface electronic property of organic/organic heterostructure visualized via kelvin probe force microscopy, Org. Electron. 61 (2018)

383–388. doi:10.1016/J.ORGEL.2018.06.018.

[143] A. Minj, H. Ben Ammar, A. Cros, N. Garro, P. Gamarra, S.L. Delage, P. Ruterana, Probing the Local Electrical Properties of Al(In,Ga)N by Kelvin Probe Force Microscopy, Phys. Status Solidi. 255 (2018) 1700427. doi:10.1002/pssb.201700427.

[144] J. Zhan, Z. Chen, Q. Jiao, Y. Feng, C. Li, Y. Chen, Y. Chen, F. Jiao, X. Kang, S. Li, Q. Wang, T. Yu, G. Zhang, B. Shen, Investigation on strain relaxation distribution in GaN-based μLEDs by Kelvin probe force microscopy and micro-photoluminescence, Opt. Express. 26 (2018) 5265. doi:10.1364/OE.26.005265.

[145] J. Gonzalez-Julian, K. Neuhaus, M. Bernemann, J. Pereira da Silva, A. Laptev, M. Bram, O. Guillon, Unveiling the mechanisms of cold sintering of ZnO at 250 °C by varying applied stress and characterizing grain boundaries by Kelvin Probe Force Microscopy, Acta Mater. 144 (2018) 116–128. doi:10.1016/J.ACTAMAT.2017.10.055.

[146] L. Kronik, Y. Shapira, Surface photovoltage phenomena: theory, experiment, and applications, Surf. Sci. Rep. 37 (1999) 1–206. doi:10.1016/S0167-5729(99)00002-3.

[147] W.H. Brattain, J. Bardeen, Surface Properties of Germanium, Bell Syst. Tech. J. 32 (1953) 1–41. doi:10.1002/j.1538-7305.1953.tb01420.x.

[148] H.C. Gatos, J. Lagowski, Surface Photovoltage Spectroscopy—A New Approach to the Study of High-Gap Semiconductor Surfaces, J. Vac. Sci. Technol. 10 (1973) 130–135. doi:10.1116/1.1317922.

[149] L.J. Brillson, The structure and properties of metal-semiconductor interfaces, Surf. Sci. Rep. 2 (1982) 123–326. doi:10.1016/0167-5729(82)90001-2.

[150] L. Kronik, Y. Shapira, Surface photovoltage spectroscopy of semiconductor structures: at the crossroads of physics, chemistry and electrical engineering, Surf. Interface Anal. 31 (2001) 954–965. doi:10.1002/sia.1132.

[151] Y. González, A. Abelenda, M. Sánchez, Surface photovoltage spectroscopy characterization of AlGaAs/GaAs laser structures, J. Phys. Conf. Ser. 792 (2017) 012021. doi:10.1088/1742-6596/792/1/012021.

[152] D. Cavalcoli, M.A. Fazio, Electronic transitions in low dimensional semiconductor structures measured by surface photovoltage spectroscopy, Mater. Sci. Semicond. Process. (2018). doi:10.1016/j.mssp.2018.05.027.

[153] D. Cavalcoli, B. Fraboni, A. Cavallini, Chapter Seven - Surface and Defect States in Semiconductors Investigated by Surface Photovoltage, Defects Semicond. Volume 91 (2015) 251–278. doi:http://dx.doi.org/10.1016/bs.semsem.2014.11.004.

[154] W. Mönch, Semiconductor Surfaces and Interfaces, Springer-Verlag, Berlin, 1993.

[155] D. Cavalcoli, A. Cavallini, Surface photovoltage spectroscopy - method and applications, Phys. Status Solidi. 7 (2010) 1293–1300. doi:10.1002/pssc.200983124.

[156] K. Shimakawa, J. Singh, S.K. O'Leary, Optical Properties of Disordered Condensed Matter. Optical Properties of Condensed Matter and Applications, J. Singh, John Wiley and Sons, 2006.

[157] M. Grundmann, The Physics of Semiconductors. An Introduction Including Nanophysics and Applications, 2nd Ed., Springer, 2010.

[158] D.K. Schroder, Surface voltage and surface photovoltage: history, theory and applications, Meas. Sci. Technol. 12 (2001) R16–R31. doi:10.1088/0957-0233/12/3/202.

[159] E. Muthuswamy, J. Zhao, K. Tabatabaei, M.M. Amador, M.A. Holmes, F.E. Osterloh, S.M. Kauzlarich, Thiol-Capped Germanium Nanocrystals: Preparation and Evidence for Quantum Size Effects, Chem. Mater. 26 (2014) 2138–2146. doi:10.1021/cm4042154.

[160] E. Kim, Y. Cho, A. Sohn, H. Hwang, Y.U. Lee, K. Kim, H.-H. Park, J. Kim, J.W. Wu, D.-W. Kim, Mie Resonance-Modulated Spatial Distributions of Photogenerated Carriers in Poly(3-hexylthiophene-2,5-diyl)/Silicon Nanopillars, Sci. Rep. 6 (2016) 29472. doi:10.1038/srep29472.

[161] T. Yao, R. Chen, J. Li, J. Han, W. Qin, H. Wang, J. Shi, F. Fan, C. Li, Manipulating the Interfacial Energetics of n-type Silicon Photoanode for Efficient Water Oxidation, J. Am. Chem. Soc. 138 (2016) 13664–13672. doi:10.1021/jacs.6b07188.

[162] D. Jana, T.K. Sharma, A correlation between the defect states and yellow luminescence in AlGaN/GaN heterostructures, J. Appl. Phys. 122 (2017) 035101. doi:10.1063/1.4993903.

[163] D. Cavalcoli, M. Rossi, A. Cavallini, Defect states in nc-Si:H films investigated by surface photovoltage spectroscopy, J. Appl. Phys. 109 (2011) 053719. doi:10.1063/1.3553583.

[164] H.P. Zhou, D.Y. Wei, S. Xu, S.Q. Xiao, L.X. Xu, S.Y. Huang, Y.N. Guo, S. Khan, M. Xu, Crystalline silicon surface passivation by intrinsic

silicon thin films deposited by low-frequency inductively coupled plasma, J. Appl. Phys. 112 (2012) 013708. doi:10.1063/1.4733701.

[165] G.B. Tong, Z. Aspanut, M.R. Muhamad, S. Abdul Rahman, Optical properties and crystallinity of hydrogenated nanocrystalline silicon (nc-Si:H) thin films deposited by rf-PECVD, Vacuum. 86 (2012) 1195–1202. doi:10.1016/J.VACUUM.2011.11.001.

[166] P. Dutta, S. Paul, D. Galipeau, V. Bommisetty, Effect of hydrogen plasma treatment on the surface morphology, microstructure and electronic transport properties of nc-Si:H, Thin Solid Films. 518 (2010) 6811–6817. doi:10.1016/J.TSF.2010.06.037.

[167] Y.-L. Hsieh, L.-H. Kau, H.-J. Huang, C.-C. Lee, Y.-K. Fuh, T. Li, In Situ Plasma Monitoring of PECVD nc-Si:H Films and the Influence of Dilution Ratio on Structural Evolution, Coatings. 8 (2018) 238. doi:10.3390/coatings8070238.

[168] Y. Wang, H. Liu, W. Shen, A Convenient and Effective Method to Deposit Low-Defect-Density nc-Si:H Thin Film by PECVD, Nanoscale Res. Lett. 13 (2018) 234. doi:10.1186/s11671-018-2641-z.

[169] L. Bagolini, A. Mattoni, L. Colombo, Electronic localization and optical absorption in embedded silicon nanograins, Appl. Phys. Lett. 94 (2009) 053115. doi:10.1063/1.3078281.

[170] Forter Tech, QTH Light Sources, (2018). http://www.forter.com.tw/products_detail.asp?seq=550.

[171] T.K. Sharma, S. Kumar, K.C. Rustagi, Frequency and intensity dependence of the sub-band-gap features observed in the surface photovoltage spectrum of semi-insulating GaAs, J. Appl. Phys. 92 (2002) 5959–5965. doi:10.1063/1.1513203.

[172] J.W. Orton, P. Blood, The electrical characterization of semiconductors: measurement of minority carrier properties, Academic Press, 1990.

[173] J.A. Woollam, Ellipsometry Tutorial, (2018). https://www.jawoollam.com/resources/ellipsometry-tutorial.

[174] Guide to using WVASE®, Spectroscopic Ellipsometry Data Acquisition and Analysis Software, J.A. Woollam Co., Inc. (2012). ftp://iristor.vub.ac.be/patio/SURF/pub/DATAtransit SURF-INTERNVUB/oscars/WVASE/WVASE_Manual.pdf.

[175] Thermo Nicolet Corporation, Introduction to Fourier Transform Infrared Spectrometry, (2001). https://www.researchgate.net/file.PostFileLoader.html?id=57ce879dd99e1e0364482dd&assetKey=AS%3A403246750420994%401473152925

890.

[176] K. Gerwert, C. Kötting, Fourier Transform Infrared (FTIR) Spectroscopy, in: Encycl. Life Sci., John Wiley & Sons, Ltd, Chichester, UK, 2010. doi:10.1002/9780470015902.a0003112.pub2.

[177] S. Rein, Lifetime Spectroscopy: A Method of Defect Characterization in Silicon for Photovoltaic Applications, Springer Berlin Heidelberg, 2005.

[178] T. Pisarkiewicz, Photodecay method in investigation of materials and photovoltaic structures, Opto-Electronics Rev. 12 (2004) 33–40.

[179] B. Dudda, Surface and interface states investigated in Si based thin films for photovoltaic applications, Università di Bologna, Master Thesis, 2017.

[180] Forter Tech, Quartz Tungsten Halogen Lamps, (2018). http://www.forter.com.tw/products_detail.asp?seq=2587.

[181] Photonics Media, A Guide to Selecting Lamps, (2018). https://www.photonics.com/Articles/A_Guide_to_Selecting_Lamps/a44487.

[182] P. Vecchi, Caratterizzazione elettrica e spettroscopia superfi ciale di film sottili a base di silicio, Università di Bologna, Bachelor Thesis, 2018.

[183] SPEX Industries Inc., M Series Spectrometers, (2018). http://www.horiba.com/fileadmin/uploads/Scientific/Documents/OSD/MSeries.pdf.

[184] HORIBA Scientific, Monochromators & Spectrographs, (2018). http://www.horiba.com/us/en/scientific/products/optics-tutorial/monochromators-spectrographs/.

[185] M. Cardona, Vibrational Spectra of Hydrogen in Silicon and Germanium, Phys. Status Solidi. 118 (1983) 463–481. doi:10.1002/pssb.2221180202.

[186] G. Lucovsky, J. Yang, S.S. Chao, J.E. Tyler, W. Czubatyj, Oxygen-bonding environments in glow-discharge-deposited amorphous silicon-hydrogen alloy films, Phys. Rev. B. 28 (1983) 3225–3233. doi:10.1103/PhysRevB.28.3225.

[187] E. Bustarret, M. Bensouda, M.C. Habrard, J.C. Bruyère, S. Poulin, S.C. Gujrathi, Configurational statistics in a-$Si_xN_yH_z$ alloys: A quantitative bonding analysis, Phys. Rev. B. 38 (1988) 8171–8184. doi:10.1103/PhysRevB.38.8171.

[188] R. Sčtoudek, J. Humlíček, Infrared spectroscopy of oxygen interstitials and precipitates in nitrogen-doped silicon, Phys. B Condens. Matter.

376–377 (2006) 150–153. doi:10.1016/j.physb.2005.12.040.

[189] H. Shanks, C.J. Fang, L. Ley, M. Cardona, F.J. Demond, S. Kalbitzer, Infrared-Spectrum and Structure of Hydrogenated Amorphous-Silicon, Phys. Status Solidi B-Basic Res. 100 (1980) 43–56. doi:10.1002/pssb.2221000103.

[190] J. Steffens, M.A. Fazio, D. Cavalcoli, B. Terheiden, Multi-characterization study of interface passivation quality of amorphous sub-stoichiometric silicon oxide and silicon oxynitride layers for photovoltaic applications, Sol. Energy Mater. Sol. Cells. 187 (2018) 104–112. doi:10.1016/J.SOLMAT.2018.07.024.

[191] P.G. Snyder, Y.-M. Xiong, J. Woollam, Graded refractive index silicon oxynitride thin film characterized by spectroscopic ellipsometry, Fac. Publ. from Dep. Electr. Comput. Eng. (1992). https://digitalcommons.unl.edu/electricalengineeringfacpub/69.

[192] A.L. Blum, J.S. Swirhun, R.A. Sinton, F. Yan, S. Herasimenka, T. Roth, K. Lauer, J. Haunschild, B. Lim, K. Bothe, Z. Hameiri, B. Seipel, R. Xiong, M. Dhamrin, J.D. Murphy, Interlaboratory study of eddy-current measurement of excess-carrier recombination lifetime, IEEE J. Photovoltaics. 4 (2014) 525–531.

[193] K.R. McIntosh, R.A. Sinton, Uncertainty in photoconductance lifetime measurements that use an inductive-coil detector, in: 23rd Eur. Photovolt. Sol. Energy Conf., Valencia, 2008: pp. 77–82.

[194] N. Brinkmann, Analyse der elektrischen, optischen und strukturellen Eigenschaften von Emitter und TCO Schichten für kristalline Silizium-Heterosolarzellen, Konstanz Universität, Ph.D. Thesis, 2014. http://kops.uni-konstanz.de/handle/123456789/28463.

[195] R.A. Street, Luminescence and recombination in hydrogenated amorphous silicon, Cambridge Solid State Science Series, New York, 1991.

[196] R. Rizzoli, C. Summonte, J. Plá, E. Centurioni, G. Ruani, A. Desalvo, F. Zignani, Ultrathin μc-Si films deposited by PECVD, Thin Solid Films. 383 (2001) 7–10. doi:10.1016/S0040-6090(00)01595-9.

[197] B. Rezek, J. Stuchlík, A. Fejfar, J. Kočka, Microcrystalline silicon thin films studied by atomic force microscopy with electrical current detection, J. Appl. Phys. 92 (2002) 587–593. doi:10.1063/1.1486032.

[198] A. Minj, D. Cavalcoli, A. Cavallini, Thermionic emission from the 2DEG assisted by image-charge-induced barrier lowering in AlInN/AlN/GaN heterostructures, Nanotechnology. 23 (2012) 115701.

doi:10.1088/0957-4484/23/11/115701.

[199] E.H. Rhoderick, R.H. Williams, Metal-semiconductor contacts, 2nd Ed., Oxford Science Publications, New York, 1978.

[200] M. Ahmetoglu (Afrailov), S.K. Akay, Determination of the parameters for the back-to-back switched Schottky barrier structures, Curr. Appl. Phys. 10 (2010) 652–654. doi:10.1016/J.CAP.2009.08.012.

[201] BYU Cleanroom, Metal-Semiconductor Ohmic and Schottky Contacts, (2018). http://cleanroom.byu.edu/ohmic-schottky.

[202] H.B. Michaelson, The work function of the elements and its periodicity, J. Appl. Phys. 48 (1977) 4729–4733. doi:10.1063/1.323539.

[203] R. Koole, E. Groeneveld, D. Vanmaekelbergh, A. Meijerink, C. de Mello Donegá, Size Effects on Semiconductor Nanoparticles, in: Nanoparticles, Springer Berlin Heidelberg, Berlin, Heidelberg, 2014: pp. 13–51. doi:10.1007/978-3-662-44823-6_2.

[204] I. Sychugov, F. Pevere, J.-W. Luo, A. Zunger, J. Linnros, Single-dot absorption spectroscopy and theory of silicon nanocrystals, Phys. Rev. B. 93 (2016) 161413. doi:10.1103/PhysRevB.93.161413.

[205] A.H.M. Smets, W.M.M. Kessels, M.C.M. Van de Sanden, Vacancies and voids in hydrogenated amorphous silicon, Appl. Phys. Lett. 82 (2003) 1547–1549. doi:10.1063/1.1559657.

[206] G. Lucovsky, R.J. Nemanich, J.C. Knights, Structural interpretation of the vibrational spectra of a-Si:H alloys, Phys. Rev. B. 19 (1979) 2064–2073. doi:10.1103/PhysRevB.19.2064.

[207] F. Wang, X. Zhang, L. Wang, Y. Jiang, C. Wei, S. Xu, Y. Zhao, Improved amorphous/crystalline silicon interface passivation for heterojunction solar cells by low-temperature chemical vapor deposition and post-annealing treatment, Phys. Chem. Chem. Phys. 16 (2014) 20202. doi:10.1039/C4CP02212B.

[208] W. Liu, L. Zhang, F. Meng, W. Guo, J. Bao, J. Liu, D. Wang, Z. Liu, Characterization of microvoids in thin hydrogenated amorphous silicon layers by spectroscopic ellipsometry and Fourier transform infrared spectroscopy, Scr. Mater. 107 (2015) 50–53. doi:10.1016/j.scriptamat.2015.05.018.

[209] T. Bååk, Silicon oxynitride; a material for GRIN optics, Appl. Opt. 21 (1982) 1069. doi:10.1364/AO.21.001069.

[210] W.R. Knolle, Correlation of refractive index and silicon content of silicon oxynitride films, Thin Solid Films. 168 (1989) 123–132. doi:10.1016/0040-6090(89)90695-0.

[211] W.C. Dash, R. Newman, Intrinsic optical absorption in single-crystal germanium and silicon at 77 K and 300 K, Phys. Rev. 99 (1955) 1151–1155. doi:10.1103/PhysRev.99.1151.

[212] R. Janssen, A. Janotta, D. Dimova-Malinovska, M. Stutzmann, Optical and electrical properties of doped amorphous silicon suboxides, Phys. Rev. B. 60 (1999) 13561–13572. doi:10.1103/PhysRevB.60.13561.

[213] Q.A. Shams, W.D. Brown, Physical and Electrical Properties of Memory Quality PECVD Silicon Oxynitride, J. Electrochem. Soc. 137 (1990) 1244. doi:10.1149/1.2086640.

[214] V.A. Gritsenko, Electronic structure of silicon nitride, Phys. - Uspekhi. 55 (2012) 498–507. doi:10.1080/01418639108224430.

[215] N. Honma, C. Munakata, H. Shimizu, Comparison of minority carrier lifetimes measured by photoconductive decay and ac photovoltaic method, Jpn. J. Appl. Phys. 27 (1988) L1498–L1503. doi:10.1143/JJAP.27.1498.

[216] S. Olibet, E. Vallat-Sauvain, C. Ballif, Model for a-Si:H/c-Si interface recombination based on the amphoteric nature of silicon dangling bonds, Phys. Rev. B. 76 (2007) 035326. doi:10.1103/PhysRevB.76.035326.

[217] H. Moormann, D. Kohl, G. Heiland, Work function and band bending on clean cleaved zinc oxide surfaces, Surf. Sci. 80 (1979) 261–264. doi:10.1016/0039-6028(79)90685-X.

[218] A. Minj, D. Cavalcoli, A. Cavallini, P. Gamarra, M.-A. di Forte Poisson, Strain distribution and defect analysis in III-nitrides by dynamical AFM analysis, Nanotechnology. 24 (2013) 145701. doi:10.1088/0957-4484/24/14/145701.

[219] M.A. Reshchikov, J.D. McNamara, H. Helava, A. Usikov, Y. Makarov, Two yellow luminescence bands in undoped GaN, Sci. Rep. 8 (2018) 8091. doi:10.1038/s41598-018-26354-z.

[220] M.A. Fazio, M. Perani, N. Brinkmann, B. Terheiden, D. Cavalcoli, Transport properties of Si based nanocrystalline films investigated by, J. Alloys Compd. 725 (2017) 163–170. doi:10.1016/j.jallcom.2017.07.151.

[221] The University of Sheffield, What is XRD?, (2018). https://www.sheffield.ac.uk/materials/centresandfacilities/x-ray-diffraction/whatxrd.

[222] Probion analysis, ECV Profiling, (2016). https://www.probion.fr/en/tutorials/ecvp/ecvprofiling.html.